Remote Control Electrodeposition:
Patterning on Substrates without Direct Electrical Connections

Trevor M. Braun

A dissertation

submitted in partial fulfillment of the

requirements for the degree of

Doctor of Philosophy

University of Washington

2016

Reading Committee:

Daniel T. Schwartz, Chair

Eric Stuve

Venkat Subramanian

Bo Zhang

Program Authorized to Offer Degree:

Chemical Engineering

University of Washington

Abstract

Remote Control Electrodeposition:
Patterning on Substrates without Direct Electrical Connections

Trevor M. Braun

Chair of the Supervisory Committee:
Professor Daniel T. Schwartz
Department of Chemical Engineering

Bipolar electrochemistry can overcome a key limitation in traditional electrochemistry, the need to electrically connect to the substrate. Wiring to a substrate is especially difficult for micro/nano-manufactured systems or complex three-dimensional geometries. Bipolar electrochemistry involves spatially segregated, equal and opposite reduction and oxidation on an electrically floating substrate. We show that spatial and temporal control of bipolar electrochemical couples enables patterned electrodeposition (or etching) by "remote control" without wiring to the substrate. The driving force for bipolar electrochemistry is the potential variation in solution when a current is passed; solution potential variation creates regions of differing electrochemical behavior (oxidation or reduction) on a single conducting substrate. Bipolar electrochemistry has intricate mating between the thermodynamics of the bipolar

electrochemical reactions, their charge transfer kinetics, and ionic migration through the electrochemical cell. We characterize local bipolar electrodeposition beneath the tip of a rastering microjet anode configuration we call a scanning bipolar cell (SBC). The fundamental interactions of thermodynamics, kinetics, and transport in the SBC are first explored using local cupric ion and nickel ion reduction to metal beneath the microjet, with concomitant oxidation of the copper substrate as the bipolar counter reaction. The bipolar current efficiency (BCE, the fraction of the applied current that flows through the unwired substrate) can be near unity under certain electrolyte and operating conditions. Advanced electrolyte design enables a wide variety of local electrodeposition chemistries (Ni, Cu, Au, and Ag) on an inert gold substrate; the bipolar counter reaction (ascorbic acid or ferrous ion oxidation) involves a far-field oxidation that leaves the gold substrate unchanged. Simple linearized scaling arguments capture the relationship between tool and electrolyte traits, enabling a 10X improvement in spatial resolution, down to the motion control limit of our device. But, scaling arguments over-predict the BCE compared to experimental values. Electroanalytical measurements of the bipolar electrolytes provide fundamental data that underpins more sophisticated simulations. Finite element method computations are used to explain where simple scaling relationships breakdown. The impact of local bipolar electrodeposition in printed circuit board repair, additive manufacturing, and electroanalytical research is discussed.

TABLE OF CONTENTS

LIST OF FIGURES

LIST OF TABLES

ACKNOWLEDGEMENTS

I would like to thank the following people for their contributions, both scientific and philosophic:

- Dan Schwartz for his guidance, mentorship, and instruction for which I'm forever grateful
- Jeff Nelson for teaching me about EcP and semiconductor testboard repair
- Funding provided by Boeing and the Department of Education
- Scott Braswell and Darick Baker for instruction and use of facilities in the MAF and WNF
- My advisory committee: Professors Venkat Subramanian, Eric Stuve, and Bo Zhang
- Matt Murbach for our many conversations on electrochemistry, impedance spectroscopy, and of course, enginearrings
- Current and former Schwartz Group members: Valerie Liu, Ikechukwu Nwaneshidu, Tyler House, Karl Oleson, and Yanbo Qi
- Mentorship from other UW ChemE faculty, particularly Jim Pfaendtner and Cole Deforest
- My family for their support and listening to me drone on about the good and bad of bipolar metal dots
- Finally, my Seattle family, for helping create an amazing experience in this beautiful city

DEDICATION

To: My parents and sister, for their unwavering support.

Chapter 1. THE PATHWAY TO REMOTE CONTROL ELECTRODEPOSITION

1.1 ELECTRODEPOSITION BACKGROUND

Electrodeposition (or electroplating) was discovered in the early 1800s by Luigi Brugnatelli, who grew a thin film of gold onto a silver substrate[1]. Over the next two centuries, electrodeposition has evolved into a precise science, providing a cost-effective, scalable process for industrial applications ranging from large-scale material coatings to nanoscale electronics fabrication. Electrodeposition requires an electrochemical cell consisting of (at a minimum) a current/voltage source electrically connected to two electrodes immersed in a conductive medium. Selection of the electrode materials and electrolyte composition depends on the desired electrochemical processes at each electrode surface. In electrodeposition, metal ions (M^{+z}) in solution are reduced at the cathode, reacting to form a metal layer ($M_{(s)}$) on the cathode surface:

$$M^{+z} + ze^{-} \rightarrow M_{(s)} \; . \tag{1.1}$$

For electrodeposition processes, the electrolyte and anode material are generally designed such that the oxidation reaction is unobtrusive to the reduction reaction occurring at the cathode. Essentially, oxidation at the anode (also called the counter electrode) is only necessary to provide electrons for electrodeposition at the cathode (considered the working electrode):

$$Oxidation\text{: } R \rightarrow O + ne^{-} \tag{1.2}$$

where *R* is a reducing agent that is oxidized to form products (*O*) and electrons. In many cases, the anode is an inert material (such as platinum) and the reaction chemistry is water oxidation for aqueous solutions. The geometric configuration of the electrochemical cell plays a significant role

in the extent of electrochemistry at the electrodes. For example, a Hull cell configuration sets a thin rectangular cathode at an angle to the anode. This produces an order of magnitude gradient of varying current densities along the cathode as a function of the distance from the anode [2]. This type of configuration is highly valuable for screening characteristics of electrodeposited materials over a wide range of current densities.

Another consistent aspect of most electrodeposition systems is forced convection to increase transport of reactants to the electrode interface[3]. Every electrochemical reaction becomes mass transfer limited after sufficient deviation from equilibrium, at which point, additional overpotential does not produce any additional current. This mass transfer limiting current is associated with the amount of reactant transport to the electrode by diffusion, migration, and convective processes. Forced convection can significantly increase reactant transport to the electrode and thus raise the mass-transfer limiting current. This enables higher reaction rates, meaning faster growth rates for electrodeposition applications. In most large scale electroplating applications forced convection is provided by mechanical stirring, air sparging with pumps, or use of eductors to generate turbulent flow[4]. The rotating disk electrode (RDE) was developed as a research tool for exploring the effect of mass transfer in electrochemical systems[5-7]. The angular rotation rate of the RDE is directly related to the mass transfer limiting current for an electrochemical reaction, making an RDE valuable for determining the diffusion coefficient of reactants and charge transfer kinetics. The RDE has been paramount in understanding electrochemical systems and is still heavily used in research over 70 years after its invention. Additional methods for increasing mass transport include use of microjet electrodes[8] and ultrasonic agitation[4,9].

1.2 USES IN INDUSTRY

Electroplating has been used in a wide variety of industrial applications over the past 200 years. One of the most significant electroplating applications is in material coatings for corrosion protection, expected to be a $26 billion market by 2019[13]. In the automobile industry, low cost materials such as steel or iron are electroplated with thin layers of sacrificial or passive metals to protect the substrate metal from corrosion. Pipelines for transporting petroleum and natural gas products are similarly electroplated to improve wear resistance against marine corrosion externally and against physical abrasion from particulates in the pipeline internally. In addition, decorative coatings, such as chrome, can provide both corrosion protection and aesthetic appeal. Decorative electroplated coatings of precious metals (such as gold or silver) are also commonly used in the consumer product and jewelry industries to create more desirable artifacts with less precious metal.

The highest value industry for electroplated metal is thin film deposition in semiconductor and microelectronics manufacturing. Thin film deposition includes physical and chemical vapor deposition as well as electrodeposition processes. One of the most commercially successful industries using thin film deposition technologies is integrated circuit (IC) manufacturing. IC devices have a complex three dimensional network of metallized features ranging from millimeters to 10s of nanometers. Electrodeposition is used across this entire lengthscale range, from deposition of interconnect pads used in device packaging several 100s of micrometers in size to damascene electrodeposition of copper circuitry 10s of nanometers in width[2,14]. In damascene electroplating, high aspect ratio cavities are filled through electrodeposition of copper in a bottom-up-fill manner. Polyethylene glycol (PEG) additives adsorb to the surface at the top of the cavity, suppressing copper deposition. The larger PEG molecules diffuse more slowly than copper ions, allowing copper deposition to begin at the bottom of the cavity creating bottom-up-fill of the high

aspect ratio features[15]. Additional studies demonstrate that copper deposition disrupts the neighboring adsorbed suppressor molecules, creating autocatalytic superconformal filling of the cavities[16]. Damascene electroplating enabled the use of copper instead of aluminum in IC devices, reducing bulk electrical resistivity and aiding in miniaturization of circuitry from a few microns to 10s of nanometers in width. While the damascene plating process is used on nanometer scale interconnects, through-mask plating methods are typically used in larger scale (micron to millimeter) electrodeposition of printed circuit boards (PCBs). Through-mask plating uses a photolithographic patterned mask, typically requiring several deposition and material removal steps to fully develop the pattern. One example of through-mask plating is in the manufacturing of gold-plated testboards used for testing integrated circuit devices before electronic packaging.

In the microelectronics industry, electrodeposition has been used in development of magnetic information storage systems, ranging from floppy disk to hard disk drives[2]. In a hard disk drive, the read/write heads are manufactured using photolithographic electrodeposition and etch techniques similar to through-mask plating for PCB boards. Consistency in head manufacturing is essential to allow operation at fly-heights less than 40 nm from the spinning disks. 3D Microelectromechanical systems (MEMS) consisting of components in the 1 to 100 micrometer range have also shown novel use of electrodeposition in their manufacturing. The most sophisticated and commercially successful of these is electrochemical fabrication (EFAB)[17,18]. EFAB is an additive manufacturing process that builds a three dimensional object layer by layer. Each layer involves three steps consisting of sacrificial material deposition, structural material deposition, and surface planarization. First, a sacrificial material is deposited using a pre-fabricated negative micromold. Then, the retained material is blanket deposited, filling in gaps left by the micromold and also depositing on top of the sacrificial material. Finally, both materials are

planarized to the desired layer thickness. After repeating until all of the layers of the build are completed, the sacrificial material is etched leaving only retained structural material with microfeature line rules down to 20 μm. Electrodeposition for semiconductor and microelectronics applications requires more complex electrochemical systems than large-scale electroplated coatings, but the value per gram of material deposited is significantly greater in these high-value, small length-scale markets.

1.3 LOCAL ELECTRODEPOSITION

In recent years, attempts have been made to transition from subtractive manufacturing to additive manufacturing methods. This revolution is being led by 3D-printing technologies that offer easy-to-use integrated software/hardware platforms for designing devices. Despite these advances, a similar shift to fully software reconfigurable electrodeposition-based prototyping has yet to emerge. The commercial electrodeposition fabrication techniques discussed above involve hardware masks or stamps to develop the pattern, placing limitations on their reconfigurability. Yet there have been several attempts to use localized electrochemistry for direct write electrodeposition and patterning. One of the first attempts at local electrodeposition was through the use of brush-plating. This technique uses an anode rod wrapped in a cloth material that absorbs electrolyte. Electrodeposition is confined to the area of contact between the rod/cloth wand and a cathodically polarized metal surface.

Another local electrodeposition method is the use of microelectrodes to confine current density locally on a conductive substrate, demonstrating growth rates on the order of micrometers per second[8]. Application of an electric field between a conductive substrate and a microelectrode in close proximity produces a highly localized current distribution at the substrate, with lateral

resolution dictated by the microelectrode dimensions. Highly developed scanning probe technologies such as scanning electrochemical microscopy (SECM) and scanning tunneling microscopy (STM) have demonstrated nanometer scale patterning for both electrodeposition and etching[19-21]. Microelectrode direct write electrodeposition addresses local control of current density and can easily achieve sub-micron resolution, but has diffusion limited mass transfer rates, which can limit material growth rates. Impinging jet electroplating systems address mass transfer limitations by providing controllable convective-diffusive mass transfer rates at the substrate. One of the first direct write jet-plating methods was developed by IBM in 1982 (laser-jet electroplating)[22-25]. This technology is able to achieve deposition rates of 50 $\mu m\ s^{-1}$ by combining jetted convection with a linearly-directed laser to further improve mass transfer and kinetic rates. Control of mass transfer and local current density enables a wide range of materials to be deposited, and can be software reconfigurable.

Our laboratory expanded on impinging jet electroplating systems by implementing full software control of all electrodeposition and mass transfer parameters with a tool called Electrochemical Printing (EcP), enabling flexible electrodeposition of metals and alloys in a raster or vector drawing mode[26-29]. EcP uses software images to define print locations and system operating conditions including applied current and charge, electrolyte flow rate, and microjet fly-height above the substrate. These parameters are loaded into a custom software program that controls the corresponding hardware components. The microjet nozzle diameter and fly-height are critical dimensions for deposit resolution. Full software control enables easily repeatable patterned deposition. EcP has been fully designed and optimized over the span of two previous PhD theses, and has successfully demonstrated electrodeposition of copper, nickel, platinum, gold, palladium, ruthenium, and copper-nickel alloys in previous work[26-32]. The EcP technology was also used in a

startup company, Micrametal, for repairing surface defects in gold-plated PCB testboards caused by repeated contact during IC device testing.

1.4 BIPOLAR ELECTROCHEMISTRY

One aspect of all the electrodeposition examples discussed above is that they require an electrical connection to the cathode. This requirement can be problematic when working with small, complexly patterned surfaces of both conductive and nonconductive materials that are difficult to electrically connect to. In recent years, a new area of scientific research has emerged using bipolar electrochemistry, enabling electrochemical reactions on a substrate without any direct electrical connections[33-47]. Bipolar electrochemistry is defined as spatially segregated, equal, and opposite reduction and oxidation reactions on an electronically conducting substrate without need for direct electrical connection. The driving force for bipolar electrochemistry is the ohmic potential variation in solution that forms during the passage of current in an electrochemical cell. When there is an appreciable ohmic potential drop through solution, and a conductor is in that potential gradient, current will have two alternative paths. Current can pass as ionic current entirely through the electrolyte or undergo charge transfer on one side of the electronic conductor, propagate as an electronic current, and then undergo a second (equal and opposite) charge transfer process on the other side of the conductor. When the path of least resistance is through the electronic conductor, bipolar electrochemistry results.

While bipolar electrochemistry is being reinvigorated for new electroanalytical and materials applications it is by no means a new phenomenon. Corrosion, one of the most intensely studied electrochemical phenomenon, is a form of bipolar electrochemistry. In aqueous environments, reduction of dissolved gaseous oxygen (ORR) on metals such as iron or copper can

induce electrochemical oxidation of that metal, forming metal ions or metal oxides. One driving force for corrosion is the energetically favorable thermodynamic difference between the equilibrium potentials of the reduction reaction and oxidation of the corroding metal. The extent of corrosion (oxidation) is equal and opposite to the ORR (reduction) and spatially separated on the metal substrate. Bipolar electrochemistry is also used in the design of redox flow batteries. Bipolar plates separate the cells in flow batteries, keeping anolyte and catholyte reactants separate while permitting electronic current flow between cells in the stack[48]. The plates are bipolar in that they contact the surface of a cathode (reduction) in one cell and an anode (oxidation) in another cell. Significant research has been devoted to optimizing these bipolar plates to reduce shunt currents (ionic current passage between cells) and maximize power and performance[49].

In recent years, bipolar electrochemical systems have been used for new types of electrochemical applications, particularly for surface modification and electroanalytics. For example, bipolar electrochemistry induced by the solution potential gradient across a conductive substrate can generate a compositionally graded material along that surface[50]. Electroanalytical chemistry applications are now using the power of bipolar electrochemistry to multiplex high throughput screening of electrocatalysts, and in this case, the equal but opposite nature of the system means that optical indicators can be used to quantify the reaction rates of the hard-to-detect chemistries of interest[35-37]. One can also use bipolar electrochemistry to generate a redox state gradient in solution or through a conducting polymer[40,42]. Bipolar electrochemistry has also been used to micropattern conductive polymers immersed in a static conductive electrolytic solution, eliminating the need for a template[51].

Bipolar electrochemistry is also useful for applications involving electrodeposition and patterning of electrically isolated substrates. For example, copper interconnects can be grown

between two electrically isolated copper posts without any direct electrical contact by placing them in a solution with high ohmic resistance[33,34]. This generates a large electric field that creates sufficient voltage across each post to drive copper reduction and the growth of material between them (since it is bipolar, there is an equal but opposite oxidation also occurring). Similarly, one can also use the equal and opposite nature of bipolar electrochemistry to make Janus type conducting particles that are differentially decorated based on the induced bias across the dimensions of the particle[52]. Bipolar electrochemistry that employs a reversible electrodeposition/etching chemistry can cause a free floating conductor of the active material to etch on one side and deposit an equal amount on the other side, resulting in a propagating chemical wave that moves in the direction of the solution potential gradient[53]. Single layer graphene sheets selectively modified with copper nanoparticles through bipolar electrodeposition provide edge functionalization to the monolayer sheets[54]. Closed bipolar electrochemistry, a system where the only current pathway is through the conductive substrate, has been used to control the growth of single gold nanowires by electrodeposition[46].

The intricate coupling between thermodynamics, kinetics, and ohmic potential drop in an electrolyte controls the behavior of bipolar electrochemical systems. Among the most impactful and intensely studied of these systems is pitting corrosion, where several different mechanisms can produce localized oxidation (in the corroding pit) that is balanced by an equal and opposite reduction in the far-field[55-68]. Pitting corrosion is a naturally occurring phenomenon that can teach us how to do desirable localized electrochemistry by remote control, with no electrical contact to the substrate. The pitting corrosion “IR mechanism”, in particular, can be adapted to an engineered system. In the “IR mechanism”, ohmic potential drop through the electrolyte solution in the pit is responsible for dictating where the surface actively corrodes (pit tip), is passive (pit walls), and

where delocalized dioxygen reduction happens (far-field outside the pit)[69-74]. There are two key ideas embedded in the "IR mechanism" that must be reversed to achieve localized electrodeposition and patterning. First, an electron donating species must be introduced into the system that has thermodynamics and kinetics well-mated to the desired reduction chemistry; this is in contrast to the electron acceptor found in corrosion (normally dioxygen). Second, we need to engineer a potential contour through solution that results in localized reduction with equal and opposite far-field oxidation of the electron donor.

Recent bipolar electrochemical applications require resistive electrolyte solutions and macroscopic electrochemical cells to produce the electrolyte potential gradients needed to drive bipolar reactions on small conductors. In the work presented in this thesis, we flip the structure of a traditional bipolar electrochemical cell, and use a microscopic electrochemical cell configuration (termed the scanning bipolar cell) that generates potential gradients locally over a macroscopic conductive surface. Adapting the EcP system for electrodeposition in a bipolar manner required only the addition of a far-field feeder cathode while leaving the substrate electrically isolated. In this configuration, current can pass between the two feeder electrodes either entirely through the electrolyte solution, or, it can undergo charge transfer at the floating substrate in the form of equal and opposite, spatially segregated oxidation and reduction reactions. While adaptation of the EcP equipment for bipolar electrochemistry was trivial, implementation of the SBC for practical and valuable bipolar electrodeposition requires complete understanding of the relationships between the ohmic distribution in solution, charge transfer reaction kinetics of the two bipolar redox reactions, and their thermodynamic relationship. Thus, the work herein focuses on understanding and describing the coupling of transport, kinetic, and thermodynamic processes necessary for designing bipolar electrochemistry with the scanning bipolar cell.

Bipolar electrodeposition with the SBC is focused on three types of systems: bipolar electrochemical sculpting, bipolar electrochemical displacement, and remote control electrochemistry. In Chapter 2, we explore bipolar electrochemical sculpting through the reduction of cupric ion (to copper) beneath the microjet on a copper substrate that oxidizes in the far-field. The result for the cupric/copper system is a "sculpting" of the originally planar substrate. Reduction of other metal cation-containing electrolytes beneath the microjet, while continuing to use far-field copper oxidation, results in "bipolar electrochemical displacement" (BED). BED is equivalent in many ways to galvanic displacement of one metal by another, but the thermodynamics can be "uphill". In Chapter 3, BED is explored using local deposition of nickel (the less noble metal) to displace an equal and opposite amount of far-field copper (the more noble metal) that etches across the entire wetted substrate. Generalizing bipolar electrodeposition in the SBC needs an alternative bipolar counter reaction to metal etching so that the workpiece remains unchanged while undergoing bipolar reactions. In Chapter 4, we address the full design of bipolar electrolytes for the SBC, where both the reduction and oxidation chemistries are optimized based on the thermodynamics of the system and the desire to leave the far-field of the substrate unaltered. We call this "remote control" electrochemistry because local modification of a substrate occurs without altering the far-field region of the substrate and with no need for an electrical connection. Chapter 5 explores electroanalytics of bipolar electrolytes to fully understand kinetics, thermodynamics, and effects of secondary reactions for nickel and copper systems. In Chapter 6, scaling relationships for the SBC are developed to relate the intricate coupling of ohmic drop, charge transfer kinetics, and thermodynamics to tool operation. Finally, Chapter 7 explores the impact of local bipolar electrodeposition and patterning in specific industries as well as in future research applications.

Chapter 2. BIPOLAR ELECTROCHEMICAL SCULPTING

2.1 SUMMARY

Microscopic, spatially controlled, and highly efficient bipolar electrochemistry can be performed on an electrically-floating macroscopic conductive substrate using a tool we call the Scanning Bipolar Cell (SBC). The operating principle for the SBC is that current follows the path of least resistance. A high ohmic potential drop can be generated in the electrolyte adjacent to the conductive substrate by using a moderate conductivity electrolyte with a microjet cell geometry, inducing localized charge transfer on the substrate beneath the microjet. The equal and opposite redox chemistry necessary for sustained bipolar electrochemistry is spread over the macroscopic far-field of the floating conductive substrate. We combine experiments and finite element simulations to demonstrate this system using reversible copper redox chemistry. Bipolar electrochemical coupling to the surface can be highly efficient in the SBC and is governed by the balance of interfacial charge transfer and solution ohmic resistances, as characterized by the Wagner number of the system

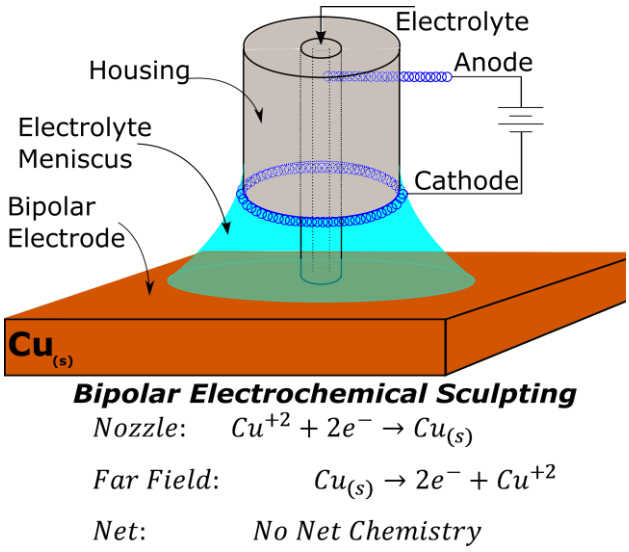

Figure 2.1. Bipolar electrochemical sculpting

2.2 INTRODUCTION

The normal design paradigm for electrochemical applications is to create electrolytes and electrochemical cell configurations that reduce ohmic drop through solution, making most conventional electrolytes and cells ill-suited to bipolar electrochemistry. There are some exceptions to this normal design paradigm. We have developed an electrodeposition method called "Electrochemical Printing" (EcP) where the electrolytes and microjet cell configuration are engineered to have a high, localized, and easily controllable ohmic drop in solution[26,28-30]. The EcP configuration produces localized electrodeposition when ohmic potential drop is large compared to charge transfer overpotential, i.e. when there is a small Wagner number[32]. The ohmic drop in EcP is spatially localized over a conducting substrate, creating an ideal platform for bipolar electrochemical experiments. Here we explore the opportunity for using our existing EcP tool as a scanning bipolar cell (SBC) able to perform localized and controllable electrochemistry by remote control, without direct electrical contact to a substrate where the deposition occurs.

2.3 EXPERIMENTAL AND SIMULATION METHODS

2.3.1 *Bipolar Plating Electrolyte*

Here we demonstrate bipolar electrochemistry in the scanning bipolar cell using the highly reversible copper chemistry. The bipolar electrodeposition bath is unmodified from the copper EcP bath we have used previously: 0.1 M $CuSO_4$ and 0.001 M H_2SO_4 (pH 2.8)[27,28]. EcP baths are a good starting point for bipolar electrodeposition (reduction), as they are designed for use in a high ohmic resistance system. To complete the room temperature bipolar redox couple (i.e., oxidation), we use a copper substrate. Thus, the bipolar electrochemical system is:

$$Reduction: Cu^{+2} + 2e^{-} \rightarrow Cu_{(s)} \quad (2.1)$$

$$Oxidation: Cu_{(s)} \rightarrow Cu^{+2} + 2e^{-} \quad (2.2)$$

The high current efficiency for both the forward and backward reactions means that copper will (effectively) be redistributed across the substrate based on the spatial nature of the solution ohmic potential variations; the solution potential variation is governed by details of the electrochemical cell that is used.

2.3.2 *Scanning Bipolar Cell (SBC)*

Figure 2.2a shows a perspective view schematic of key features in the SBC system. Electrolyte is pumped through an electrically insulating microjet nozzle where it passes a platinum feeder anode inserted into the stream. The electrolyte flows out of the microjet nozzle and pools on the bipolar electrode surface (an electrically floating copper substrate). The electrolyte forms a meniscus that then contacts the platinum feeder cathode which is fixed to the acrylic nozzle housing. Figure 2.2b further depicts a cross-section of the axisymmetric system geometry. The key geometric features of the nozzle that dictate the electrochemical behavior of the SBC are the inner (r_i) and outer (r_o) radii of the nozzle, as well as the fly-height (H) of the nozzle above the bipolar electrode substrate. For our experimental system we use a microjet nozzle with an inner radius of 100 μm and an outer radius of 335 μm. Flow rates in the microjet were held constant at 400 μL min^{-1} in all experiments.

2.3.3 *Bipolar Electrode Substrate Preparation*

To carry out the bipolar chemistry denoted in Eqs. 2.1-2.2, a copper substrate was required as the bipolar electrode. High planarity electrodeposited copper substrates were used in all experiments reported here. Silicon wafers with 50 nm gold on a 5 nm titanium adhesion layer were

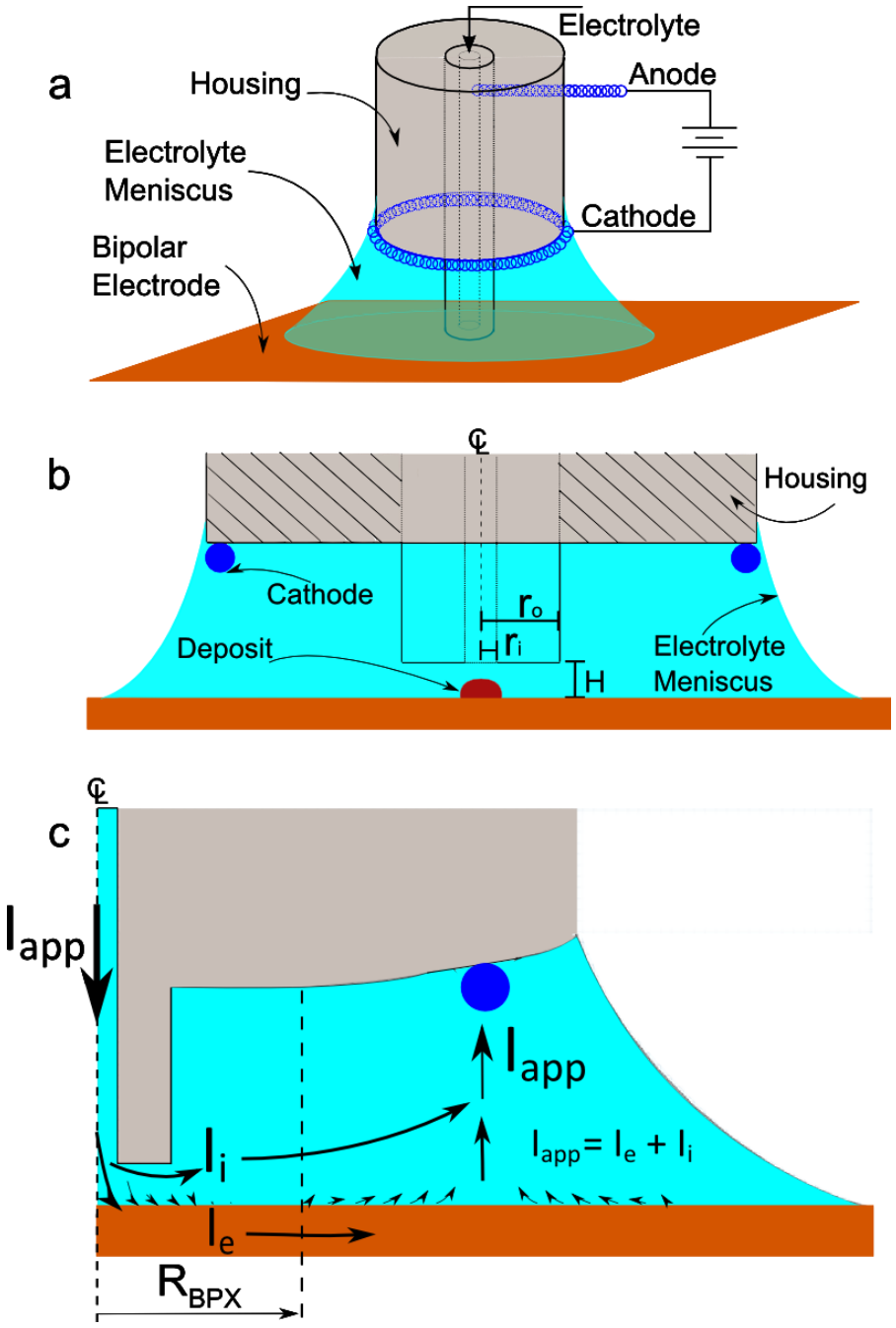

Figure 2.2. Schematics of the scanning bipolar cell

a. Perspective view schematic of the scanning bipolar cell (SBC) and its important components. **b**. Illustrates geometric features of the nozzle. **c**. Shows the to-scale axisymmetric geometry used in COMSOL simulations for the case when H = $2r_i$. The total applied current I_{app} is the sum of the ionic current (I_i) and the electronic current (I_e).

prepared using an E-beam evaporator at the University of Washington Nanofabrication Facility (WNF). Prior to copper electrodeposition, the gold substrates were cleaned via 20 cyclic voltammetry sweeps at 100 mV s^{-1} from -400 to 1700 mV vs SCE in a 1 M H_2SO_4 solution with a Pine Model AFRDE5 Bi-potentiostat. Gold substrates were then rinsed with DI water and dried with N_2 gas. Electrodeposition of bright copper on the clean gold substrates was carried out in a 0.24 M $CuSO_4$, 0.4 M H_2SO_4, and 1.4 mM HCl electrolyte using the same bi-potentiostat. The substrate electrodeposition step was carried out galvanostatically at 25 mA cm^{-2} for a total of 10-20 seconds in a well-mixed beaker with a Pt counter electrode. Plated copper substrates were immediately removed from the electrolyte solution to avoid corrosion and were rinsed with DI water and dried with N_2 gas. All electrodeposition steps were carried out at room temperature.

2.3.4 *Characterization Tools*

An Olympus BX51 optical microscope with an Olympus QColor3 digital camera and 5.0X objective was used to take optical micrographs of each sample. An Oakton model no. 510 pH/conductivity meter was used to measure pH. Electrolyte conductivities were measured with a Mettler Toledo S230 conductivity meter with an InLab 738 ISM probe. Electrodeposited profiles were measured with an Alpha-Step 500 profilometer.

2.3.5 *Simulation Methods*

Secondary current distribution computations were performed in the axisymmetric 2D computational domain shown in Figure 2.2c. These computations were used to determine the relevant current flow pathways through the electrolyte (denoted I_i, for ionic current, in Figure 2.2c) and extent of bipolar electrochemistry through the substrate (denoted I_e, for electronic current, in Figure 2.2c).

A secondary current distribution is appropriate here because the concentration is substantially uniform (limiting current densities can exceed 10 A cm^{-2}, so it is reasonable to neglect concentration gradients for all of our experiments)[27]. For this secondary current distribution problem, Laplace's equation governs the potential distribution (φ) in the electrolyte domain

$$\nabla^2 \varphi = 0 \ . \tag{2.3}$$

The nozzle, housing walls, and electrolyte meniscus are treated as insulating boundary conditions,

$$n \cdot \nabla \varphi = 0 \ . \tag{2.4}$$

The boundary condition for the feeder anode at the microjet inlet is given as

$$-\kappa n \cdot \nabla \varphi = \frac{I_{app}}{A_{nozzle}} \ , \tag{2.5}$$

and the feeder cathode boundary condition is

$$-\kappa n \cdot \nabla \varphi = \frac{-I_{app}}{A_{cathode}} \ , \tag{2.6}$$

where κ is the electrolyte conductivity, A_{nozzle} is the area of the nozzle where the current is applied, and $A_{cathode}$ is the area of the outer ring cathode. The reversible copper bipolar electrochemistry occurring on the conducting substrate is given by the Butler-Volmer equation

$$i = i_o \left[e^{\frac{\alpha n F}{RT} \eta_s(r)} - e^{\frac{-(1-\alpha) n F}{RT} \eta_s(r)} \right] \tag{2.7}$$

where the room temperature parameters for copper are assumed to be i_o = 3.35 mA cm^{-2} , α = 0.73, and n = 2 [75]. The surface overpotential shown in Eq. 2.7 is[76]

$$\eta_s = V_s - \varphi(r) - E_{eq} \ , \tag{2.8}$$

where the potential φ at the surface is shown explicitly as a function of radial position, while the potential of the conductive substrate V_s and the equilibrium potential E_{eq} are constants. For these simulations, we assume there is a single reversible copper chemistry on the conductive substrate

measured with a reference electrode of the same kind (i.e., reversible copper reference), resulting in $E_{eq} = 0$, $V_s = 0$, and $\eta_s = -\varphi(r)$.

The bipolar electrode must have equal and opposite oxidation and reduction reactions to remain charge neutral, which can be expressed by the integral constraint over the area of the electrode

$$I_{e,net} = 2\pi \int_0^R i_o \left[e^{\frac{\alpha_a nF}{RT}\eta_s(r)} - e^{\frac{-(1-\alpha_a)nF}{RT}\eta_s(r)} \right] r dr = 0. \quad (2.9)$$

Here, $I_{e,net}$ is the net electronic current passing through the bipolar substrate, which must be zero when integrated over the whole electrode.

Mesh refinement in the regions of high gradients was used so that the overall charge balance in the system and the substrate integral on the bipolar electrode, Eq. 2.9, both converged to less than 0.01% error. Grid refinement to achieve this level of charge balance resulted in about 300,000 mesh elements and a computational time of approximately 1-3 minutes for a typical converged solution. All simulations converged for realistic geometric conditions, however, as fly-height was reduced, system gradients beneath the nozzle increased and mesh refinement became more substantial in the annular gap region in order to meet charge balance constraints. All computations were performed on a Lenovo ThinkCenter model M7052-C9U with an Intel® Core™ i7-2600 CPU @ 3.40 GHz and 8GB RAM using a Windows 7 Professional 64-bit operating system. Finite element method (FEM) simulations were performed using COMSOL version 4.4 software with the heat transfer in fluids module.

2.4 Results and Discussion

Equations 2.8 and 2.9 show that the radial dependence of surface overpotential is the driving force for the bipolar electrochemistry on the conductive substrate. Our assumption that V_s

= constant is effectively a statement that the substrate has infinite conductivity (relative to the solution), so there are negligible potential gradients in the conductor needed to carry electronic current through the substrate. We can understand the system qualitatively from Figure 2.2c. When an applied current is sourced from the anode at the microjet inlet to the cathode located distant from the substrate (at the electrolyte meniscus), the applied current (I_{app}) is carried through the microjet as an ionic current toward the nozzle exit. At this point, current can continue to be transported as an ionic current (denoted I_i) through the annular gap between the microjet and the conductive bipolar electrode and out to the cathode. However, the geometry of the SBC and the low conductivity of the electrolyte (compared to the substrate) means current flow as electrons through the substrate (denoted I_e) may be a lower resistance alternative to ionic current flow through the annular gap. Electronic current flow through the substrate requires charge transfer, with localized reduction occurring beneath the nozzle and an equal and opposite oxidation reaction outside the annular gap. The sum of pathways I_i and I_e are equal to the total applied current (I_{app}). Ideally, we configure the SBC so that the path of least resistance for current flow is via the bipolar electrochemistry route, resulting in high current efficiency for the bipolar electrochemistry.

Figure 2.3 shows that the qualitative effects described above happen in practice, and the SBC indeed induces localized electrodeposition beneath the nozzle and an equal but opposite oxidation current spread over the much larger region outside the nozzle. The optical micrograph shows the systematic effect of applied current and fly-height on bipolar electrochemistry with the SBC. An array of copper deposits was electrodeposited on a copper substrate over the range of conditions shown. In this experiment, the applied current was varied along the horizontal axis from 60 μA to 160 μA in 20 μA increments and H was varied along the vertical axis from 25 μm to 50 μm in 5 μm increments. The deposition time was held constant at 5 seconds for each bipolar

condition, resulting in the total charge deposited per dot varying proportionally with applied current. The deposits are spaced 400 μm center to center. The array demonstrates how different electrochemical and geometrical operating conditions can control deposit shape, size, and morphology. The fact that deposition is localized beneath the nozzle and the equivalent etching is spread across most of the substrate means that significant local topography is developed.

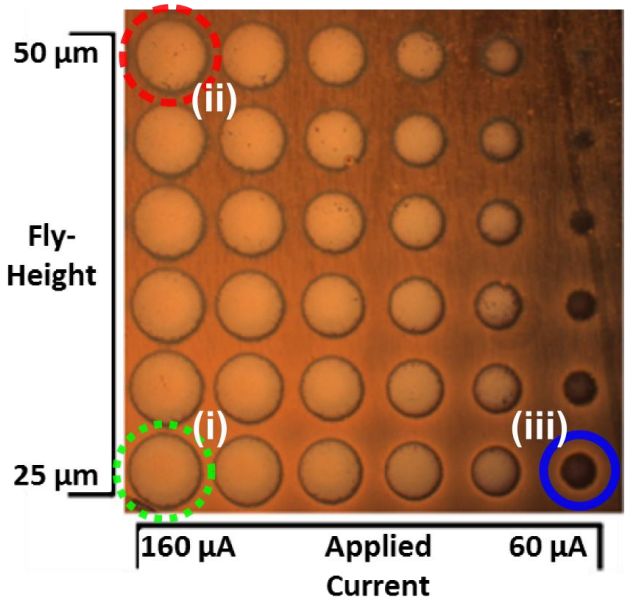

Figure 2.3. Array of copper on copper electrochemical sculpting

Optical micrograph of an array of copper deposits on a copper substrate plated at a range of applied currents and nozzle fly-heights. Stylus profilometry scans were performed to determine the heights of the three circled deposits: (i) = 0.35 μm, (ii) = 0.24 μm, and (iii) = 0.07 μm.

We expect the most efficient bipolar electrochemistry condition to occur when the SBC has the highest ohmic resistance through the annular gap and the lowest charge transfer resistance on the substrate. The ohmic resistance through the annular gap between the nozzle and substrate ($R_{annular}$) is inversely proportional to the fly-height (H) through the relationship

$$R_{annular} \sim \frac{ln(r_o/r_i)}{2\pi\kappa H} \ , \tag{2.10}$$

where all the variables have been defined previously. Likewise, the role of applied current on charge resistance can be represented as

$$R_{CT,red} \sim \frac{RT}{I_{app} nF}, \tag{2.11}$$

if one assumes a Tafel kinetic approximation for the high current density reduction region beneath the nozzle. The balancing of these characteristic ohmic and charge transfer resistances is key to understanding all of the results, at least qualitatively.

Figure 2.3 shows the largest copper deposit occurs at point (i), and this is the spot with the smallest fly-height and highest applied current (i.e., highest ohmic resistance and lowest charge transfer resistance in Eqs. 2.10 and 2.11, respectively). For a given current, one sees that the amount of deposit declines when fly-height is increased. For example, profilometry scans show a height of 0.24 μm for deposit (ii) whereas the height of deposit (i) is 0.34 μm. The effect of fly-height on the amount of deposit is especially obvious at lower applied currents. For a given fly-height, the amount of deposition is significantly lower as applied currents decline, in part, because the total charge is proportional to the applied current for our constant dwell time experiments. Looking more quantitatively, however, we see that deposit (iii) has 37.5% less charge than deposit (i), however, the actual deposit is disproportionately smaller than expected for charge differences alone (e.g., the deposit height is only 0.07 μm with a smaller radius). This is partially caused by an increase in charge transfer resistance as applied current drops, per Eq. 2.11, but also the competing role of oxygen reduction beneath the nozzle reduces the Faradaic efficiency (we do not deaerate electrolytes for practical reasons). Previous work has explored the effect of background oxygen reduction, and we find it is in the range of 20-40 μA for this system[27].

The discoloration evident in the top right corner of the array suggests this region has experienced the greatest amount of background etching during localized deposition on the array.

This is consistent with the fact that we scan the SBC starting at the bottom left corner, move horizontally, return to the next row on the left side, and finish in the top right. Since bipolar electrochemistry requires an equal amount of etching for each dot of material deposited, the upper right hand corner was exposed to the most oxidizing scans before experiencing the protection of the cathodic region scanning near it.

We use FEM simulations to translate these qualitative observations into quantitative predictions regarding the current density and potential distributions at the bipolar electrode surface. Figure 2.4a shows the surface overpotential calculated for the three deposits highlighted in Figure 2.3. The surface overpotential curves show that simulations predict the highest localization occurs for the condition with highest applied current and lowest fly-height (i), as we discussed qualitatively using resistance arguments from Eqs. 2.10 and 2.11. As expected, decreasing the applied current (iii) results in less polarization of the bipolar electrode, while an increase in fly-height (ii) decreases the peak overpotential and produces a wider region of cathodic overpotential. Within the region of the nozzle inner radius, the overpotentials are several hundred millivolts and therefore exhibit Tafel behavior, as assumed in Eq. 2.11. However, the full nonlinear kinetics are required to describe the whole bipolar electrode behavior since there are regions along the radial dimension of the bipolar substrate where both branches are important, such as when the overpotential approaches zero, or goes positive. The point along the conductive substrate where $\eta_s(r) = 0$ is defined as the bipolar crossover point (*BPX*), shown by the arrows in Figure 2.4a. $\eta_s(r)$ is negative from the nozzle center to this point, resulting in reduction chemistry, and $\eta_s(r)$ is positive from *BPX* to the electrolyte meniscus, resulting in oxidation chemistry. The positive overpotential is small compared to the negative overpotential because it is spread out over a much

larger area than the microscopic nozzle. The location for the *BPX* point varies slightly with details of the SBC operating conditions.

Figure 2.4b shows simulations for the current density profiles for the three deposits highlighted in Figure 2.3. The current density profiles match the expected shape of the deposit. Again, full simulations show that the high current and low fly-height (i) conditions produce the most current localization beneath the nozzle. The qualitative trends predicted by comparing the resistances in Eqs. 2.10 and 2.11 are borne out in our full physics simulations.

Simulations can give us more insights than the simple scaling in Eqs. 2.10 and 2.11. For example, the total amount of current that passes through the substrate (I_e) can be evaluated by modifying Eq. 2.9; if we integrate the local current density from nozzle center ($r = 0$) to the bipolar cross-over point ($r = BPX$) we get the total amount of reduction current, which is equal and opposite in sign to the integrated oxidation current density from $r = BPX$ to the edge of the electrolyte meniscus at $r = R$. The bipolar current efficiency (*BCE)* is then calculated by dividing the current passing through the substrate (I_e) to the total applied current of the system (I_{app})

$$BCE = \frac{I_e}{I_{app}}. \tag{2.12}$$

Bipolar current efficiency calculations for the three deposits in Figure 2.3 are 93.08%, 84.57%, and 88.85% for (i), (ii), and (iii), respectively, putting quantitative numbers to the qualitative discussion above. As expected, the condition of highest current and lowest fly-height is the most efficient bipolar condition. These simulations, combined with the experimental evidence above, shows that a properly designed SBC operating with a facile kinetic system will route nearly all of the applied current through the bipolar electrode in the region directly beneath the nozzle.

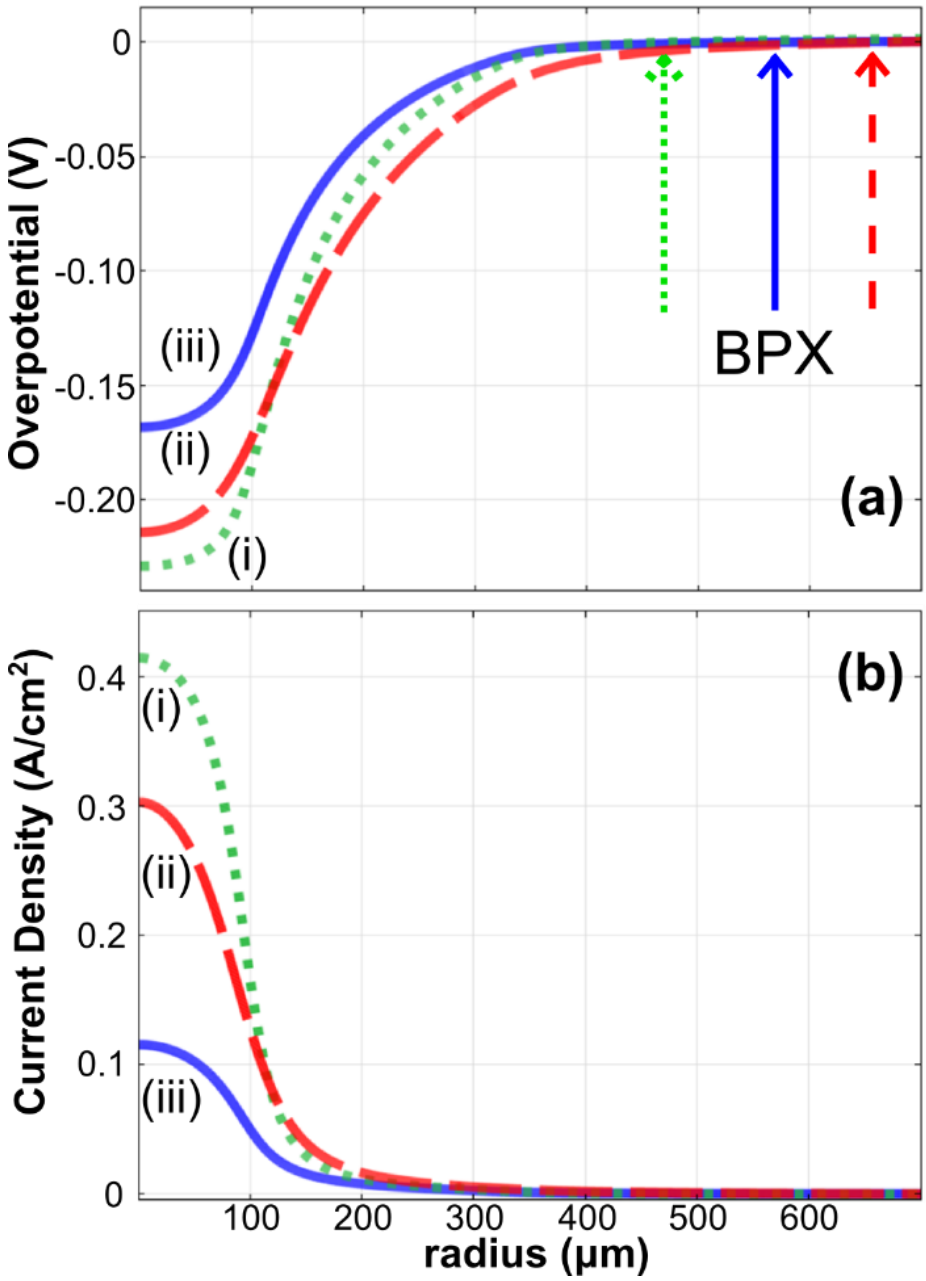

Figure 2.4. Simulations for copper on copper bipolar system

a. Computed surface overpotential profiles for the three deposits highlighted in Figure 2.3: (i) I_{app} = 160 μA and H = 25 μm, (ii) I_{app} = 160 μA and H = 50 μm, and (iii) I_{app} = 60 μA and H = 25 μm. The location where surface overpotential equals zero is defined as the bipolar crossover point (BPX); the BPX locations are identified by arrows for each case. **b.** Computed current density profiles for the same three conditions.

The locations of the *BPX* demonstrate how the SBC is able to achieve highly localized reduction while spreading the simultaneous substrate etching across a large area. The *BPX* for the three experiments shown falls between 450-700 μm from the nozzle center, whereas the feeder cathode is located 3.5 mm from the center. This results in a peak reduction current density about 500 times larger than peak oxidation current densities. As a result, a localized copper deposit 1 micron in height beneath the nozzle results in about 2 nanometers of copper etching across the far field. Repeated deposition and etching, and the patterned movement we use with the SBC, produces the background discoloration gradient seen in Figure 2.3. We have effectively removed the most materials from the upper right corner and redistributed it to the lower left corner of the image. Simulations let us understand nearly all the features of the experimental system, and this is a guide for future design of SBC nozzles, chemistries, and tool path planning.

To generalize our findings further, we define a dimensionless Wagner number (*Wa*) that captures the key balance between the annular ohmic resistance and cathodic charge transfer resistances described in Eqs. 2.10 and 2.11:

$$Wa = \frac{2\pi RT\kappa H}{I_{app} nF ln(r_o/r_i)} . \tag{2.13}$$

If the applied current followed a simple and uniform parallel splitting of current flow via the ionic vs electronic paths, then the dimensionless *BCE* would scale with *Wa* in the following manner:

$$\text{BCE} \sim \frac{1}{1+Wa} . \tag{2.14}$$

Figure 2.5 shows the relationship between *Wa* and the *BCE* for our computations, but is plotted in a form suggested by the simple scaling arguments in 2.14, namely (1-*BCE*)/*BCE* vs. *Wa*. We plot these dimensionless properties over experimentally achievable ranges for our SBC tool.

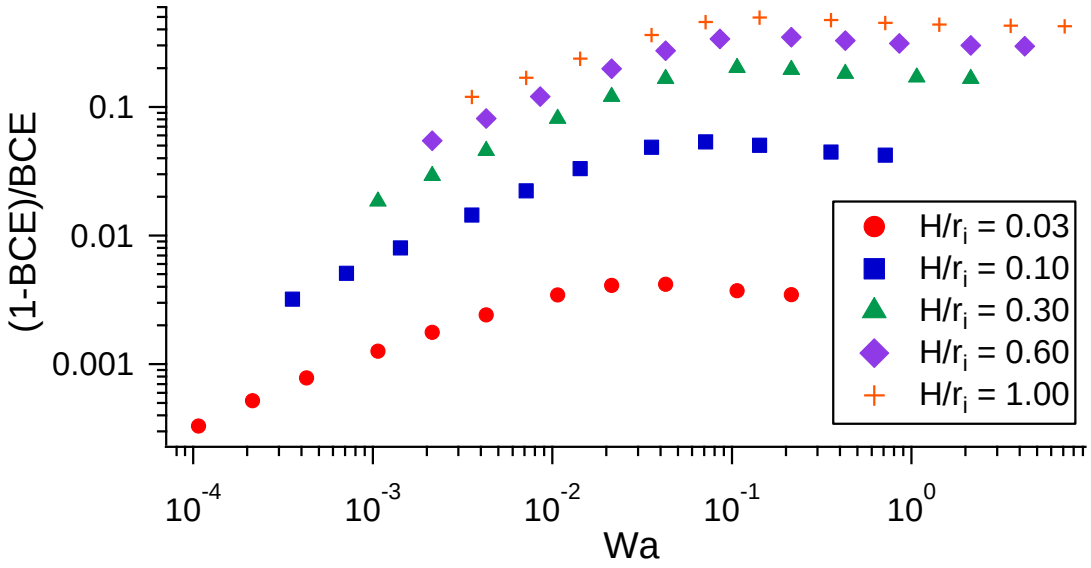

Figure 2.5. *BCE* vs *Wa* scaling relationship

The computed bipolar current efficiency (*BCE*) is shown over a wide range of Wagner numbers (*Wa*) and SBC geometries (H/r_i).

As expected, in the limit of small *Wa*, we approach the linear dependence implied by adherence to a highly localized parallel current pathways scaling implicit in Eq. 2.14. As *Wa* increases, the *BCE* value plateaus, because the applied current density becomes so small that the characteristic charge transfer resistance reaches a fixed value (set by the linearized charge transfer resistance, which is independent of applied current). Each specific SBC geometry (denoted by the ratio of H/r_i) produces a separate curve with a similar shape. Based on the systematic behavior of the family of curves seen in Figure 2.5, it seems likely that there is a more "universal" scaling than represented by Eq. 2.14, though we have not explored that here.

The scanning bipolar cell is able to do basic additive metal micropatterning without needing an electrical connection to the substrate. Figure 2.6a shows an optical micrograph consisting of 211 individual copper deposits on a copper substrate micropatterned in the form of the Cu elemental symbol. In this experiment, the applied current was held constant at 175 μA and

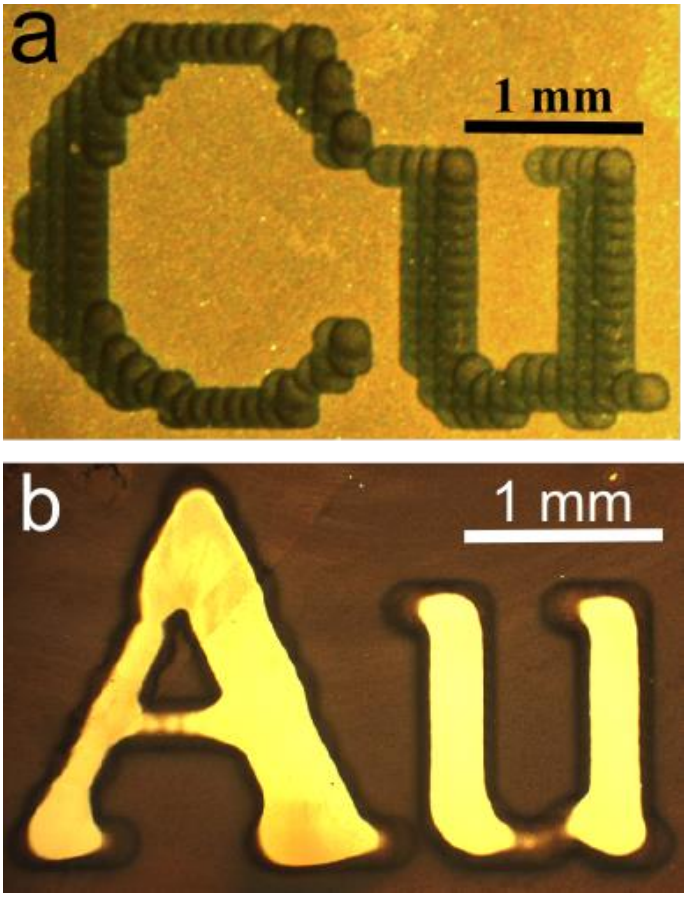

Figure 2.6. Patterning by bipolar electrochemical sculpting

Optical micrograph of **(a)** patterned copper deposition on a copper substrate using the SBC and **(b)** patterned copper etching through a 200 nm copper film to the gold underlayer using the SBC.

H was constant at 15 μm. The electrolyte flowrate was 400 μL min^{-1}, deposition time was constant at 2 seconds per deposit, and the deposits were spaced 100 μm center to center.

Of course, the same scanning bipolar cell can carry out localized oxidation and broad far-field plating. Figure 2.6b shows an optical micrograph where the applied current was reversed, and localized etching of the copper substrate created a micropattern of the Au elemental symbol (here gold is an etch stop that underlies the copper film). For this experiment, applied current was held at -100 μA and *H* was again constant at 15 μm. The electrolyte flowrate was 400 μL min^{-1}, etching

time was constant at 2 seconds per localized etch. The localized etches were spaced 100 μm center to center. The micropattern consisted of 224 individual localized etch pixels. Approximately 200 nanometers of copper was oxidized in order to expose the gold layer underneath. The optical micrograph also shows a consistent dark copper background which is a result of the simultaneous low current density copper reduction occurring macroscopically on the substrate.

2.5 CONCLUSION

The low conductivity electrolytes and geometry of the micro-nozzle configuration provides an ideal platform for performing bipolar electrochemical reactions on a conductive substrate. High ohmic drops through the annular gap between the microjet nozzle and the substrate allows for an alternate current pathway through the bipolar electrode. Proof of this concept was demonstrated through copper deposition on a copper substrate, under conditions where there were negligible concentration gradients. Finite element simulations were utilized to evaluate the coupling between the ohmic and charge transfer resistances of the SBC as well as provide quantitative analytical parameters to describe the system through the *BPX* and *BCE*. Surface patterning also demonstrates how the spatial and temporal control of bipolar electrochemistry can be coupled with motion control, to direct local chemistry without an electrical contact to the substrate. The scanning bipolar cell represents a new class of remote control electrochemistry.

Because the behavior of the SBC is governed by a secondary current distribution, the fundamental scaling traits of this system are set by the geometry of the SBC (r_i, r_o, H), the conductivity of the electrolyte, and the applied current, as grouped into the dimensionless form shown in Figure 2.5. This means that the SBC is scalable to nanoscopic dimensions, until either continuum transport assumptions breakdown or the geometric traits of the SBC approach the

Debye length for the electrolyte. Practical scaling limitations may be more important than the theoretical limits just described. For example, fabrication and nanopositioning of nanoscale nozzles requires much more sophistication than attempted here. But, these limitations are similar to those found in many scanning probe methods, and thus, we look forward to the future of much higher resolution bipolar electrochemistry than previously encountered.

Chapter 3. BIPOLAR ELECTROCHEMICAL DISPLACEMENT

3.1 SUMMARY

Bipolar electrochemical displacement (BED) enables direct-write electrodeposition on a conducting substrate that has no electrical connection. We demonstrate this phenomenon using nickel deposition coupled to the equal and opposite displacement of copper. The driving force for BED is the solution potential gradient generated by a specially configured rastering microjet electrochemical cell. BED is self-limiting based on the quantity of metal available for displacement from the substrate. Finite-element method simulations are used to show how the coupling between solution ohmic drop and charge transfer kinetics control bipolar efficiency and spatial segregation of the electrochemistry. Experiments and simulations show that the electrodeposition of nickel is largely dictated by the potential gradients in the microjet region, and largely unaffected by details of copper etching far from the microjet. Simple analytical scaling arguments explain most of the experimental trends.

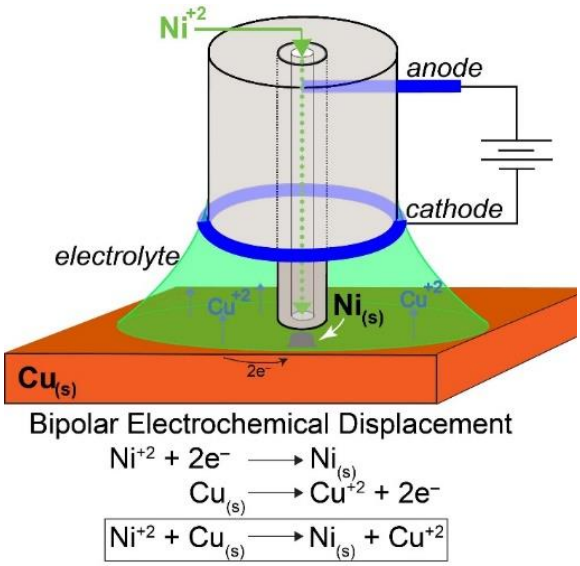

Figure 3.1. Bipolar electrochemical displacement

3.2 INTRODUCTION

We've recently made the first demonstration of locally-controlled microscopic bipolar electrodeposition on electrically isolated, macroscopic conducting substrates using a scanning

bipolar cell (SBC)[44]. The SBC geometry induces a high local potential variation in the electrolyte, even when using electrolytes with conductivities similar to standard electrodeposition baths[29]. The previous study's redox chemistry was the highly reversible copper system, where localized copper reduction occurred beneath the SBC tip and equal, but opposite, oxidation of the copper substrate occurred in the far-field, effectively letting the scanning tip sculpt the surface by redistributing copper from the far-field to the region beneath the SBC.

In this chapter, we explore the use of the SBC to carry out a phenomenon we call bipolar electrochemical displacement. The analogy is with traditional galvanic displacement reactions, where a more noble metal ion in solution displaces a less noble reduced metal by an equal and opposite charge transfer reaction. In galvanic displacement chemistries, the thermodynamic driving force causes spontaneous growth of the noble metal until the less noble material is completely consumed or densely capped. With the SBC, we can drive a displacement chemistry when the thermodynamics are unfavorable. In this case, the reaction is driven by the potential variation in solution, and this has the advantage that we can create stable electrolytes and use the spatial and temporal control of the SBC to start, stop, and pattern an electrically floating substrate. When done thoughtfully, this is a self-limiting displacement controlled by the total amount of sacrificial metal available. Here, we demonstrate the ability of the SBC to perform local bipolar electrochemical displacement reactions by growing nickel deposits on a thin copper sacrificial substrate.

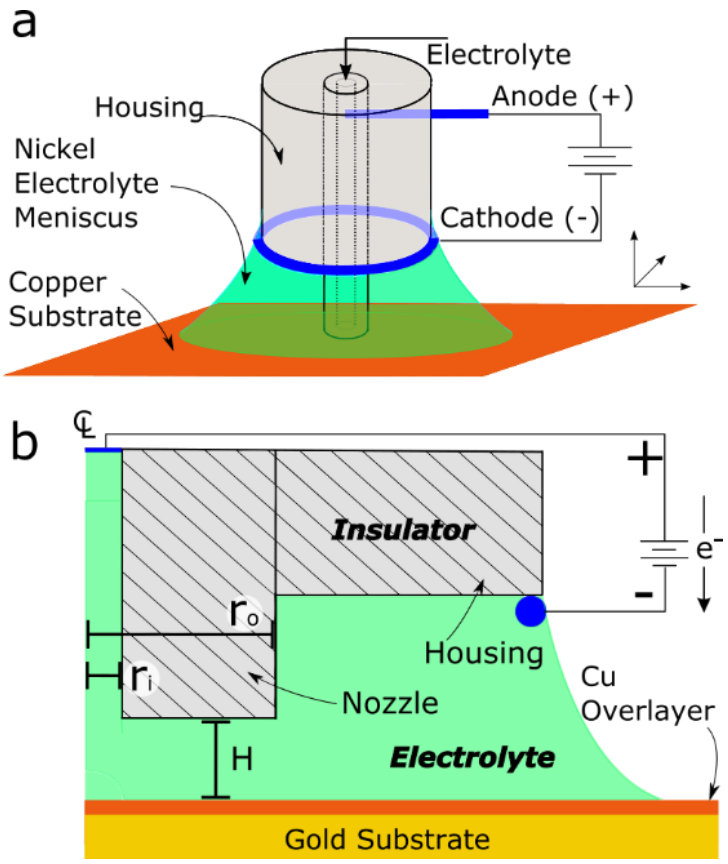

Figure 3.2. Schematic for bipolar electrochemical displacement

Illustration showing key features of the scanning bipolar electrochemical cell (SBC). **a.** Perspective view of the physical system. **b.** Definition of key geometric parameters in the axisymmetric computational domain.

3.3 Experimental Section

3.3.1 *Scanning Bipolar Cell (SBC)*

Figure 3.2a shows a perspective view schematic of key features in the SBC system used in the bipolar electrochemical displacement reactions. Nickel electrolyte flows through a microjet nozzle, passing by an internal platinum feeder anode before jetting onto the copper bipolar substrate. The electrolyte pools on the conductive substrate, and forms a liquid meniscus that

contacts the platinum feeder cathode fixed to the acrylic housing of the microjet nozzle, completing the electrochemical cell. The reaction at the feeder anode is water oxidation. Either nickel reduction or hydrogen reduction are the dominating reaction at the feeder cathode. Figure 3.2b further depicts the key geometric features and axisymmetric configuration used in finite element simulations (FEM) for the case $H = 2r_i$. The nozzle inner (r_i) and outer (r_o) radii and the fly-height of the nozzle above the substrate (H) dictate electrochemical behavior in the SBC by tailoring the ohmic resistance beneath the annular gap of the nozzle. For our experimental system we use a microjet nozzle with an inner radius of 100 μm and an outer radius of 335 μm. Flow rates for all experiments were held constant at 400 μL min^{-1}. The SBC deposition experiments performed here use a single nozzle to perform a serial write process; we found this simple geometry valuable for our prior development of Electrochemical Printing (EcP)[26-30]. However, like EcP, we expect the design of a SBC with multiple independently addressable electrodes should follow principles laid out in our prior work on the design of parallel print heads to accelerate patterning[77].

3.3.2 *Bipolar Plating Electrolytes*

Here we demonstrate bipolar displacement using a nickel electrolyte unmodified from previous use in electrochemical printing (EcP)[26-30]. The nickel electrolyte contains 0.3 M $NiSO_4$, 0.014 M sodium acetate, and 0.04 M acetic acid. Electrolyte conductivity is 2.1 S m^{-1} and pH is 3.95. We use a copper substrate to complete the bipolar redox couple and produce a bipolar displacement reaction. Thus, the bipolar electrochemical system is:

$$Reduction: \quad Ni^{+2} + 2e^- \rightarrow Ni_{(s)} \tag{3.1}$$

$$Oxidation: \quad Cu_{(s)} \rightarrow Cu^{+2} + 2e^- \tag{3.2}$$

$$Net: \quad Ni^{+2} + Cu_{(s)} \rightarrow Ni_{(s)} + Cu^{+2}.$$

The net reaction shows displacement of copper metal by nickel ions in solution similar to traditional galvanic displacement reactions. Except here, displacement is driven by potential variation in solution instead of by a spontaneous thermodynamic driving force. To simplify tool operation and use, we do not deareate our electrolytes. As a result, small amounts of copper etching will occur if the substrate is left in solution for significant periods of time. Moreover, our electrolyte metal assays show trace amounts of copper in the as-purchased nickel salts. As a result of trace Cu^{+2} from the salts and etching, our copper substrates have fairly stable open circuit potentials close to the reversible potential for the copper redox system.

3.3.3 *Bipolar Electrode Substrate Preparation*

To carry out the bipolar displacement reactions a copper thin film with a known number of available Coulombs was used as the bipolar electrode. Silicon wafers with 50 nm gold on a 5nm titanium adhesion layer were prepared using an E-beam evaporator at the University of Washington Nanofabrication Facility (WNF). Prior to copper electrodeposition, the gold substrates were cleaned via 20 cyclic voltammetry sweeps at 50 mV s^{-1} from -250 to 1500 mV vs SCE in a 1 M H_2SO_4 solution with a Pine Model AFRDE5 Bi-potentiostat. Gold substrates were then rinsed with DI water and dried with N_2 gas. Electrodeposition of bright copper on the clean gold substrates was carried out in a 0.24 M $CuSO_4$, 0.4 M H_2SO_4, and 1.4 mM HCl electrolyte using the same bi-potentiostat. The substrate electrodeposition step was carried out galvanostatically at 25 mA cm^{-2} with a platinum counter electrode. Plating time was varied to create copper substrates with differing total copper material. The coulombs of copper served to limit the total displacement reaction possible. Plated copper substrates were immediately removed from the electrolyte solution to avoid corrosion and were rinsed with DI water and dried with N_2 gas. All electrodeposition steps were carried out at room temperature. Substrates are masked to make a

circular exposed area of 19.6 mm^2. For the electrolyte flow rates and small number of printed features/movement used here, the meniscus is pinned on the SBC feeder cathode/outer nozzle housing. As the droplet of pooled electrolyte grows during electrolyte injection, it drains over the much larger masked substrate.

3.3.4 *Characterization Tools*

An Olympus BX51 optical microscope with an Olympus QColor3 digital camera using 5.0X and 10X objectives was used to take optical micrographs of each sample. An Oakton model no. 510 pH/ conductive meter was used to measure pH. Electrolyte conductivities were measured with a Mettler Toledo S230 conductivity meter with an Inlab 738 ISM probe. A FEI Sirion XL30 SEM was used for scanning electron microscopy of nickel deposits and copper thin films.

3.3.5 *Simulation Methods*

Secondary current distribution simulations were performed in the axisymmetric 2D computational domain shown in Figure 3.2b. These simulations determine relevant current flow pathways through the electrolyte and the extent of bipolar electrochemistry through the substrate. All governing equations and boundary conditions are the same as for our reversible copper system[44] except for at the conductive substrate, where now we must consider two chemistries.

A secondary current distribution is appropriate here because the concentration is substantially uniform for the microjet configuration used (limiting current densities can exceed 10 A cm^{-2}, so it is reasonable to neglect concentration gradients for all of our experiments)[27]. For this secondary current distribution problem, Laplace's equation governs the potential distribution (ϕ) in the electrolyte domain

$$\nabla^2\phi = 0. \tag{3.3}$$

The nozzle, housing walls, and electrolyte meniscus are treated as insulating boundary conditions,

$$\boldsymbol{n} \cdot \nabla \phi = 0. \tag{3.4}$$

The boundary condition for the feeder anode at the microjet inlet is given as

$$-\kappa \boldsymbol{n} \cdot \nabla \phi = \frac{I_{app}}{A_{nozzle}}, \tag{3.5}$$

and the feeder cathode boundary condition is

$$-\kappa \boldsymbol{n} \cdot \nabla \phi = \frac{-I_{app}}{A_{cathode}}, \tag{3.6}$$

where κ is the electrolyte conductivity, $\boldsymbol{n}$ is the unit normal vector pointing out of the computational domain, A_{nozzle}, is taken as the area of the nozzle where the current is applied, and $A_{cathode}$ is the area of the outer ring cathode.

Nickel reduction is taken as irreversible, so we use the cathodic Tafel branch with kinetic data taken from the literature[78]. As mentioned above, trace Cu^{+2} means the open circuit potential of the substrate is dominated by the copper redox chemistry due to its greater reversibility. We deal with the uncontrolled, trace copper in a manner that is easy to implement, produces results that are consistent with all experimental measurables (such as open circuit potential, current efficiencies, threshold voltages/currents, etc.) and whose magnitude (within reasonable bounds) has negligible influence on the computational results we report. Specifically, we use a Butler-Volmer form for the reversible copper chemistry, and set a small limiting current for copper reduction (in this case, $0.01 i_{o,Cu}$). With this *ad hoc* treatment of the small amounts of copper reduction possible in this system, we get the boundary condition for total current density on the bipolar substrate as

$$i = \frac{i_{o,Cu}e^{(\alpha_{Cu}f\eta_{s,Cu})} - i_{o,Cu}e^{(-(1-\alpha_{Cu})f\eta_{s,Cu})}}{1+\frac{i_{o,Cu}}{0.01i_{o,Cu}}e^{(-(1-\alpha_{Cu})f\eta_{s,Cu})}} - i_{o,Ni}e^{(-(1-\alpha_{Ni})f\eta_{s,Ni})} \quad (3.7)$$

where the room temperature parameters for nickel and copper are assumed to be: $i_{o,Ni}$ = 2x10^{-6} mA cm^{-2}, $i_{o,Cu}$ = 3.35 mA cm^{-2}, α_{Ni} = 0.5, α_{Cu} = 0.73, and f = 77.89 V^{-1} since both reactions transfer two electrons[75,78].

The surface overpotential for redox reaction j (copper or nickel-related charge transfer) in Eq. 3.7 is[76]

$$\eta_{s,j} = V_m - \phi(r) - E_j^{eq} \quad (3.8)$$

The potential at the surface ϕ is shown explicitly as a function of the radial position, while the "equilibrium" potentials E_j^{eq} are estimated for this system through a Nernst approximation, and the open circuit mixed potential of the conductive substrate (V_m) reflects the kinetics and thermodynamics of the reactions when current and $\phi(r)$ are equal to zero.

The bipolar electrode must have equal and opposite oxidation and reduction reactions to remain charge neutral, which can be expressed by the integral constraint over the area of the electrode

$$I_{e,net} = 2\pi \int_0^R irdr = I_{e,red} + I_{e,ox} = 0 \quad (3.9)$$

where i is defined by Eq. 3.7. Here, $I_{e,net}$ is the net electronic current passing through the bipolar substrate, which must be zero when integrated over the whole electrode. The quantities $I_{e,red}$ and $I_{e,ox}$ are the equal and opposite reduction and oxidation currents occurring on the bipolar substrate that, although spatially segregated, must add to zero over the entire floating substrate.

Mesh refinement in the regions of high gradient was used so that the overall charge balance in the system and the substrate integral on the bipolar electrode both converged to less than 0.01%

error. Grid refinement to achieve this level of charge balance resulted in about 800,000 mesh elements and a computational time of approximately 5-10 minutes for a typical converged solution. All simulations converged for realistic geometric conditions, however, as fly-height was reduced system gradients beneath the nozzle increased and mesh refinement became more substantial in the annular gap region in order to meet charge balance constraints. All simulations were performed on a Lenovo ThinkCenter model M7052-C9U with an Intel Core i7-2600 CPU @ 3.40 GHz and 8 GB Ram using a Windows 7 Professional 64-bit operating system. Finite element method (FEM) simulations were performed using COMSOL version 4.4 software with the heat transfer in fluids module.

3.4 Results and Discussion

Relevant current pathways through the electrolyte domain in Figure 3.2b (ionic current I_i) and through the conductive substrate (electronic current I_e) have been detailed previously for the SBC with a reversible copper system and also apply to the bipolar system in Eqs. 3.1 and 3.2 [44]. The fraction of the total applied current that passes through the substrate and participates in bipolar electrochemical reactions is the bipolar current efficiency (*BCE*)

$$BCE = \frac{-I_{e,red}}{I_{app}} . \tag{3.10}$$

Nickel deposition on a copper substrate requires a substrate polarization equivalent to the thermodynamic difference we estimate between the equilibrium potentials for nickel (-0.265 V) and copper (0.251 V). Without this minimum polarization potential (ΔE_{min}), neither reaction can occur and all applied current will proceed to the feeder cathode as ionic current through solution. The minimum potential is related to the minimum applied threshold current (I_{min}) by

$$I_{min} = \frac{\Delta E_{min}}{R_{annular}} \tag{3.11}$$

where $R_{annular}$ is the ohmic resistance through the annular gap beneath the nozzle and is related to nozzle geometry and electrolyte conductivity (κ) by

$$R_{annular} \sim \frac{ln\left(r_o/r_i\right)}{2\pi\kappa H}. \tag{3.12}$$

Once the threshold current for a given geometry is achieved, appreciable current can begin to pass through the copper substrate via bipolar charge transfer reactions. When bipolar current flow is active, this system has two separate charge transfer resistances; one for nickel reduction beneath the nozzle and one for copper oxidation across the far-field substrate. The dominant charge transfer resistance is from nickel deposition in the region within the nozzle inner radius and can be approximated by

$$R_{CT,red} \sim \frac{RT}{I_{app} nF}, \tag{3.13}$$

assuming a Tafel kinetic approximation for the high overpotential nickel reduction region beneath the nozzle. The balance between ohmic resistance across the annular electrolyte region and nickel charge transfer resistance will dictate, to first order, the current pathways and efficiency of the bipolar electrochemical system.

Figure 3.3a shows the qualitative effects discussed above for bipolar displacement of nickel on a thick copper substrate. The horizontal axis of the optical micrograph depicts the effects of applied current (I_{app}) from 300 μA to 500 μA in 50 μA increments whereas the vertical axis shows the fly-height (H) from 20 μm to 36 μm in 4 μm increments. The deposition time was held constant at 10 seconds for each bipolar condition. The deposits are spaced 300 μm center to center. The substrate used here had a total of 120 mC of copper deposit, which is sufficiently large to ensure the substrate did not fully etch during the course of the experiment.

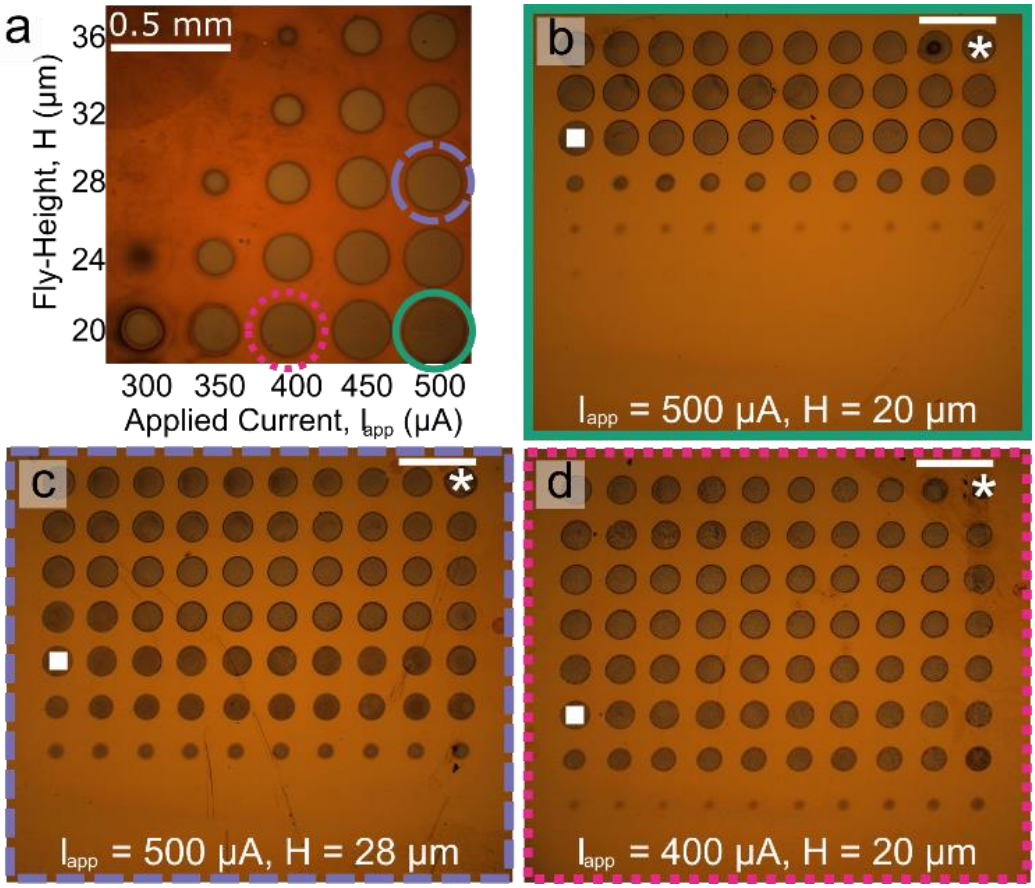

Figure 3.3. Bipolar electrochemical displacement arrays

Optical micrographs showing bipolar displacement of copper with nickel (all scale bars are 0.5mm). Circular dots are localized nickel deposits that have displaced copper from the substrate. **a.** Screening of operating conditions for bipolar displacement over a range of applied currents and nozzle fly-heights. **b-d.** Each image represents a different operating condition, repeated until all copper from the substrate (30 mC) has fully etched, terminating the bipolar displacement reaction.

Figure 3.3a shows that variation in applied current and fly-height affects the characteristic resistances in Eqs. 3.12-3.13. The most efficient conditions for bipolar electrochemistry should occur with the lowest charge transfer resistance (highest I_{app}) and highest annular ohmic resistance (lowest H). Qualitatively, we observe the most nickel deposition in the lower right corner of the array in Figure 3.3a, where the nickel deposit has the largest area. For a given applied current,

deposit size shrinks with increased fly-height, correlating with the lowering of electrolyte ohmic resistances. Similarly at a given fly-height, one sees a decrease in deposit area with decreased applied current mainly due to increased charge transfer resistance. In the upper-left region of the micrograph no nickel deposition is observed. Here, the substrate has not achieved enough polarization to overcome ΔE_{min} and none of the applied current appears to participate in bipolar electrochemical reactions. It is qualitatively clear that the minimum threshold current increases as the fly-height is increased, obeying the relationship in Eq. 3.11. This relationship predicts a threshold current of 160 μA for a geometry with H = 28 μm, whereas our experimental system shows an I_{min} between 300 and 350 μA at this condition. Eq. 3.11 assumes an idealized geometry, with square corners of the annulus and a perfectly flat substrate and nozzle end. Experimentally, our nozzles may have rounded edges, slanted nozzle ends, and error in actual fly-height that would result in smaller ohmic resistances than expected, requiring larger threshold currents to achieve adequate substrate polarization. Our experimental system also has competing oxygen reduction that reduces faradaic efficiency and is typically estimated to account for approximately 20-40 μA of the applied current.

Figure 3.3b-d show optical micrographs of constant deposition experiments that demonstrate the self-limiting nature of the displaced copper material on the bipolar electrodeposition of nickel when the copper layer is made thin (30 mC in this case). In each image, the copper material on the substrate is fully displaced from the substrate, causing nickel deposition to terminate before the whole 10x10 pattern is finished. Thus, the bipolar displacement of copper has a self-limiting behavior much akin to galvanic displacement, but in a driven system. Some of the nickel deposits (particularly towards the beginning of the array sequence) will deposit on top of the copper thin film, protecting the copper underneath from etching. Thus, slightly less copper

is being displaced than expected. We have never seen a printed nickel dot detach from the substrate as a result of copper etching beneath the printed feature. Figure 3.3b&c are done at the same applied current but different fly-heights with constant dwell times of 10 seconds per pattern location, producing an equal amount of total applied charge per deposit. The lower fly-height condition is self-limited after about 30 deposits whereas the higher fly-height requires 70 deposits before consuming all of the copper material. This is reflective of the lower bipolar current efficiency *(BCE)* at higher fly-heights, which means more of the applied current passes through the annular gap rather than the substrate, requiring more net applied charge to consume the copper material. This same effect is seen in Figure 3.3d, where a lower applied current increases charge transfer resistance, creating a more resistive pathway for current through the substrate and a smaller *BCE*.

The total number of nickel deposits necessary to fully displace the copper thin film from the substrate is an indicator for the *BCE*. Measuring the deposit areas provides an approach to estimating the *BCE* of these experiments. Deposition of the array begins in the upper-right corner, moves laterally to the left, then returns to the right side for the next row. Towards the end of the progression in Figure 3.3b-d the deposits decrease in size before eventually disappearing when copper material is fully depleted. The shrinking of nickel dots prior to the complete cessation of deposition results from increasing copper charge transfer resistance as copper material becomes scarce on the substrate. To improve our estimates of BCE, we "count Coulombs" for the nickel deposits in the region where they are uniform area (denoted in Figure 3.3b-d as the deposits from the * to ■ symbols). Our estimation for *BCE* is calculated from these optical micrographs using the equation

$$BCE \approx \frac{\left(\frac{A_{ud}}{A_{td}}\right)Q_{Cu}}{N_{ud} I_{app} \Delta t} \tag{3.14}$$

where A_{ud} is the area of the deposits inclusive of the regions denoted by * to ■, A_{td} is the total area of all visible deposits, Q_{Cu} is the total charge used to form the copper thin film on the substrate, N_{ud} is the number of uniform deposits inclusive of the regions denoted by * to ■, I_{app} is the total applied current, and Δt is the dwell time for each deposit. This "Coulomb counting" assumes that deposit thicknesses are uniform, a poor assumption that will systematically make our estimates for *BCE* using Eq. 3.14 smaller than reality for all experiments reported here. Using Eq. 3.14, we estimate *BCE* values of 17.8%, 10.2%, and 11.0% for Figure 3.3b, c, and d, respectively. The role of the minimum threshold current on the experimentally derived *BCE* values will be discussed later after first detailing simulations.

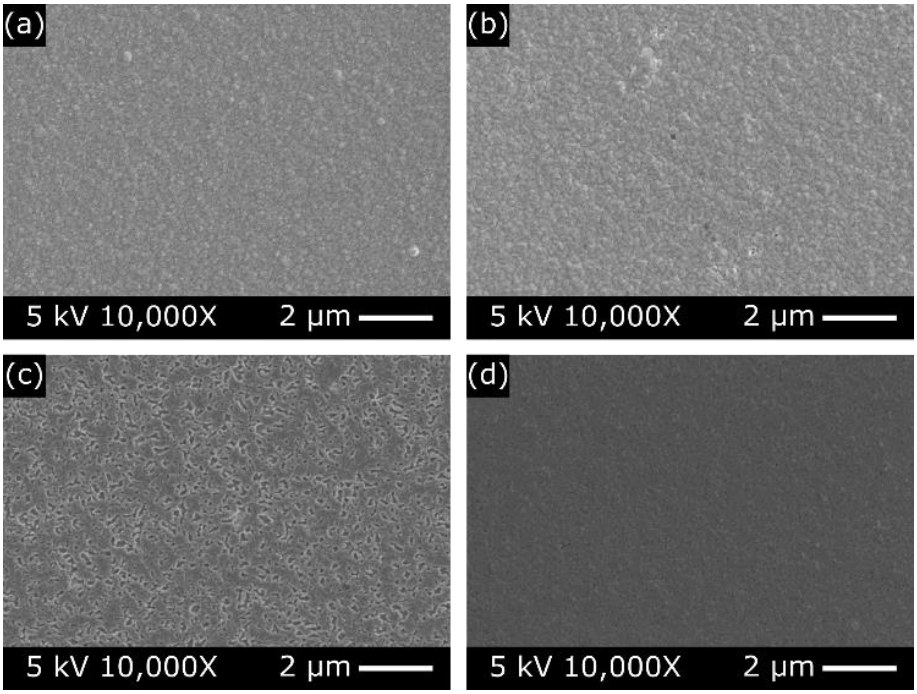

Figure 3.4. SEM of BED vs EcP patterns

SEM images comparing the morphologies of nickel on copper in the SBC configuration, where the substrate is electrically floating, and the EcP configuration where the substrate is the cathode. **a.** Nickel deposited by bipolar electrodeposition and **b.** nickel deposited by EcP. **c.** Copper far-field after deposition by bipolar electrodeposition and **d.** copper far-field after deposition by EcP.

SEM images were acquired to compare the morphology of nickel deposited in the SBC configuration where the substrate is electrically isolated versus more conventional microjet electrodeposition where the substrate is directly connected as the cathode of the cell (this is the EcP configuration). All of the applied current in the EcP configuration drives charge transfer on the substrate, whereas only the electronic current in the SBC configuraton drives charge transfer on the substrate. Thus, equivalent experiments require EcP applied currents that are scaled by the *BCE* for the given microjet nozzle geometry. Figure 3.4a-b show SEM images of nickel deposited by SBC (I_{app} = 400 μA, H = 28 μm) and EcP (I_{app} = 100 μA, H = 28 μm), respectively. The equivalent EcP value for I_{app} was estimated from Figure 3.3a, where $I_{min} \sim$ 300 μA. For both configurations, SEM shows dense nickel deposition with comparable morphology; deposition at comparable rates and overpotentials produces similar deposits regardless of how the overpotential develops on the substrate. However, Figure 3.4c-d show that there is a far-field effect on the copper substrate that differs by deposition method. With the SBC, Figure 3.4c, there is far-field oxidation and loss of copper, changing the surface morphology from fine grained bright copper to an etched surface with coarser morphology and a visually matte finish. By comparison, EcP has the whole substrate cathodically protected. There is negligible far-field chemistry, so the surface remains fine grained, Figure 3.4d, and the substrate remains bright.

We use FEM simulations to translate the qualitative observations into quantitative predictions regarding important bipolar electrochemical parameters. As described earlier, our simulations are analogous to those done previously for the reversible copper system except that the boundary condition at the substrate considers two chemistries. Figure 3.5 shows a plot of the total computed bipolar reduction current, $-I_{e,red}$, passing through the substrate for varying applied currents at two fly-heights. Each geometric condition has a minimum threshold current necessary

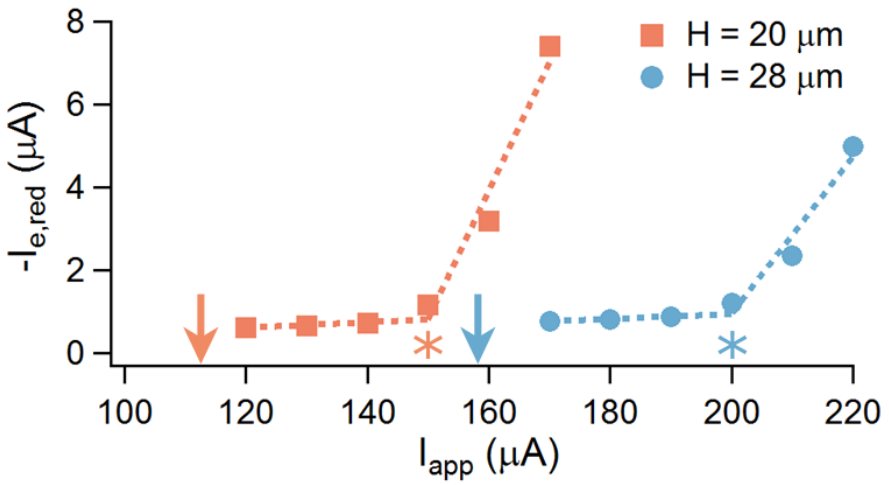

Figure 3.5. Computations for I_{min} values

Simulation showing the total bipolar reduction current passing through the conductive substrate as a function of applied current for two nozzle fly-heights. The star symbols indicate I_{min} values estimated by simulations and the arrows indicate I_{min} values calculated with Eq. 3.11.

to drive both bipolar reactions on the substrate. I_{min} is estimated in Figure 3.5 as the point where the total reduction current passing through the substrate begins to increase rapidly, indicated by the stars in Figure 3.5 at 150 μA and 200 μA for H = 20 μm and H = 28 μm, respectively.

The estimations for I_{min} in Figure 3.5 are higher than those calculated by Eq. 3.11 (indicated by arrows in the figure). Eq. 3.11 provides the threshold current at which the substrate has achieved enough polarization to drive nickel reduction and copper oxidation, whereas the computational estimates use the actual growth in current accounting for all the details of geometry and charge transfer. The exponential nature of charge transfer means that immediately after sufficient substrate polarization is applied, the kinetics (especially for nickel) are sluggish resulting in a high charge transfer resistance and low levels of bipolar electrochemistry. Additional current above the minimum substrate polarization threshold lowers charge transfer resistances so that appreciable bipolar electrochemistry occurs. Thus, our simulations are expected to better capture the reality of

our experiments, though basic scaling arguments like Eq. 3.11 are useful for understanding qualitative traits like the fly-height trend shown in Figure 3.5.

Bipolar electrochemistry involves equal and opposite reduction and oxidation that is spatially segregated across a substrate. The experiments in Figure 3.3 clearly show the equal and opposite nature of bipolar electrochemistry; nickel deposition stops when the copper is displaced completely from the substrate. The experiments also show the spatial segregation; nickel growth is localized whereas copper displacement is spread across the entire wetted electrode. Simulations let us better understand the details of both phenomena. Figure 3.6a shows three simulated current densities on the substrate in the vicinity of the SBC nozzle for the operating conditions used in Figure 3.3(b-d). The current density curves are a good representation of the expected shape for each bipolar nickel deposit (in the figure, we actually plot the negative of current density to emphasize that reduction produces deposit growth). Lower current densities are produced for the conditions used in Figure 3.3(c) and (d) than the conditions for Figure 3.3(b) because higher fly-heights and lower applied currents allow more ionic current to pass through the annular gap (i.e., producing less bipolar electrochemistry on the substrate). The radial position along the conductive substrate where the local current density equals zero is defined as the bipolar crossover point (*BPX*). From the nozzle center to this point, reduction chemistry dominates on the substrate, and from the *BPX* to the edge of the substrate, oxidation chemistry dominates. The magnitude of current densities for oxidation are much smaller than for reduction because it is spread over a much larger area than the microscopic nozzle. Integrating the current density on the substrate from the nozzle center to the *BPX* produces the quantity $I_{e,red}$ in Eq. 3.9 and Figure 3.5. Simlarly, integrating the (much lower, and oppositely signed) current density from the BPX to the edge of the substrate

produces $I_{e,ox}$, which of course, is equal and opposite to $I_{e,red}$. Once $I_{e,red}$ is known, *BCE* is then easily computed using Eq. 3.10.

Figure 3.6b shows the computed surface overpotentials ($\eta_{s,j}$) for nickel and copper across the entire bipolar substrate when the operating conditions match those in Figure 3.3b (I_{app} = 500

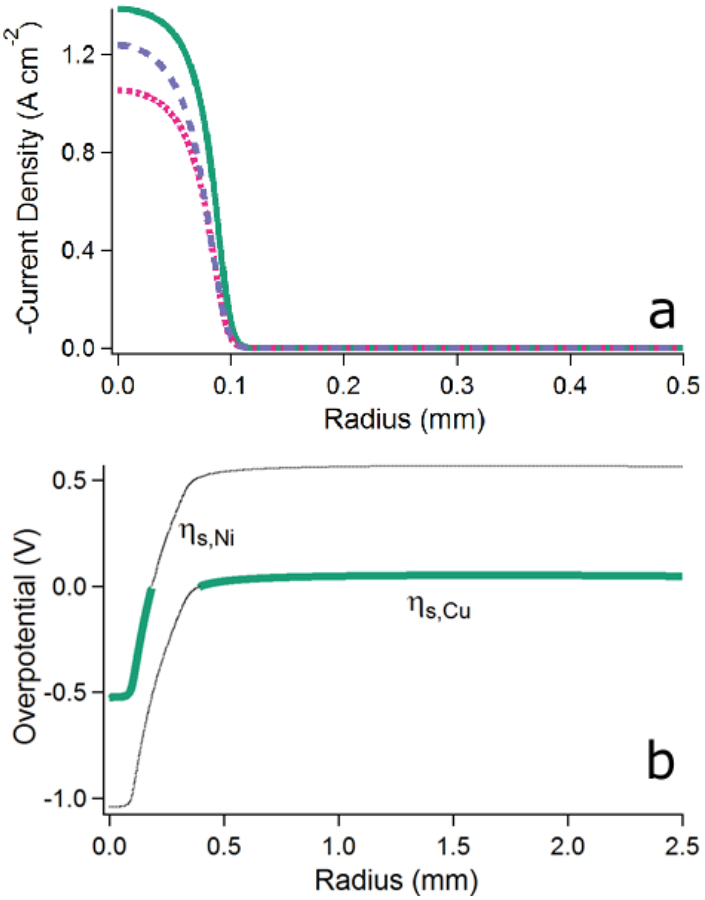

Figure 3.6. Current density and overpotential FEM computations

Simulation details showing the spatial variation of key bipolar electrochemical properties for the operating conditions used to produce Figure 3.3b (———), Figure 3.3c (– – – –), and Figure 3.3d (-------). **a.** Current density profiles in the vicinity of the nozzle for the three different operating conditions. **b.** Surface overpotentials for nickel and copper across the entire substrate for the conditions used in Figure 3.3b. Dark regions of each overpotential curve indicate the spatial regions where the dominant bipolar nickel reduction ($\eta_{s,Ni} < 0$) and copper oxidation ($\eta_{s,Cu} > 0$) occur.

μA and H = 20 μm). The dark curves indicate the regions on the substrate where the main bipolar electrochemistry occurs, namely, nickel reduction ($\eta_{s,Ni} < 0$) and copper oxidation ($\eta_{s,Cu} > 0$). In the regions with the light lines, little electrochemistry can occur for our system. Specifically, the modeled irreversibility of the $Ni_{(s)}/Ni^{+2}$ system means when $\eta_{s,Ni} > 0$ there is no anodic branch to the kinetic expression and therefore no oxidation chemistry. Likewise, since we have assumed trace Cu^{+2} and set a small limiting current density, even when $\eta_{s,Cu} < 0$ only a small limiting reduction current flows.

Both the current density profiles in Figure 3.6a and the darkened overpotential curves in Figure 3.6b show that significant reduction chemistry occurs beneath the nozzle region of the SBC, where the nickel reduction overpotential is several hundreds of millivolts. Though the oxidation chemistry is not visible in the current density plots on the scale given (it is 3 orders of magnitude smaller), the dark region of the copper overpotential curve shows that a few tens of millivolts of oxidation overpotential is spread over the entire substrate far-field where the copper slowly etches. The overpotential curves also show there is a gap beneath the nozzle where neither nickel reduction nor copper oxidation chemistries are present (between r = 0.185 mm and r = 0.396 mm). The potential drop spanning this gap is equal to the minimum potential difference to drive the bipolar pair. Rearranging Eq. 3.8 for each chemistry, we find that the gap corresponds to

$$\phi|_{\eta_{s,Cu}\to 0} - \phi|_{\eta_{s,Ni}\to 0} = E_{Ni}^{eq} - E_{Cu}^{eq} \tag{3.15}$$

as one expects, where the surface potentials are evaluated when the overpotentials for copper and nickel are equal to zero. From repeated simulations like those shown in Figure 3.6b, we find that the gap where little chemistry occurs depends somewhat on details of the operating conditions, though two key features seem to be true: the cathodically polarized region where most of the reduction occurs is largely invariant across the operating conditions represented by Figure 3.3(b-

d) whereas the edge of the anodically polarized region near the SBC nozzle is somewhat sensitive to the operating conditions, though overall, that sensitivity has little impact on the total area polarized anodically.

We can further generalize our findings and start looking for more universal scaling behaviors in this system by defining a dimensionless Wagner number (*Wa*) that relates the annular ohmic resistance and cathodic charge transfer resistances described in Eqs. 3.12 and 3.13 as:

$$Wa = \frac{2\pi RT\kappa H}{I_{app} nF ln\left(r_o/r_i\right)}. \tag{3.16}$$

Though the real system has complex spatial segregation of chemistries, the scaling behavior is likely dominated by the parallel paths current can follow, either ionic current flow through the electrolyte in the annular gap or electronic current flow in the substrate via bipolar electrochemistry. Of course, a minimum polarization is required to "turn on" the bipolar electrochemistry pathway. If we assume a perfect parallel current path, with charge transfer resistance infinite until we achieve I_{min}, at which point we assume charge transfer resistance given by Eq. 3.13, the *BCE* can be written:

$$BCE = \frac{1-I_{min}/I_{app}}{1+Wa}. \tag{3.17}$$

Figure 3.7 combines many experimental estimates for *BCE* (using the methods shown in Figure 3.3) with many simulation results for the same operating conditions. We use the scaling relationship in Eq. 3.17 to plot the data as *BCE* vs 1 - I_{min}/I_{app}. In all cases presented here, $Wa << 1$, so we ignore that factor in the plotting of the data. We can expect to see linear behavior for *BCE* as a function of 1-I_{min}/I_{app}, which is indeed the case for both our experimental and simulated results. As discussed in Figure 3.3, the experimental methods we use are expected to systematically bias the bipolar current efficiencies we estimate lower than the actual *BCE*; that effect is clearly

evident here and provides a motivation to develop more quantitative methods for experimental determination of this critical performance metric. At the same time, we also observe that the simulated *BCE* values fall below the black line, which represents the relationship in Eq. 3.17 in the limit of *Wa* going to zero. Compared to the simple, uniform current distribution assumed to get Eq. 3.17, we see that the full current distribution problem introduces complexity that uniformly reduces *BCE*. For example, Eq. 3.17 ignores the anodic charge transfer resistance, as well as the edge of the cathodically polarized region where Tafel kinetics no longer hold (and hence, where the charge transfer resistance is effectively higher). Both of these effects reduce the *BCE* and are included in the simulation results, but not Eq. 3.17. Nonetheless, Eq. 3.17 provides key insights into the scaling of experiments and simulation, even if it is not quantitatively accurate.

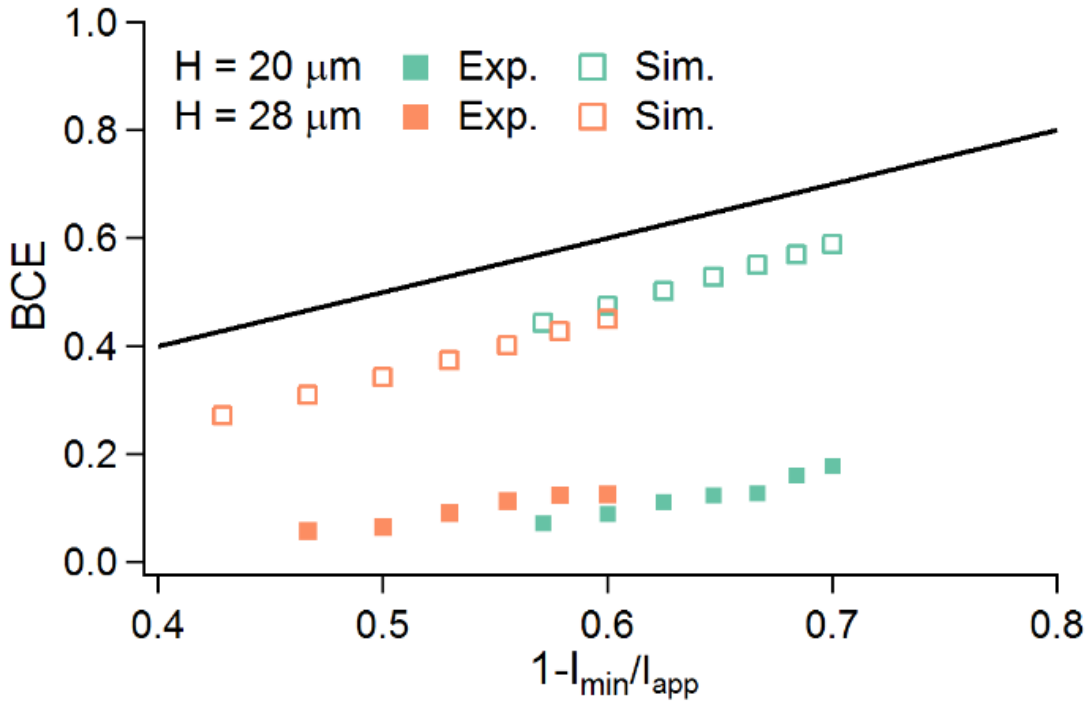

Figure 3.7. Computed and experimental BCEs vs $1\text{-}I_{min}/I_{app}$

Plot of experimental and computational bipolar current efficiencies as a function of $1\text{-}I_{min}/I_{app}$ for two different fly-heights. The black line represents the relationship in Eq. 3.17 in the limit of *Wa* going to zero.

The fundamental studies described here were driven by a desire to understand and implement bipolar electrochemical displacement in a simple axisymmetric geometry where the deposition occurs directly on a substrate uniformly coated by the displaced metal. However, for practical implementation, one would prefer to separately engineer the substrate for adhesion and other purposes, and not be limited by metals that are easy to displace. Figure 3.8 shows an alternative bipolar electrochemical displacement configuration that has the advantage of self-regulating displacement without the disadvantage of deposition on top of the displacing material. Figure 3.8a shows the SBC configuration schematically. We place an isolated copper material dot on the substrate far-field, away from the microjet nozzle where reduction occurs. We expect this configuration to also display bipolar electrochemical displacement, based on the results in Figure 3.6, where we saw that the cathodically polarized region was almost entirely dictated by the local nozzle geometry.

For these experiments, we repeatedly pattern the numbers “1 2 3”, each time with a different amount of copper material deposited in the far-field dot (we used 10, 20 or 30 mC of charge). Figure 3.8b (left panel, 10 mC of Cu) shows that the self-limiting nature of bipolar displacement means the nickel material electrodeposits directly on the gold substrate for the number “1”, but ceases to deposit the numbers “2 3” even though we continued to move the SBC and apply current in the pattern. Figure 3.8b (middle panel, 20 mC of Cu) shows that doubling the amount of copper dot lets the numbers “1 2” appear as the pattern is rastered by the nozzle, but not the full number “3” since the copper has been fully displaced. Finally, Figure 3.8b (right panel, 30 mC of Cu) lets us fully pattern “1 2 3”. In these experiments, the applied current was held constant at 450 μA and H was constant at 20 μm with a deposition time of 10 seconds for each displacement deposit. The deposits are spaced 75 μm center to center. Since each printed number (1 or 2 or 3)

consists of 25 individual deposits, we applied 112.5 mC of charge per printed number, meaning the *BCE* for this configuration was approximately 0.09. This *BCE* is only slightly lower than the experimental results shown in Figure 3.7 for the axisymmetric configuration. Thus, far-field details matter a little for the efficiency of this bipolar electrochemical displacement system, but not fundamentally.

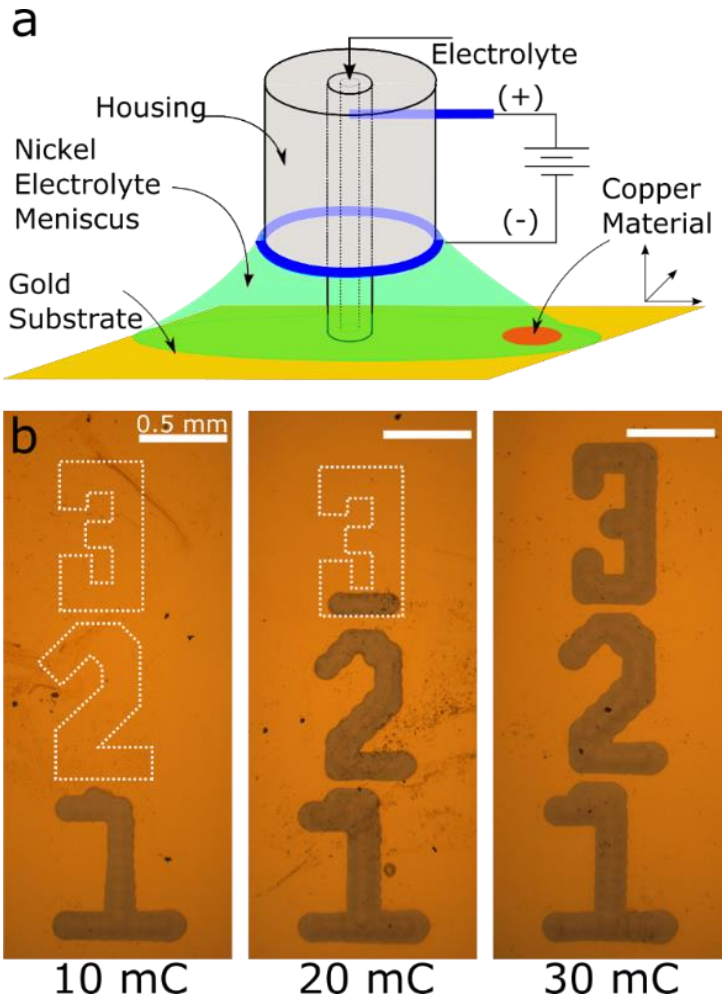

Figure 3.8. BED self-limiting nickel patterning

Demonstration of an alternative configuration for bipolar electrochemical displacement that separates the deposition substrate traits from the displaced material. **a.** Perspective view illustration of the SBC configuration using an isolated copper thin film. **b.** Optical micrographs of self-limiting bipolar displacement reactions at differing copper Coulombic quantities (all scale bars are 0.5 mm).

3.5 CONCLUSIONS

The equal and opposite nature of bipolar electrochemistry is ideal for driving electrochemical displacement reactions on an electrically isolated conductive substrate. These bipolar electrochemical displacement reactions are driven by the potential variation in solution and are spatially controlled by the geometric configuration of the scanning bipolar cell. Evidence and a detailed description of this phenomenon is demonstrated experimentally and through scaling arguments using nickel deposition on a copper substrate. Knowing the Coulombs of copper material on the substrate provides a technique to experimentally estimate the bipolar current efficiency of the SBC at a given set of experimental conditions. We also demonstrate the ability of the SBC to spatially pattern known quantities of nickel on the conductive substrate through displacement of an equal quantitiy of copper. FEM simulations help quantify experimental observations, provide detailed insights into the bipolar processes, and show how simple scaling can be used to describe trends. SEM demonstrates that the morphology of nickel deposited via bipolar electrochemistry is comparable to those deposited by more conventional electrodeposition methods. The SBC's major limitation is the low experimental bipolar current efficiencies, which can be somewhat mitigated by improved nozzle fabrication and fly-height motion control, but will ultimately always be less than electrodeposition connected to the substrate. The SBC provides a unique platform for spatially controlled bipolar electrodeposition on electrically isolated conductive substrates.

Chapter 4. REMOTE CONTROL ELECTRODEPOSITION: PRINCIPLES FOR BIPOLAR MATERIALS PATTERNING

4.1 SUMMARY

We describe electrolyte design for bipolar electrochemical growth and patterning of a range of materials on an electrically floating substrate using the scanning bipolar cell (SBC). In the SBC, bipolar electrodeposition is driven by local potential variation generated beneath a rastering microjet anode connected to a far-field cathode. Metal reduction occurs beneath the microjet when the substrate is approached, provided the electrolyte possesses a suitable reducing agent that undergoes oxidation across the substrate far-field. We use a series of metal reduction reactions (Ni, Cu, Au, Ag) that cover a wide range of nobility, and couple them to the oxidation of ascorbic acid or ferrous ion, depending upon the metal used. The reversibility or irreversibility of the local metal reduction reaction dictates details of the required electrolyte thermodynamics. For irreversible deposits (Ni, Au), there is a wide thermodynamic operating window for the bipolar counter reaction. Reversible deposits that are easily etched (Cu, Ag) have tight thermodynamic windows; deposit stability requires the use of metastable electrolytes. We provide a simple scaling relationship that incorporates the electrolyte thermodynamics, interfacial

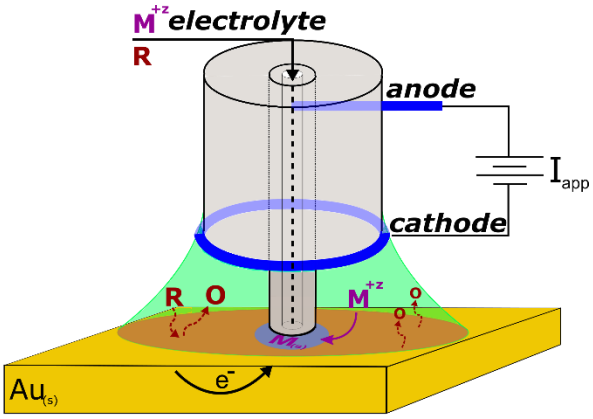

Figure 4.1. Remote control electrochemistry

charge transfer kinetics, and SBC operating conditions, then demonstrate its use through a 10X reduction in the spatial dimensions of local nickel reduction chemistry.

Chemistries Explored in Ch. 4:

$Local$: $Ni^{+2} + 2e^- \rightarrow Ni_{(s)}$
$Far\ Field$: $AA \rightarrow 2e^- + DHAA + 2H^+$
Net: $Ni^{+2} + AA \rightarrow Ni_{(s)} + DHAA + 2H^+$

$Local$: $Cu^{+2} + 2e^- \rightarrow Cu_{(s)}$
$Far\ Field$: $AA \rightarrow 2e^- + DHAA + 2H^+$
Net: $Cu^{+2} + AA \rightarrow Cu_{(s)} + DHAA + 2H^+$

$Local$: $[Au(CN)_2]^- + e^- \rightarrow Au_{(s)} + 2CN^-$
$Far\ Field$: $AA \rightarrow 2e^- + DHAA + 2H^+$
Net:
$[Au(CN)_2]^- + AA \rightarrow Au_{(s)} + DHAA + 2H^+$

$Local$: $Ag^+ + e^- \rightarrow Ag_{(s)}$
$Far\ Field$: $Fe^{+2} \rightarrow e^- + Fe^{+3}$
Net: $Ag^+ + Fe^{+2} \rightarrow Ag_{(s)} + Fe^{+3}$

4.2 INTRODUCTION

Previous work by our group showed that a rastering microjet anode system used for localized electrodeposition and patterning on a cathode[26-30] can be adapted for localized bipolar electrodeposition; the critical modification was adding a far-field cathode while leaving the substrate electrically isolated. We call this rastering microjet anode, with far-field cathode, the scanning bipolar cell (SBC)[44,45]. Mass transfer rates are extraordinary in our microjet configuration[27], so there is no appreciable concentration polarization, making the SBC mechanistically distinct from scanning electrochemical microscopy methods that rely on spatially confined concentration cells[79-84]. Initial applications of the SBC used an electrically-floating copper metal substrate as the electron donor and cupric ion containing electrolytes as the electron acceptor for the bipolar pair. As the copper substrate was oxidized in the far-field, electrons were donated to the equal and opposite local reduction of cupric ion (to copper) beneath the microjet. The result for the cupric/copper system was a “sculpting” of the originally planar copper

substrate[44]. Reduction of other metal cation-containing electrolytes beneath the microjet, while continuing to use far-field copper oxidation, resulted in "bipolar electrochemical displacement" (BED)[45]. BED is equivalent in many ways to galvanic displacement of one metal by another, but the thermodynamics can be "uphill". For example, using the local deposition of nickel (the less noble metal) by displacing an equal and opposite amount of far-field copper (the more noble metal) resulted in an atom-for-atom displacement, where the nickel was locally deposited while the copper etching occurred across the entire wetted substrate (assuming perfect Faradaic efficiency). In all these cases, the far-field area was 1000X greater than the microjet nozzle area, so each micron of nickel deposition etched a nanometer of copper in the far-field.

Generalizing bipolar electrodeposition in the SBC requires an alternative to far-field metal etching, so that the substrate remains unchanged while undergoing bipolar reactions. Here we address the full design of bipolar electrolytes for the SBC, where both the reduction and oxidation chemistries are optimized based on the thermodynamics of the system and desire to leave the far-field of the workpiece unaltered. We call this "remote control" electrochemistry, because it occurs without need for electrical connection to the substrate. We lay out the rules for tailoring efficient localized bipolar electrochemistry over a wide range of electrodeposition chemistries (from noble to base metals). Tailoring the electrolyte requires a detailed mating of the reduction and oxidation chemistries based on thermodynamic and kinetic constraints. The insights and principles laid out here can be easily extended to other bipolar electrochemical couples.

4.3 MATERIALS AND METHODS

4.3.1 *Scanning Bipolar Cell*

Figure 4.2a shows a perspective view configuration and key features of the electrochemical cell used for carrying out local bipolar electrochemistry on macroscopic, floating substrates. For the chemistries explored here, an electrolyte containing reducible metal ions (M^{+z}) and an electron donating reducing agent (R) is pumped through an electrically insulating capillary nozzle. A platinum feeder anode is inserted in the capillary, upstream of the nozzle exit where electrolyte jets onto the gold bipolar substrate. The electrolyte pools on the conducting substrate, forming a liquid meniscus that contacts the far-field platinum feeder cathode fixed to the acrylic housing of the microjet nozzle, completing the electrochemical cell. The nature of the solution potential contours beneath the microjet is such that, under the proper operating conditions, metal ions are reduced in the region directly beneath the nozzle and the reducing agent (R) is oxidized across the far-field of the substrate, resulting in the bipolar couple:

$$M^{+z} + ze^- \rightarrow M_{(s)} \tag{4.1}$$

$$R \rightarrow O + ne^- \tag{4.2}$$

$$Net: \quad M^{+z} + \frac{z}{n}R \rightarrow M_{(s)} + \frac{z}{n}O$$

The net reaction of Eqs. 4.1 and 4.2 looks superficially like a standard electroless deposition system, though we design the electrolyte thermodynamics to be either “uphill” or “downhill” depending on characteristics of the full bipolar electrochemical couple, as detailed in the main text (electroless deposition systems are always sufficiently “downhill” to overcome nucleation barriers).

The current flow and electrochemical behavior of the cell are dictated by the coupling of the solution ohmic resistance, bipolar couple thermodynamics, and charge transfer resistances of the bipolar couple as described previously for copper and nickel deposition on a copper substrate[44,45]. Figure 4.2b more clearly depicts the key geometric features and axisymmetric configuration of the SBC in the nozzle region. The nozzle inner (r_i) and outer radii (r_o) and the fly-height of the nozzle above the substrate (H), together with the electrolyte conductivity (κ), dictate the ohmic resistance through the annular gap between the nozzle and conducting substrate (unless noted otherwise r_i = 100 μm and r_o = 335 μm). When the resistance in the annulus of electrolyte between the nozzle and substrate is sufficiently high compared to the substrate charge transfer resistances, current will flow through the floating conductive substrate, driving bipolar electrochemical reactions

The SBC nozzle is cut from a 200 μm I.D. and 670 μm O.D. Polymicro microcapillary glass tube to a length of about 1 centimeter and epoxied into a Peek 1/4" fitting. The Peek fitting threads into a machined acrylic housing containing a platinum anode embedded approximately 3 centimeters upstream of the microcapillary outlet. The cathode is a 0.25 mm diameter platinum wire mounted concentrically (about 0.34 cm in diameter) on the acrylic housing (labelled "insulator" in Figure 4.2b) that holds the microcapillary. Current was sourced galvanostatically between the feeder anode and cathode with a Keithley 2400 sourcemeter. The total voltage between the electrodes is typically 10-100V for the various experiments. The nozzle fly-height is monitored with a Mightex USB camera. Fly-height is controlled by bringing the tip into contact with the substrate, moving the nozzle 300 μm sideways, and then stepping the nozzle up at 3 μm increments until the nozzle snaps back into position. This position is considered H = 3 μm.

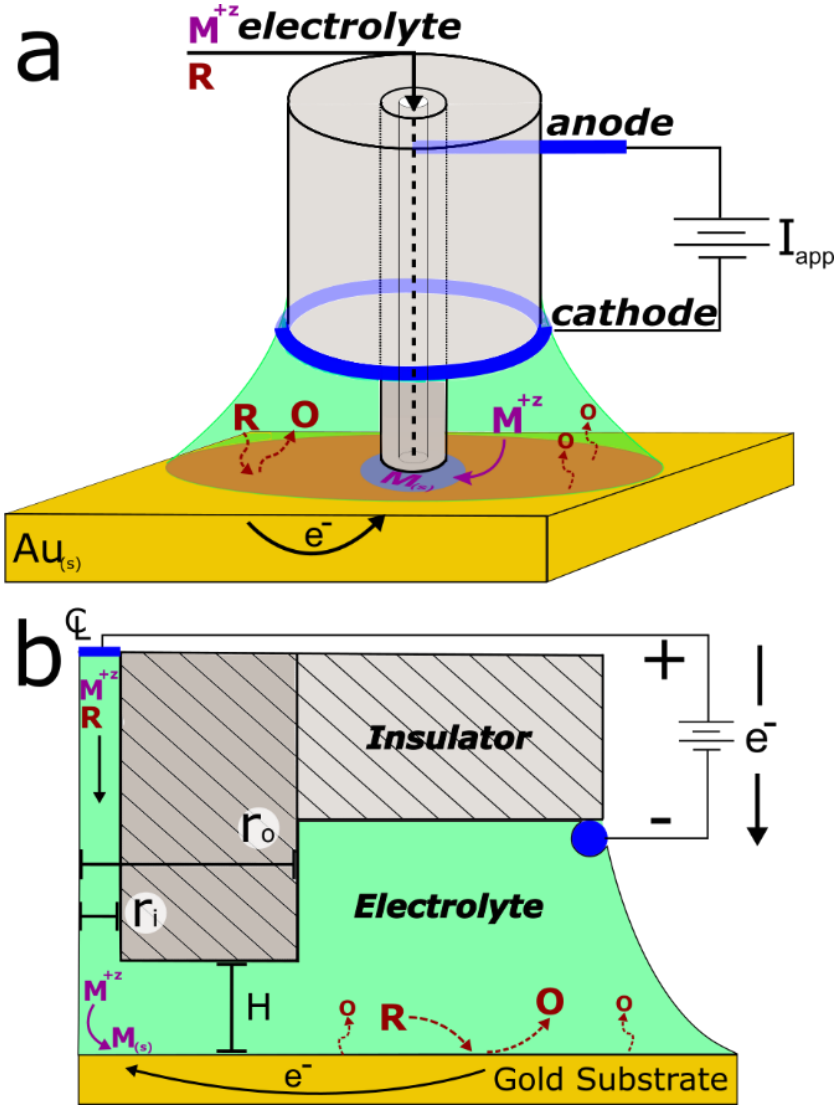

Figure 4.2. Remote control electrodeposition schematic

(a) Perspective view illustration of the Scanning Bipolar Cell (SBC) and important components. **(b)** Schematic of the to-scale axisymmetric geometric domain and key geometric features for the case where $H = 2r_i$.

4.3.2 *Chemicals*

Unless noted otherwise, the following chemicals were used as received: $NiSO_4 \cdot 5H_2O$ (Sigma Aldrich, 99-102.0%), L-ascorbic acid (Sigma Aldrich, 99%), $KAu(CN)_2$ (Sigma Aldrich, 99.99%), KOH pellets (Fisher Scientific, 89.1%), $CuSO_4 \cdot 5H_2O$ (Fisher Scientific, technical

grade), $AgNO_3$ (Sigma Aldrich, 99.0%), $FeSO_4 \cdot 7H_2O$ (Sigma Aldrich 98%), $Fe_2(SO_4)_3 \cdot 5H_2O$ (Sigma Aldrich, 97%), and concentrated H_2SO_4 (Mallinckrodt Chemicals, 95-98%). All aqueous electrolytes were prepared with high purity deionized (DI) water.

4.3.3 *Electrolytes for Bipolar Electrochemistry*

Here we demonstrate bipolar electrochemistry with the SBC using a variety of noble and base metal electrodeposition reactions. As detailed above, Eqs. 4.1-4.2, each electrolyte must contain metal ions for local deposition and an electron-donating reducing agent suitable for oxidation in the far-field of the gold substrate.

For metals that behave irreversibly (i.e., deposit much more easily than they strip), electrolytes were designed to be thermodynamically "uphill". The thermodynamic difference for the bipolar couple (ΔE_{BC}) is the estimated difference between the Nernst potential for the local reduction reaction minus the Nernst potential for the oxidation reaction in the far-field. Nickel electrodeposition, a fairly irreversible metal at moderate pH, used a bath modified from previous electrochemical printing studies, with ascorbic acid added as the far-field reducing agent. The bath composition was 0.1 M $NiSO_4$ and 0.01 M ascorbic acid (pH = 2.9). For the nickel electrolyte, the estimated bipolar couple thermodynamic potential difference was $\Delta E_{BC} \approx$ -0.59V (here, negative potentials denote thermodynamically "uphill"). Another irreversible system, gold deposition, used a basic electrolyte with cyanide complexation:

$$[Au(CN)_2]^- + e^- \leftrightarrow Au_{(s)} + 2CN^-. \tag{4.3}$$

To make the gold chemistry behave irreversibly, free cyanide concentration was kept low by using potassium hydroxide as the supporting electrolyte instead of potassium cyanide (which is typical of industrial plating baths)[4]. For ascorbic acid (AA) to be used as the far-field reducing agent the

pH must be less than the second pK_a value, so that AA can donate an electron. The pH value was set between 8-9 by titrating a solution of 0.02 M $KAu(CN)_2$ and 0.01 M ascorbic acid with 1 M KOH. We estimated $\Delta E_{BC} \approx$ -0.89V for this electrolyte formulation.

Unlike the previous electrolytes, copper and silver electrolytes were designed to have modestly "downhill" thermodynamics (i.e. $\Delta E_{BC} > 0$) to protect the (reversible) metal deposits from electrochemically oxidizing after deposition. The plating bath for copper deposition experiments consisted of 0.05 M $CuSO_4$ and 0.005 M ascorbic acid (pH = 2.6) with $\Delta E_{BC} \approx$ +10mV. Silver electrodeposition used a nitrate plating bath. Ascorbic acid is too strong of a reducing agent for Ag^+, resulting in nucleation and silver particle formation in solution. However, a suitable metastable bath was made using the Fe^{2+}/Fe^{3+} redox couple with the equilibrium potential tailored to the $Ag^+/Ag_{(s)}$ equilibrium potential. The silver bipolar plating bath consisted of 0.01 M $AgNO_3$, 0.01 M $Fe_2(SO_4)_3$, and 0.01 M $FeSO_4$ (pH = 2.3) with $\Delta E_{BC} \approx$ +80mV. Despite the "downhill" thermodynamics, both of these baths proved sufficiently stable for use in our bipolar electrochemical experiments.

4.3.4 *Bipolar Electrode Substrate Preparation*

All electrodeposition experiments were performed on gold substrates. Silicon wafers with 50 nm gold on a 5 nm titanium adhesion layer were prepared using an E-beam evaporator at the University of Washington Nanofabrication Facility. Prior to bipolar experiments, the gold substrates were cleaned via 20 cyclic voltammetry sweeps at 50 mV s^{-1} from -250 to 1500 mV vs SCE in a 1 M H_2SO_4 solution with a Pine Model AFRDE5 Bipotentiostat. Clean gold substrates were then rinsed with deionized (DI) water and dried with N_2 gas. Substrates were masked to make a circular exposed area of 0.45 cm^2. For the electrolyte flow rates and small number of printed features used here, the meniscus was pinned on the SBC feeder cathode/outer nozzle housing. As

the droplet of pooled electrolyte grew during electrolyte injection, it drained over the much larger masked substrate. All electrodeposition steps were carried out at room temperature.

4.3.5 *Characterization Tools*

An Olympus BX51 optical microscope with an Olympus QColor3 digital camera using 5.0X and 50X objectives was used to take optical micrographs of each sample. A FEI Sirion XL30 SEM was used for scanning electron microscopy of metal deposits. An Oakton model no. 510 pH/conductivity meter was used to measure pH.

4.4 RESULTS AND DISCUSSION

Figure 4.3 shows the qualitative effects discussed above for local nickel deposition on a gold bipolar electrode, where ascorbic acid (AA) is oxidized in the far-field to form dehydroascorbic acid (DHAA) and protons:

$$Ni^{+2} + 2e^{-} \rightarrow Ni_{(s)} \tag{4.4}$$

$$AA \rightarrow DHAA + 2H^{+} + 2e^{-} \tag{4.5}$$

The estimated reduction potentials for nickel and ascorbic acid are $E_{Ni}^{eq} \approx$ -0.28V and $E_{AA}^{eq} \approx$ 0.31V for the electrolyte concentrations used. The difference between these values ($\Delta E_{BC} \approx$ -0.59V) represents the minimum potential variation through the electrolyte that must be achieved to initiate this "uphill" bipolar chemistry. Specifically, the activation overpotentials for nickel and ascorbic acid charge transfer in Eqs. 4.4 and 4.5 are[76]

$$\eta_{s,Ni} = V_m - \phi(r) - E_{Ni}^{eq} \tag{4.6}$$

$$\eta_{s,AA} = V_m - \phi(r) - E_{AA}^{eq} \tag{4.7}$$

where the solution potential evaluated at the substrate surface $\phi(r)$ is shown explicitly as a function of the radial position. The open circuit mixed potential of the conductive substrate (V_m) reflects the kinetics and thermodynamics of the reactions when applied current (and hence $\phi(r)$) is equal to zero.

The array in Figure 4.3 shows how the SBC operating parameters couple to electrolyte chemistry to produce bipolar electrodeposition on a conducting substrate that is electrically floating. The 10 X 10 array features 10 different values of the applied current (I_{app}) along the horizontal axis and 10 different fly-heights (H) along the vertical axis. In this experiment, the deposition time was held constant at 5 seconds for each bipolar condition and electrolyte flowrate was constant at 400 μL min^{-1}. Deposit spacing is 300 μm center to center. No nickel deposition appears in the region of the array to the left of the dotted curve. Experimental conditions in the no-deposition zone do not generate enough potential drop in the electrolyte beneath the nozzle to overcome the thermodynamic barrier (-0.59V) for this bipolar pair. Under these conditions, all of the applied current passes through the electrolyte as an ionic current, and none undergoes charge transfer and passes through the substrate; the charge transfer resistance for the reactions is essentially infinite until the thermodynamic barrier is exceeded. As we move to conditions to the right of the dotted curve, the potential difference through the annular gap beneath the nozzle and substrate is sufficient to drive the bipolar reactions, and we observe nickel deposition on the gold substrate. Nickel deposits grow in size as the potential variation through the electrolyte is increased (either by increasing applied current or decreasing nozzle fly-height). If the potential variation exceeds a threshold represented by the dashed curve, undesirable hydrogen gas bubble formation disrupts nickel nucleation and deposition, reducing Faradaic efficiency. The experimental

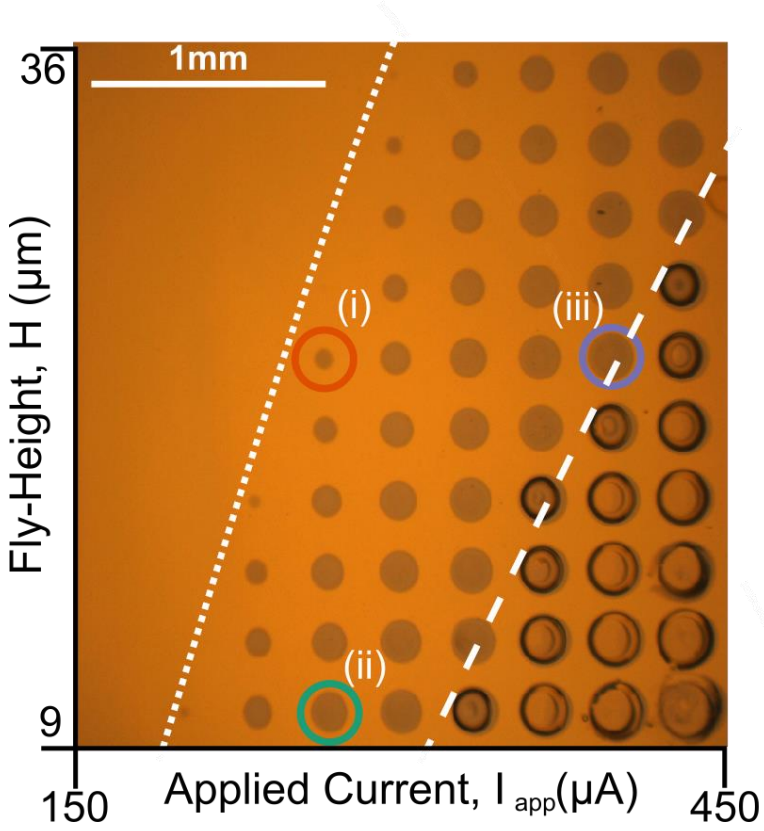

Figure 4.3. Nickel bipolar electrodeposition array

Optical micrograph of nickel deposits on a gold substrate deposited at a range of applied currents and nozzle fly-heights using ascorbic acid oxidation as the far-field bipolar oxidation chemistry.

conditions between the dotted and dashed curves in Figure 4.3 show that the SBC/Electrolyte combination has an ideal operating window for deposition.

The dotted curve in Figure 4.3 is an experimental estimation for the minimum polarization potential of the bipolar couple (ΔE_{BC}). Qualitatively, ΔE_{BC} is related to a minimum applied threshold current by

$$I_{min} \sim \frac{-\Delta E_{BC}}{R_{annular}} \ . \tag{4.8}$$

where $R_{annular}$ is the ohmic resistance through the annular gap and is estimated by the nozzle geometry and electrolyte conductivity (κ)[85]:

$$R_{annular} \sim \frac{ln\left(r_o/r_i\right)}{2\pi\kappa H} \ . \tag{4.9}$$

As fly-height is increased in Figure 4.3, the dotted curve estimating ΔE_{BC} moves to higher applied currents. This is expected, as an increase in fly-height decreases the annular resistance, and more applied current is needed to sufficiently polarize the substrate as described by Eq. 4.8.

When bipolar electrochemistry is active (i.e. solution potential variation exceeds ΔE_{BC}), the bipolar current flow is affected by the charge transfer resistances for nickel reduction beneath the microjet and ascorbic acid oxidation across the far-field substrate. Because of the small area of the nozzle region, the charge transfer resistance is dominated by nickel reduction beneath the nozzle, and can be approximated by[85]

$$R_{CT,red} \sim \frac{RT}{I_{app}\alpha_c zF} \ , \tag{4.10}$$

where we assume a Tafel kinetic approximation for the high overpotential reaction and α_c is the transfer coefficient for reduction, z is the number of electrons transferred, F is Faraday's constant, R is the ideal gas constant, and T is temperature (assumed to be room temperature). The relationship in Eq. 4.10 holds when the preponderance of applied current is through the bipolar chemistry route. In Figure 4.3, varying the applied current (horizontal axis) changes charge transfer resistance, by Eq. 4.10, and varying fly-height (vertical axis) changes the ohmic resistance, by Eq. 4.9. At condition (i) in Figure 4.3 there is little nickel deposition, which is expected as these conditions are immediately to the right of the dotted curve and the electrochemical system has only slightly exceeded ΔE_{BC}. For a given current, one sees that the amount of deposit increases when fly-height is decreased, due to increased potential variation through the annular gap, enabling more current to participate in bipolar electrochemical reactions. Profilometry scans show a height of 160 nm for deposit (ii) whereas the height of deposit (i) is approximately 10 nm. For a given fly-height, the nickel deposition is also significantly increased as applied currents increase. This is partially

caused by scaling of charge with applied current (47% more charge in deposit (iii) than (ii)) but the main affect is caused by the additional current beyond I_{min} participating in nickel reduction, with each increment of current lowering the charge transfer resistances. As a result, deposit (iii) in Figure 4.3 has a height of 355 nm. We expect the most efficient conditions for bipolar nickel deposition to occur when the ohmic potential variation is largest (lowest *H*) and charge transfer is lowest (highest I_{app}) for the range examined, and that is what we observe.

Quantitative analysis for the bipolar electrochemical behavior can be approximated through the bipolar current efficiency (*BCE*). *BCE* is the fraction of total applied current (I_{app}) that passes through the substrate and participates in electrochemical reactions on the substrate. We can estimate the *BCE* by comparing the actual mass deposited and relating that to the mass (*m*) calculated using Faraday's Law, assuming all the applied current goes into bipolar deposition. The amount of mass deposited is estimated from the bulk density of the deposited material (ρ) and volume (V_{prof}) determined using stylus profilometry (detailed in the supplementary materials). The experimentally estimated *BCE* is

$$BCE = \frac{\rho V_{prof}}{m} = \frac{\rho V_{prof} zF}{I_{app} \Delta t M} \tag{4.11}$$

where *M* is the molecular weight of nickel and Δt is the deposition time per dot. This method provides *BCE's* for deposits (i), (ii), and (iii) equal to 0.05%, 2.8%, and 7%, respectively, quantitatively matching the qualitative observations discussed above. For applications where having a high BCE is important, we describe the strategy for its optimization in a later section.

The guidelines developed for bipolar nickel reduction can be extended to other electrochemical reactions that behave similarly. For example, gold reduction from a cyanide complex, $Au(CN)^-_2$, is irreversible for the low complexant concentration used here. Screening arrays and Eq. 4.8 help identify the minimum threshold current I_{app} for this electrolyte, as well as

the conditions where deleterious secondary reactions occur. Figure 4.4a shows an optical micrograph of gold reduction patterned in the form of the elemental symbol Au using ascorbic acid as the reducing agent. This pattern consists of 260 individual gold deposits grown at I_{app} = 450 μA and H = 30 μm. Some gold discoloration is evident in the substrate background caused by small amounts of oxidation of the gold substrate.

The irreversible (easy to deposit, hard to strip) behavior of nickel and gold simplifies electrolyte design, as there is little concern for oxidizing the previously patterned material as the SBC moves across the gold substrate. However, electrolyte design with tight thermodynamic tolerances enables the growth and retention of deposits that are reversible (easy to deposit, easy to strip). Figure 4.4b shows an optical micrograph consisting of 281 copper deposits patterned on a gold substrate using ascorbic acid oxidation as the far-field chemistry. The applied current was 20 μA and fly-height was 30 μm. Copper is highly reversible in our electrolytes, so any copper patterns that move into the far-field can be oxidized, in competition with ascorbic acid oxidation. To avoid etching previously deposited copper material, the electrolyte is designed to be metastable, where there is a modest thermodynamic "downhill" driving force of about +10mV. The downhill thermodynamics of the electrolyte protects the copper deposits by making ascorbic acid oxidation preferential to copper oxidation, but the thermodynamic driving force is small enough to prevent spontaneous reduction of copper in solution.

Each local chemistry explored thus far utilized ascorbic acid as the far-field oxidation chemistry. Ascorbic acid is a convenient reducing agent for nickel, gold, and copper reduction in the SBC because it has good oxidation kinetics. However, ascorbic acid cannot be used for noble metals such as Ag^{+} reduction to $Ag_{(s)}$ because it is too strong of a reducing agent and will cause spontaneous reduction of silver ions in solution. Instead, we show that Fe^{2+} oxidation to form Fe^{3+}

in the far-field is an effective couple for bipolar silver reduction. Figure 4.4c shows an optical micrograph of 282 individual silver deposits patterned on a gold substrate. The dark coloration of the deposits results from depositing with a silver nitrate solution, which is known for producing coarse, grainy deposits[4]. This experiment had an applied current of 15 μA and fly-height of 30 μm. Similar to our copper system, a metastable electrolyte was formulated with a marginal downhill thermodynamic driving force estimated to be about +80mV. The reversibility of the far-field chemistry can also affect the efficiency of the bipolar system. To keep silver from reducing in solution, both Fe^{2+} and Fe^{3+} must be initially present to set the reducing power of the electrolyte at a level that maintains a metastable system. Therefore, Fe^{3+} reduction to Fe^{2+} competes with the desired silver deposition beneath the nozzle, reducing the Faradaic efficiency of the bipolar system.

Despite the range of materials patterned in Figure 4.3 and Figure 4.4 ---from noble to base metals, that are easy or hard to strip---we have demonstrated how to tailor the local and far-field chemistry to achieve stable, spatial control of the deposition and patterning on a macroscopic electrically floating substrate, demonstrating the idea of remote control electrodeposition.

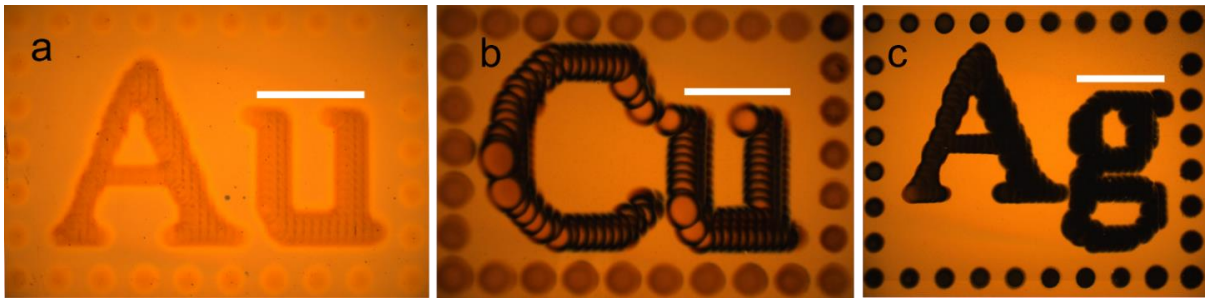

Figure 4.4. Au, Cu, & Ag patterns

Optical micrographs for patterned **(a)** gold deposition on a gold substrate with ascorbic acid oxidation in the far-field, **(b)** copper deposition on a gold substrate with ascorbic acid oxidation in the far-field, and **(c)** silver deposition on a gold substrate with Fe^{2+} oxidation to Fe^{3+} in the far-field. All scale bars are 1mm.

The metastable electrolyte design we use for reversible metals slightly "protects" the deposit with a thermodynamic bias toward reduction. Nonetheless, it is possible to "erase" a reversible metal when it enters the oxidizing far-field region, if the SBC is operated inappropriately. Figure 4.5 shows an optical micrograph of the same copper pattern and bath from Figure 4.4b, except deposition occurs at an order of magnitude higher applied current (200 μA). At the higher current, most of the copper symbol has been etched away as it moved into the oxidizing environment of the far-field (the SBC scanned from left to right, top to bottom in the image). The +10 mV of downhill driving force intrinsic to the bath protected the copper pattern in Figure 4.4b, when the tool operated at 20 μA and the far-field was only modestly oxidizing, but at 200 μA, the far-field polarization is more oxidizing and the copper gets erased in Figure 4.5 (the "Cu" outline shows where copper metal would have been visible, had there not been etching in the far-field). The amount of polarization and, hence, the operating I_{app}, where the SBC can operate without etching a reversible deposit depends on how the electrolyte is designed, i.e. how positive ΔE_{BC} is made. At the same time, the more thermodynamically downhill, the less stable the electrolyte will be, in general. An ideal electrolyte for patterning permanent deposits from reversible metals will have the largest ΔE_{BC} that does not spontaneously reduce the metal cation in solution. It is possible that electroless deposition reactions take place on the freshly deposited materials after initial nucleation overpotentials are overcome. This hypothesis can be tested with quartz crystal microbalance measurements, and will be a focus of future research in this area.

Simple scaling relationships can be used to understand nearly every aspect of the electrolyte/tool design characteristics. Because the SBC is governed by the behavior of a secondary

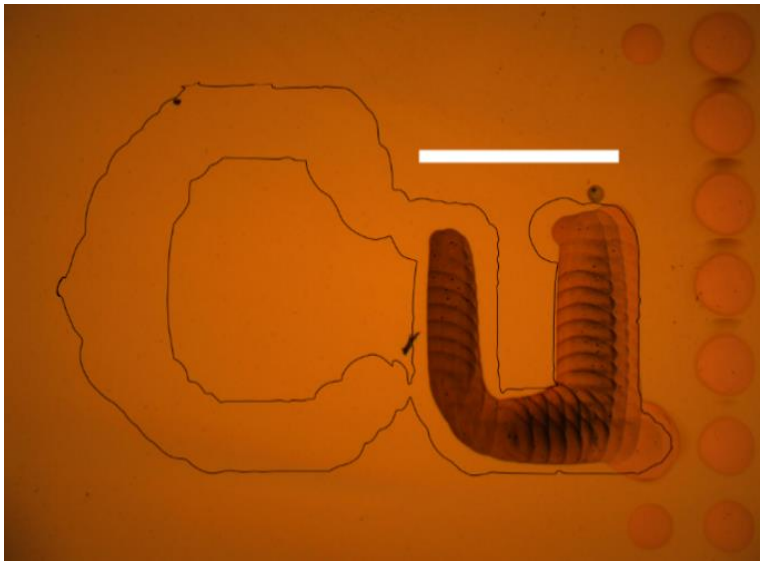

Figure 4.5. Cu pattern etches with high applied current

Optical micrograph of patterned copper that has been partially electrochemically oxidized when I_{app} is 200 μA. The Cu outline shows where copper material has been etched from the substrate. Scale bar is 1mm.

current distribution problem[28] (ohmic and charge transfer dominate, with negligible concentration gradients), scaling is described using the dimensionless Wagner number (Wa), which relates the key ohmic resistance to the key charge transfer resistance in the system. As described earlier, we can estimate the ohmic resistance of the SBC by Eq. 4.9 and the charge transfer resistance by Eq. 4.10, providing a Wagner number of the form

$$Wa = \frac{2\pi RT\kappa H}{I_{app}\alpha_c zF ln\left(r_o/r_i\right)}. \tag{4.12}$$

The possible strategies for optimizing the *BCE* can be understood by considering the parallel current paths beneath the nozzle, as we have discussed previously, in terms of the Wagner number. Using the parameters of this chapter, we can show that *BCE* scales as

$$BCE \sim \frac{1+\Delta E_{BC}\left(\frac{\alpha_c zF}{RT}\right)Wa}{1+Wa}. \tag{4.13}$$

Thus, *BCE* is optimized when the characteristic ohmic resistance is much higher than the charge transfer resistance (i.e. when *Wa* is small). This is achieved by lowering electrolyte conductivity (κ), lowering the fly-height (H), or increasing nozzle thickness (r_o/r_i); all of which increase the annular resistance through the electrolyte. Additionally, *Wa* is minimized at higher applied currents, where the Tafel charge transfer resistance is smaller. The *BCE* can be further understood by considering the thermodynamic factor in Eq. 4.13. For uphill thermodynamics (negative ΔE_{BC}), the *BCE* is lower the more uphill the system is for a given *Wa* number. When the numerator is negative, no bipolar electrodeposition occurs. In Figure 4.3, this is indicated by the region left of the dashed line, which scales with fly-height and applied current. Conversely, if the thermodynamics are downhill (positive ΔE_{BC}), then *BCE* can be greater than 1 due to the potential for spontaneous electroless deposition. We also note that the predicted resistance under the gap is higher than shown by Figure 4.3. This is likely due to imperfect microjet nozzles with rounded edges, implying that better fabrication would further increase *BCE*. The relationship in Eq. 4.13 effectively conveys the intricate coupling of kinetics, ohmic drop, and thermodynamics that influences bipolar behavior in the scanning bipolar cell. At the same time, we know that geometric scaling of the nozzle and far-field regions in the SBC is governed by the same set of physicochemical processes. It is important to show that geometric scale up or scale down is achievable, and we focus on that here.

Eq. 4.12 can be used to set equivalent geometric and operating parameters over a wide range of scales. Figure 4.6a shows an optical micrograph consisting of 261 individual nickel deposits patterned in the form of the Ni elemental symbol. Desirable operating conditions were selected from Figure 4.3, with I_{app} = 400 μA and H = 30 μm. Each deposit was grown for 2 seconds, with a 75 μm center to center spacing. In contrast, Figure 4.6b is a Ni pattern created with a 10-

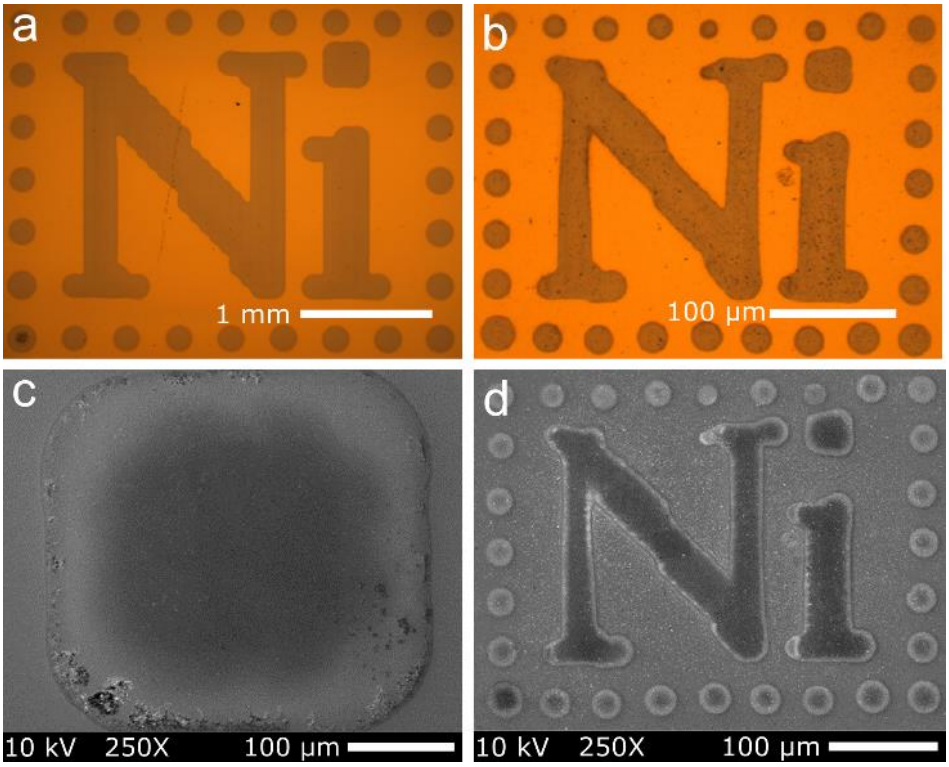

Figure 4.6. 10x nickel pattern scale down

Optical micrographs and SEM imaging for patterns using local nickel deposition and ascorbic acid oxidation in the far-field for **(a & c)** our standard nozzle dimensions of r_i = 100 µm and r_o = 300 µm and for **(b & d)** a 10x scale down of the nozzle inner radius with dimensions of r_i = 10 µm and r_o = 350 µm.

fold decrease in the nozzle inner radius (r_i = 10 µm and r_o = 350 µm), using the same electrolyte for local nickel reduction and far-field ascorbic acid oxidation as in Figure 4.6a. Operating conditions were set by creating the same value of *Wa* in Figure 4.6a and Figure 4.6b. To get equal *Wa*, with the new nozzle, the SBC settings were I_{app} = 40 µA and H = 9 µm. Flowrate and deposit spacing were also scaled to be 6.25 µL min^{-1} and 9 µm pitch, respectively, though these were set for convenience, not as a fundamental feature of scaling. The resulting scaled-down nickel deposition in Figure 4.6b is of similar quality to that shown in Figure 4.6a, though the positioning accuracy of each nickel dot is limited by the 3 µm resolution of our (worm-driven) motion-control

system. The overall size of the scaled-down pattern is 330 μm in width with individual deposits approximately 25 μm in diameter.

SEM images in Figure 4.6c-d show the patterns at the same magnification (Figure 4.6c is zoomed into the dot of the "i" in Figure 4.6a). These SEM images show fairly sharp edges at the borders of the patterns. The current density profile at the substrate is Gaussian-like in shape, with the low current tails being insufficient to exceed ΔE_{BC}, so deposition abruptly truncates at the edges. As a result, nickel deposition is restricted to the high current densities directly beneath the microjet nozzle. The relationship in Eq. 4.12 scales the bipolar current efficiency of the system, but not the characteristic current density, defined as I_{app}/A_{noz}, where A_{noz} is the cross-sectional area of the microjet. Therefore, we would not expect to see the same morphology for the 10x scale-down of inner nozzle radius and applied current shown in Figure 4.6, which produces a roughly 10x increase in current density. Indeed, significantly finer grains are observed for nickel deposition with the 10x nozzle scale-down (see SEM images in supplementary materials). These experiments demonstrate the scalability of bipolar electrodeposition. We expect it to have similar capabilities as conventional electrodeposition, which is suitable for sub-micron to nanometer scale patterning.

4.5 CONCLUSIONS

The scanning bipolar cell provides a unique method for bipolar electrochemical materials patterning on conductive substrates. Our previous demonstrations of the SBC used a copper substrate as the electron donor for local bipolar metal deposition. Here, we've designed the far-field oxidation chemistry into the electrolyte so that the conductive substrate is unchanged. SBC and electrolyte design was generalized by using a variety of noble and base metal deposition chemistries as indicators for bipolar behavior, where reversibility and nobility of the local

chemistry dictated electrolyte design. Potential variation generated beneath the microjet drives local electrochemistry, with spatial control provided by the operating conditions and motion control of the SBC. Temporal control is tailored by the dwell time for individual deposit growth and by the design of electrolytes that stabilize or destabilize the previously patterned deposits as they move away from the reducing zone beneath the microjet. Simple scaling relationships provide a pathway for scale-up or scale-down of the physicochemical phenomenon described here. More broadly, design guidelines developed here for metal deposition can be generalized to other types of bipolar electrochemical systems.

4.6 SUPPLEMENTARY INFORMATION

Electrodeposited profiles were measured using a Bruker OM-DektakXT profilometer and data was analyzed using Gwyddion (64 bit). 2D area scans were done for each deposit highlighted in Figure 4.3. Line scans in Figure 4.7a-c across the center of each deposit were selected to estimate the volume for each deposit. Volume was estimated by numerically integrating from the center of the profile to the edge of the deposit for both halves. Each half of the deposit was numerically integrated (assuming axial symmetry) using the trapezoidal rule

$$V_{half} = \pi \int_0^R rh(r)dr = \sum_{i=0}^{n} \pi (r_{i+1} - r_i) \left[\frac{h_{i+1}r_{i+1} + h_i r_i}{2}\right] \tag{4.13}$$

where r is the radius, $h(r)$ is the height profile as a function of radius, and the total profile volume (V_{prof}) is the sum of the two halves (V_{half}). Multiplying the volume by the bulk density of nickel (ρ) provides the estimate for total mass actually deposited. The mass calculated assuming all applied current participates in bipolar deposition is determined using Faraday's Law

$$m = \frac{I_{app}\Delta t M}{zF} \tag{4.14}$$

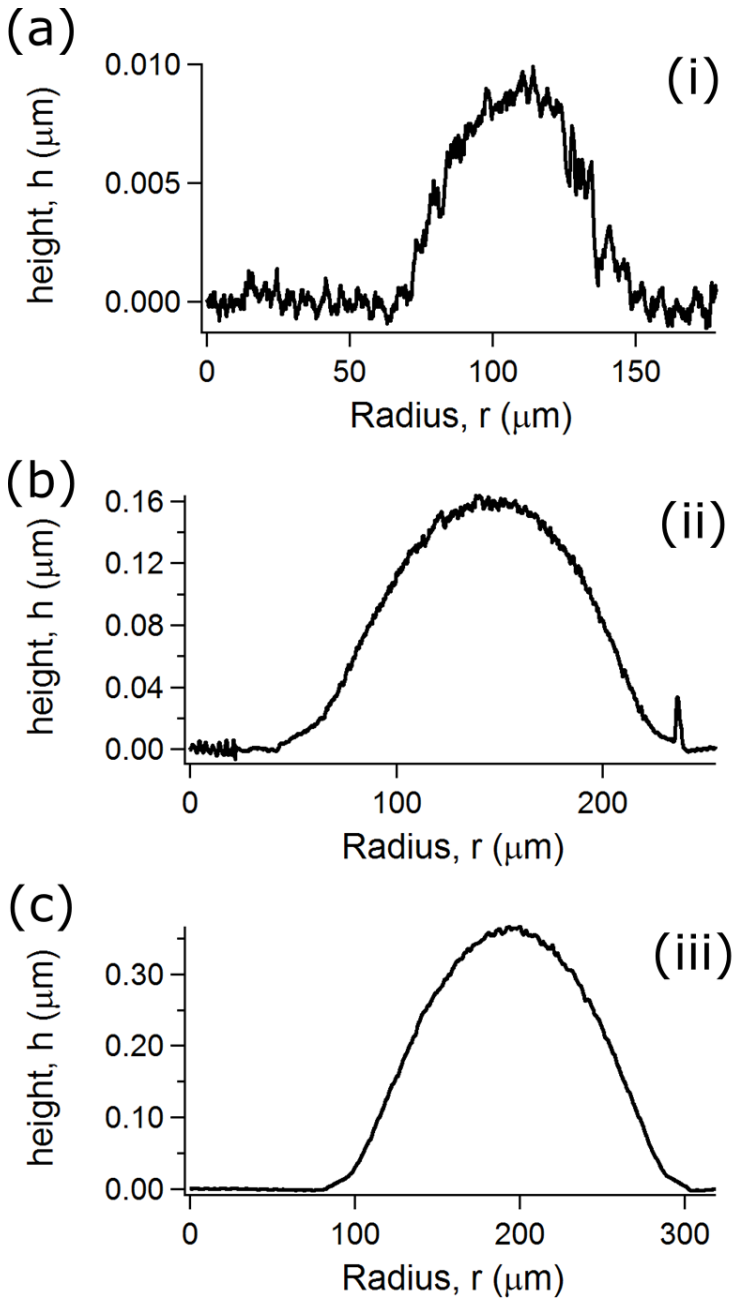

Figure 4.7. Nickel deposit height profiles

(a)Profilometry line scans for the deposits in Figure 4.2 with conditions of (a) I_{app} = 283.33 μA, H = 24 μm, (b) I_{app} = 283.33 μA, H = 9 μm, and (c) I_{app} = 416.67 μA, H = 24 μm.

where I_{app} is the applied current, Δt is the deposition time per dot, M is the molecular weight of nickel, z is the number of electrons transferred, and F is Faraday's constant. Dividing the estimated mass deposited by the expected mass calculated gives the bipolar current efficiency:

$$BCE = \frac{\rho V_{prof}}{m} = \frac{\rho V_{prof} zF}{I_{app} \Delta t M}. \quad (4.15)$$

This estimate assumes 100% Faradiac efficiency for nickel reduction. Using this approach, estimates for the *BCE* for deposits (i), (ii), and (iii) in Figure 4.3 are 0.04%, 2.77%, and 7.08%, respectively.

Nickel Deposition Scanning Electron Microscopy

Scanning electron microscopy was used to image and compare the nickel morphology for the 10x nozzle scale-down demonstrated in Figure 4.6. Figure 4.8a-b, show SEM imaging for the patterns in Figure 4.6a-b, respectively. Overall, the higher current density in Figure 4.8b produces much smaller grains than the lower current density conditions of Figure 4.8a, although less uniform. Larger nodule growth scattered across the surface is also seen in Figure 4.8b. This is fairly typical of our simple electrolytes where increased nodule growth can occur at high current densities. At higher current densities there is also more overpotential, and likely more hydrogen coevolution that can affect faradaic current efficiency. These are issues that can affect applications for scale-down into micron or submicron dimensions.

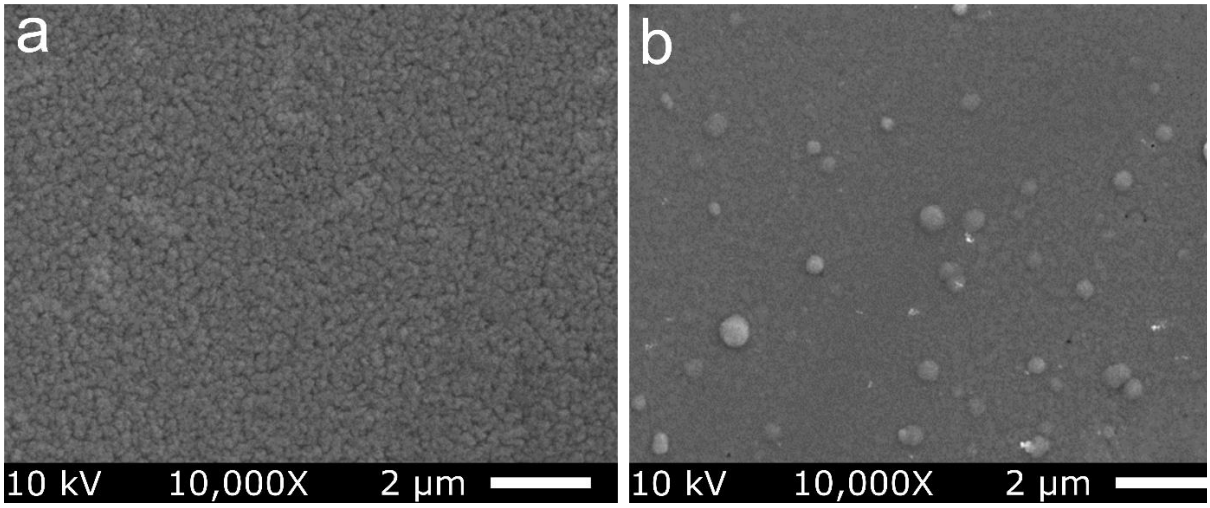

Figure 4.8. SEM morphology of nickel deposits

(a) SEM image of the nickel pattern from Figure 4.6a done with our standard nozzle with a 200 µm ID and 670 µm OD. (b) SEM image of the 10x scale down nickel pattern from Figure 4.6b done with nozzle dimensions of 20 µm ID and 700 µm OD.

Chapter 5. ELECTROANALYTICS OF BIPOLAR ELECTROLYTES

5.1 SUMMARY

In this chapter, electroanalytical methods are used to further understand design of bipolar electrolytes in the scanning bipolar cell. Koutecky-Levich rotating disk electrode analysis is used to determine the charge transfer kinetic parameters for ascorbic acid oxidation on a gold electrode. Ascorbic acid oxidation is used in nickel, gold, and copper electrodeposition and patterning in Chapter 4. These kinetic parameters are necessary for quantitative computational analysis explored in Chapter 6. Cyclic voltammetry of bipolar electrolytes elucidates information on secondary parasitic reactions and thermodynamic behavior for key bipolar electrolytes. The nickel and ascorbic acid electrolyte characteristic of irreversible local bipolar electrodeposition in fact shows that nickel is reversible, and is electrochemically etched from the surface We hypothesize that the irreversible nickel deposition observed in Chapter 4 is due to formation of a passivation layer at potentials similar to where ascorbic acid oxidation takes place. In addition, significant faradaic current losses are reported due to hydrogen reduction. Cyclic voltammetry of copper and ascorbic acid electrolytes show clear overlapping of copper and ascorbic acid oxidation peaks. This is expected because reversible local deposition reactions require metastable electrolyte formulations to protect previously deposited material from electrochemical oxidation.

5.2 Koutecky-Levich Analysis for Kinetic Parameters of Ascorbic Acid Electrochemical Oxidation

5.2.1 *Introduction*

Ascorbic acid (commonly known as Vitamin-C) is one of the more common organic compounds used in electrochemical systems due to its antioxidant behavior and function as a mild reducing agent[86]. Ascorbic acid's antioxidant behavior has generated substantial research interest in biological systems for its role in fighting diseases[87-89]. Recent electrochemical applications include the development of several forms of biosensors used to detect ascorbic acid quantities in foods and drugs[90,91]. Another heavily studied biological area where ascorbic acid plays a significant role is in the electrochemical detection of dopamine, which is complicated by ascorbic acid's similar oxidation potential and typically far higher concentrations[92,93]. Ascorbic acid has also proven useful in many non-biological applications[94]. For example, nano-networks of gold films for surface-enhanced Raman scattering have been developed through oxidation in the presence of ascorbic acid[95]. Additionally, ascorbic acid's role as a mild reducing agent was integral to the synthesis of palladium nanoparticles, where stronger reducing agents yielded palladium hydride particles[96].

The kinetics for oxidation of ascorbic acid,

$$AA \rightarrow DHAA + 2H^+ + 2e^- \tag{5.1}$$

are necessary to fully understand its role in electrochemical applications. Given its prevalence in bioanalytical and materials synthesis methods, it is not surprising that the homogeneous[97] and heterogeneous charge transfer kinetics of ascorbic acid have been reported[98-105]. Surprisingly, there seems to be a single prior study of charge transfer kinetics for ascorbic acid oxidation on gold, and

that was in a complex ammonium sulfate, acetic acid, phosphoric acid, and KOH containing electrolyte[106]. For our ongoing work related to bipolar electrochemistry, electrolytes require both reducible and oxidizable species, so it is necessary to simplify formulations to ensure functionality[44,45,107]. In the study presented here, rotating disk electrode Koutecky-Levich analysis was used to quantitatively determine exchange current density (i_o) and transfer coefficient (α) parameters characteristic of Butler-Volmer reaction kinetics for ascorbic acid oxidation on an electrodeposited gold surface.

5.2.2 *Experimental Methods*

The motivation for this study is to understand the role of ascorbic acid as a reducing agent in bipolar electrochemical applications, particularly for local electrodeposition using a scanning bipolar cell[107]. In these applications, the electrolytes typically consist of 0.1 M reducible metal sulfate salts and 0.01 M ascorbic acid. Therefore, the electrolytes used here for ascorbic acid kinetic analysis consisted of 0.01 M ascorbic acid and 0.1 M Na_2SO_4 [44]. The electrolyte had a pH of 3.3, which was below the first pK_a of the acid. The conductivity was 17 mS/cm. A 0.164 cm^2 PINE E7 Series platinum RRDE was electroplated with gold from an alkaline bath containing 6 g/L $KAu(CN)_2$ and 30 g/L KCN. Gold was electrodeposited galvanostatically at 2.5 mA for 60 seconds using a Pine Model AFRDE5 Bi-potentiostat. Prior to gold electrodeposition, the platinum RDE was cleaned via 20 cyclic voltammetry sweeps at a rate of 50 mV/s from -250 to 1550 mV vs SCE in a 1 M H_2SO_4 solution with the same bi-potentiostat. All experiments were carried out at room temperature, and all potentials reported are referenced to a saturated calomel electrode (SCE).

Prior to ascorbic acid kinetic measurements, the gold RDE was cleaned via 20 cyclic voltammetry sweeps at 50 mV/s from -200 mV to 1500 mV in a 1 M H_2SO_4 solution.. A Pine

Model AFMSRX analytical rotator provides controlled mass transfer rates at the RDE. Linear sweep voltammograms (LSVs) were obtained at rotation rates of 100, 225 400, 625, 900, 1225, and 1600 RPM. After collecting LSVs, a series of potentials was selected for potential step experiments to generate Koutecky-Levich plots. The selected potentials ranged from 80 mV to 160 mV in 10 mV intervals, providing a range of currents from 2% to 75% of the mass transfer limiting currents. Square wave potential step experiments were performed where potential was increased from 0 mV after 10 seconds to the desired potential for an additional 10 seconds. The current selected for Koutecky-Levich analysis was the average value over the final 5 seconds of the potential step experiments. The acquired data was modified to incorporate the solution ohmic drop between the rotating disk electrode and the reference electrode[108]. Rotation rates and potentials with less than 3 mV variation due to solution ohmic drop were selected for constant potential experiments.

5.2.3 *Analysis*

To estimate the kinetic parameters for the oxidation of ascorbic acid on gold, we use a Koutecky-Levich analysis, plotting the inverse of measured current versus rotation rate to the negative one half power ($\omega^{-1/2}$), with the data expected to fall on the line given by:

$$\frac{1}{i} = \frac{1}{i_K} + \left(\frac{1}{-0.62nFD_R^{2/3}\upsilon^{-1/6}C_R^*}\right)\left(\frac{1}{\omega^{1/2}}\right) , \tag{5.2}$$

where $n = 2$ is the number of electrons transferred, F is Faraday's constant, D_R is the diffusion coefficient of ascorbic acid (cm^2/s), v is the solution kinematic viscosity (cm/s), and C_R^* is the bulk concentration of ascorbic acid (mol/cm^3). The kinetic current density (i_K) is found from the intercept of the plot, and represents the pure mass-transfer-free current density at the selected potential. The diffusion coefficient for ascorbic acid (D_R) is determined from the slope of the line.

The kinetic current density can be written in a Tafel form

$$i_K = i_0 exp[\alpha n f(E - E^{eq})] \quad (5.3)$$

for high overpotentials, where i_o is the exchange current density, α is the transfer coefficient (for oxidation), $f = F/RT$ (with R being the universal gas constant and T = 298 K), and E^{eq} is the equilibrium electrode potential. Tafel plots are used to determine i_o and α from i_K values at different potentials.

5.2.4 *Results*

Figure 5.1 shows linear sweep voltammograms acquired at varying rotation rates. Mass transfer limiting currents for each rotation rate in Table 5.1 are estimated by taking the average of current between 200 and 300 mV. The amount of current produced by ascorbic acid oxidation that is kinetically limited is highest at potentials near the base of the exponential increase observed in Figure 5.1. Therefore, Koutecky-Levich kinetic analysis using Eq. 5.2 was done using currents evaluated at potentials between 82 mV and 122 mV at approximately 8 mV intervals. Koutecky-Levich plots with linear fits at these potentials are shown in Figure 5.2. The kinetic current (i_K) is estimated from the linear relationship in Eq. 5.2 by extrapolating the data to the ordinate intercept. The slope of the curves provides the diffusivity. Assuming n = 2 and a kinematic viscosity of 0.01 cm^2/s, the average from all the Koutecky-Levich plots diffusivity is 1.5×10^{-6} cm^2/s. This value is on the same order as other studies for ascorbic acid[100,106].

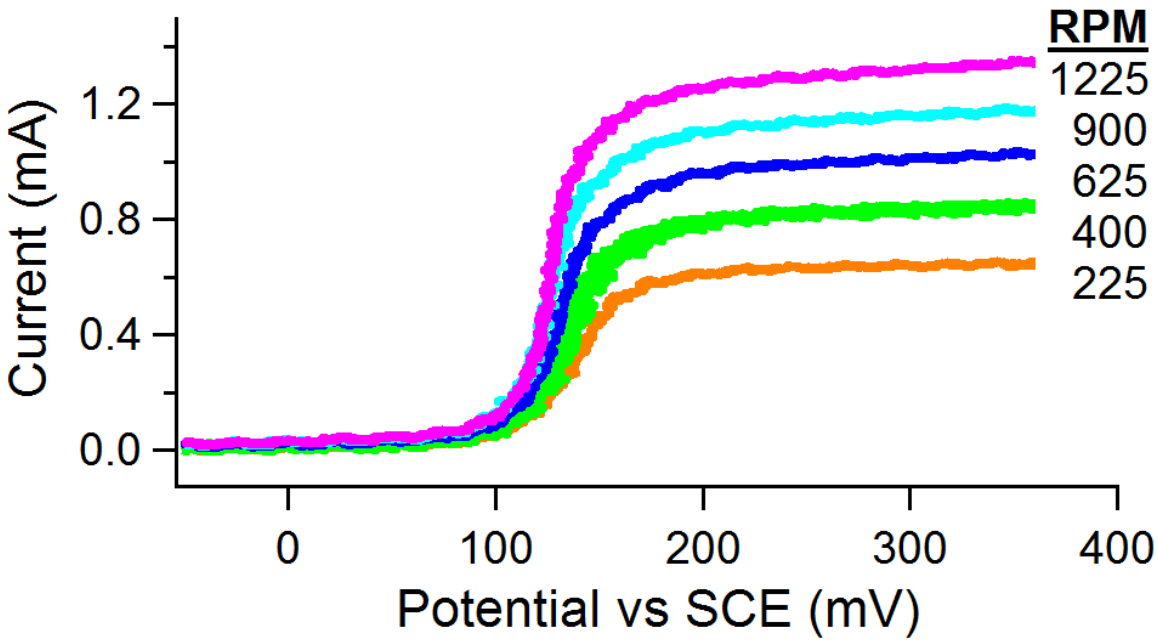

Figure 5.1. Ascorbic acid linear sweep voltammetry

Linear sweep voltammetry of 0.01 M ascorbic acid and 0.1 M Na_2SO_4 on a gold rotating disk electrode at the indicated rotation rates. The small limiting currents from dioxygen reduction were subtracted for each rotation rate.

Table 5.1. Mass transfer limiting currents for linear sweep voltammetry

Rotation Rate (RPM)	Mass Transfer Limiting Current (mA)
225	0.608
400	0.766
625	0.912
900	1.037
1225	1.154

To determine the kinetic parameters i_o and α, the natural log of kinetic currents (i_K) estimated from the graphs in Figure 5.2 was plotted versus overpotential ($E - E^{eq}$). This relationship shown in Figure 5.3 demonstrated linear behavior over the range of overpotentials selected. The transfer coefficient (α) is estimated from the slope of the linear fit and the exchange current density (i_o) is calculated from the exponential of the ordinate intercept. Using Eq. 5.3 and Figure 5.3, the transfer coefficient for oxidation is $\alpha = 0.20$ and the exchange current density is $i_o = 1.02$ mA cm^{-2}.

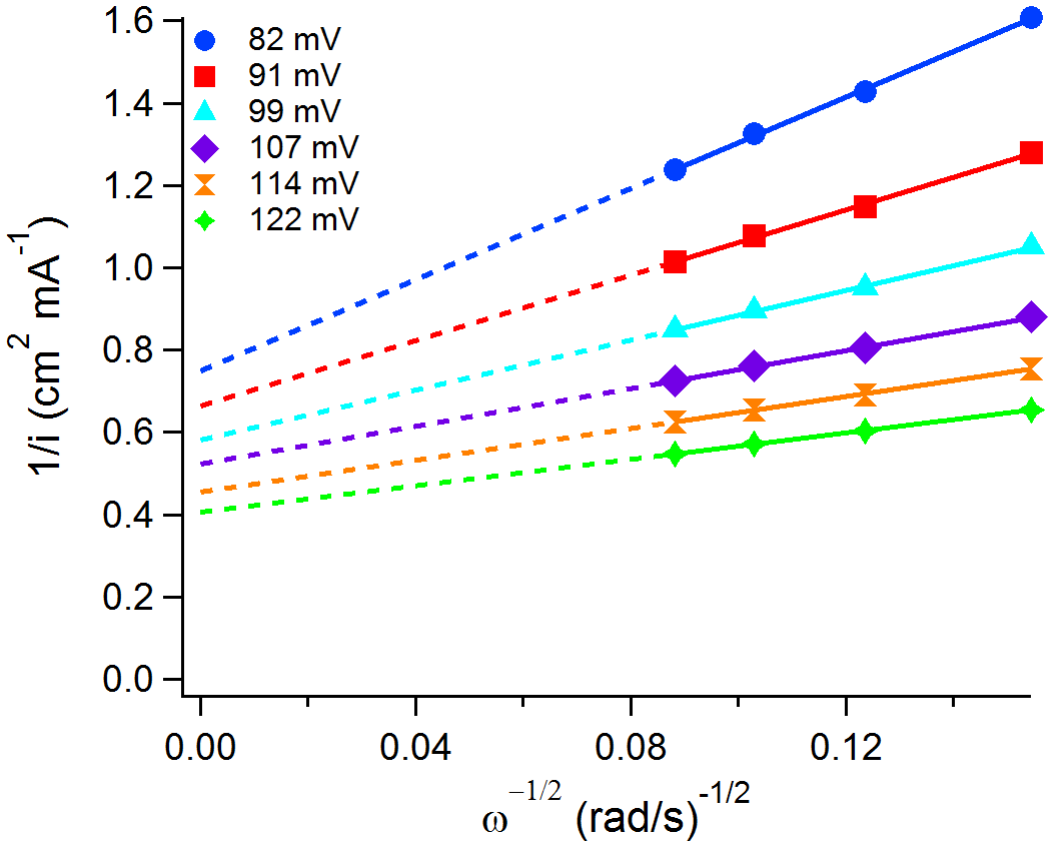

Figure 5.2. Koutecky-Levich plots

Koutecky-Levich plots of kinetic data for a 0.01 M ascorbic acid and 0.1 M Na_2SO_4 electrolyte on a gold rotating disk electrode.

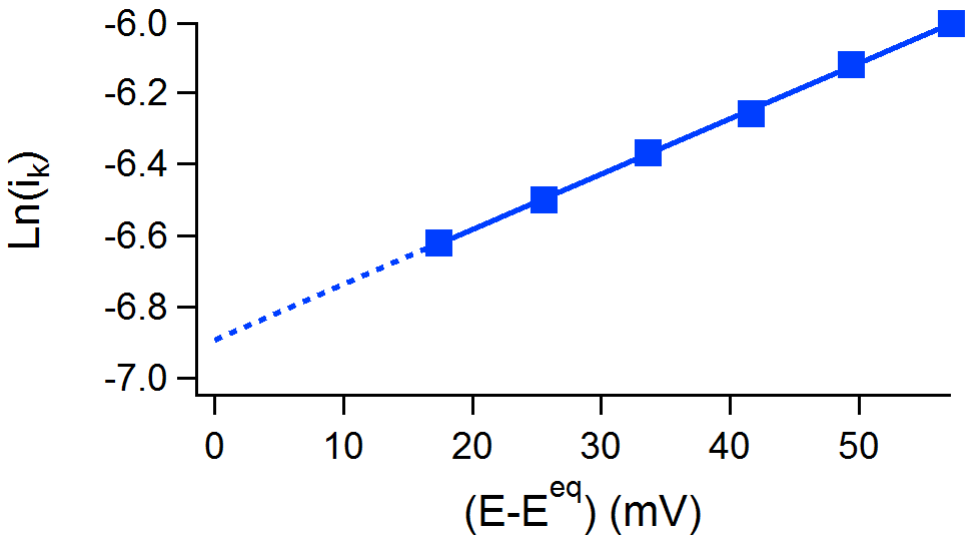

Figure 5.3. Linearized relationship for estimating kinetic parameters

Plot of the natural log of the kinetically limited current versus the overpotential. The linear relationship provides the transfer coefficient (α) from the slope and the exchange current density (i_o) from the ordinate intercept.

5.2.5 *Conclusion*

Koutecky-Levich analysis was used to estimate the Butler-Volmer kinetic parameters for ascorbic acid oxidation on an electrodeposited gold rotating disk electrode. Mass transfer limiting currents were measured at a range of rotation rates and the diffusivity for ascorbic acid in 0.1 M Na_2SO_4 was estimated to be 1.5×10^{-6} cm^2/s. Kinetically limiting currents estimated from Koutecky-Levich plots were used to determine the transfer coefficient ($\alpha = 0.20$) and the exchange current density ($i_o = 1.02$ mA cm^{-2}) used in Butler-Volmer kinetics. This kinetic information for ascorbic acid oxidation on a gold surface is valuable for designing electrochemical systems that use ascorbic acid's antioxidant properties. The experimental technique presented here provides a

straightforward pathway for estimating kinetic parameters of other heterogeneous electrochemical reactions.

5.3 Cyclic Voltammetry of Bipolar Electrolytes

5.3.1 *Introduction*

The coupling of thermodynamics, ohmic resistance, and charge transfer kinetics was addressed and generalized for several metal reduction chemistries in Chapter 4. Bipolar systems with irreversible local reduction chemistries (i.e. nickel and gold) can be designed with wide uphill thermodynamic windows as there is no concern for electrochemically oxidizing the deposited metals. However, these systems require more current to overcome the uphill thermodynamic window, sacrificing current efficiency for more facile electrolyte design. Bipolar systems with reversible local reduction chemistries (i.e. copper and silver) are easily etched off the substrate when moved into an anodically polarized region. To combat this, the bipolar electrolytes are engineered with a small downhill thermodynamic window. This design is akin to that of an electroless deposition system, except the spontaneous driving force for reduction is too small to overcome nucleation resistances. When bipolar electrolytes are designed in this manner, oxidation of the reducing agent is preferential to oxidation of the previously deposited metal. In Chapter 4, the Nernst Equation was used to estimate equilibrium potentials and subsequent thermodynamic windows for design of bipolar electrolytes. In this section, we use cyclic voltammetry to explore the effect of electrolyte composition on thermodynamic behavior for irreversible (nickel) and reversible (copper) bipolar electrolytes.

5.3.2 *Nickel Cyclic Voltammetry*

Cyclic voltammetry was done using a three-electrode system on a Pine Model AFRDE5 Bi-potentiostat with a platinum wire counter electrode. Prior to each experiment, gold substrates prepared by the University of Washington Nanofabrication Facility (WNF) were cleaned via 10 cylic voltammetry sweeps at 50 mV s^{-1} from -250 to 1500 mV vs SCE in a 1 M H_2SO_4 solution beginning at 0 mV. Gold substrates were then removed from solution, rinsed with deionized water, and dried with N_2 gas. All gold substrates were masked with a circular 0.385 cm^2 area (3.5 mm radius). All reported potentials are referenced against a saturated calomel electrode (SCE). Nickel bipolar electrolytes used in Chapter 4 are composed of 0.1 M nickel sulfate ($NiSO_4$) and 0.01 M ascorbic acid (AA). Ascorbic acid composition was varied at 0.001 M, 0.005 M, and 0.01 M while keeping nickel sulfate constant at 0.1 M. Nickel sulfate composition was also varied at 0.05 M, 0.1 M, and 0.2 M while keeping ascorbic acid concentration constant at 0.01 M. CV potential was sweeps were done at 50 mV s^{-1} from -900 to 1500 mV beginning at 0 mV for 5 cycles. The 5^{th} cycle was selected for comparison between electrolyte conditions.

Figure 5.4a shows the cyclic voltammograms for varying ascorbic acid concentrations and constant nickel concentration. An ascorbic acid oxidation peak (I) is observed around 250 to 300 mV for each composition with the onset for exponentially increasing current at about 70 mV. An increase in ascorbic acid concentration produces larger oxidation currents (0.5 mA, 1.5 mA, and 2 mA) before diffusional mass transfer limitations take place. The nickel reduction peak (II) appears combined with proton reduction between -600 and -900 mV. The Nernst equilibrium potential for hydrogen is estimated to be about 140 mV greater than nickel in our standard electrolyte formulation (pH ~ 2.9). Therefore, it is difficult to separate a clear nickel reduction peak from hydrogen reduction in this region. The onset potential for peak II is at approximately -525 mV for

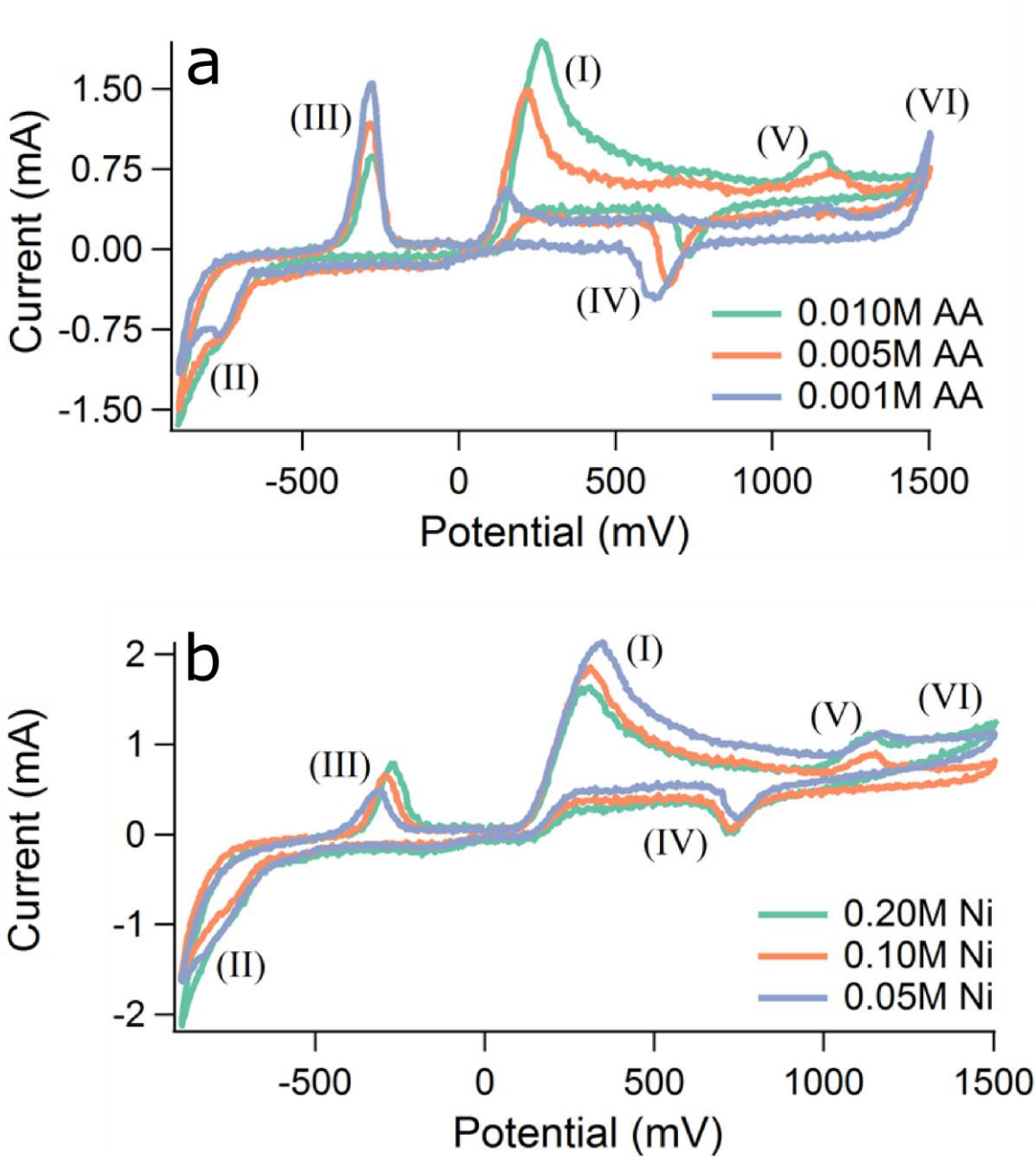

Figure 5.4. Cyclic voltammetry for nickel/ascorbic acid bipolar electrolytes

Cyclic voltammograms of the nickel/ascorbic acid electrolyte used in bipolar electrodeposition of nickel for **(a)** varying ascorbic acid concentrations with constant 0.1 M nickel sulfate and **(b)** varying nickel sulfate concentrations with constant 0.01 M ascorbic acid.

all three nickel compositions. The current appears to rapidly increase at -850 mV and is associated with hydrogen gas formation. Formation of H_2 at the working electrode provides new surface cites for increased proton reduction. In Figure 4.3 we observe crater-like nickel deposition at high applied currents, which we associated with hydrogen gas formation disrupting nickel nucleation. The difference between the onset potential for nickel reduction (-525 mV) and hydrogen gas formation (-850 mV) measured by cyclic voltammetry correlates well with the estimated potential window of 360 mV for bipolar nickel deposition in Figure 4.3.

A nickel oxidation peak III appears at about -275 mV with an onset potential of about -500 mV for each ascorbic acid concentration. Previous local electrodeposition of nickel with the SBC suggested that nickel reduction was irreversible. However, the CVs in Figure 5.4 show an oxidation peak with characteristics consistent with metal oxidation. In peak III current increases before sharply dropping to zero. This precipitous current decline is typical of complete metal etching, i.e. depletion of the reactant. Despite this, no nickel etching is observed in Chapter 4, despite the large 590 mV thermodynamic window between nickel and ascorbic acid equilibrium potentials. It is expected that nickel forms a passivation layer at a potential between nickel etching in peak III and ascorbic acid oxidation in peak I, protecting the metal from electrochemical oxidation with the SBC.

The amount of nickel oxidation current in peak III corresponds to the total amount of nickel reduction current in peak II and can be used to estimate faradaic current efficiencies for nickel deposition. Numerical integration of the current in peak III with respect to time gives the total charge for each concentration highlighted in Table 5.2. Using Faraday's law, the total mass etched (and deposited) is 0.52 μg, 0.70 μg, and 0.88 μg for 0.01 M, 0.005 M, and 0.001 M AA, respectively. Integrating current with respect to time for peak II from -500 mV to -500 mV

(through the -900 mV minimum) gives the total charge for reduction shown in Table 5.2. The higher total charges in peak II demonstrate that secondary reactions such as hydrogen reduction contribute significantly to the measured current. In fact, faradaic efficiencies for nickel reduction range from 24%-53%. The maximum current in peak III increases with decreasing ascorbic acid concentration. It is possible that ascorbic acid stabilizes nickel ions in solution, reducing the amount of deposition in peak II, and subsequently, nickel oxidation in peak III. The additional peaks indicated in the voltamograms are gold reduction (peak IV) at about 675 mV, gold oxidation (peak V) at 1200 mV, and water oxidation (peak VI).

Figure 5.4b shows cyclic voltammetry for constant ascorbic acid and varying nickel sulfate concentrations. The six peaks identified in Figure 5.4a are all present here. Oxidation of ascorbic acid peaks from 300 to 350 mV for each concentration with an onset potential of about 80 mV. The maximum current in peak I increases slightly with decreasing nickel sulfate concentration. This suggests that higher levels of nickel sulfate may hinder ascorbic acid oxidation, although the effect is not significant over the concentrations tested. Again, a reduction peak (II) between -600 mV and -900 mV consists of both nickel and hydrogen reduction reactions. The onset potential for peak II is between -550 and -650 mV for all three concentrations. The nickel oxidation peak III is observed between -300 mV and -250 mV for each condition, shifting to higher potentials at higher concentrations of $NiSO_4$ by about 25 mV. Higher peak currents are also achieved as concentration of nickel sulfate increases. Total charge contributing to nickel oxidation and combined nickel and hydrogen reduction is shown in Table 5.2. Using Faraday's law, the total mass etched estimated from these charges is 0.35 μg, 0.39 μg, and 0.49 μg for 0.05 M, 0.1 M, and 0.2 M $NiSO_4$, respectively. The total charge in the reduction peaks (II) is far higher than the oxidation peaks (III), with faradaic efficiencies for nickel reduction ranging from 13%-17%.

Table 5.2. Total charge for reduction (peak II) and oxidation (peak III) in Ni CVs

Sweep #	Nickel mass etched (μg)	Peak II Charge (mC)	Peak III Charge (mC)	Nickel Reduction Faradaic Efficiency
	0.1 M $NiSO_4$			
0.01 M AA	0.52	7.15	1.72	24%
0.005 M AA	0.70	7.17	2.31	32%
0.001 M AA	0.88	5.47	2.90	53%
	0.01 M AA			
0.05 M $NiSO_4$	0.35	9.01	1.14	13%
0.10 M $NiSO_4$	0.39	7.37	1.28	17%
0.20 M $NiSO_4$	0.49	9.76	1.59	16%

5.3.3 *Copper Cyclic Voltammetry*

The copper bipolar electrolytes are designed to be metastable, with a small downhill thermodynamic driving force for cupric ion reduction in solution. The Nernst Equation gives an estimate for this driving force, but does not provide any information on the electrolyte's stability over time. Comparison of a series of cyclic voltammetry sweeps gives some information on electrolyte stability over time. The experimental equipment and substrate preparation were the same as for the nickel CVs above. In this section, potential was swept from -200 mV to 1400 mV at 50 mV s^{-1}, beginning at 1000 mV. Cyclic voltammetry sweeps were initiated immediately after mixing ascorbic acid into copper sulfate solutions. Data was collected for 30 sweeps, covering a time frame of 32 minutes after electrolyte components were mixed. Copper bipolar electrolytes used in Chapter 4 were composed of 0.05 M copper sulfate ($CuSO_4$) and 0.005 M ascorbic acid. In this analysis, two electrolyte compositions were explored: 0.05 M $CuSO_4$ with 0.005 M AA and 0.05 M $CuSO_4$ with 0.01 M AA. The system with higher ascorbic acid has a larger thermodynamic driving force for cupric ion reduction, and therefore should demonstrate less stability over time.

Figure 5.5a and Figure 5.5b show cyclic voltammograms taken at sweeps 5, 15, and 30 for low concentrations (0.05 M) and high concentrations (0.1 M) of ascorbic acid, respectively. Reduction of copper ions to copper metal occurs in peak II with an onset potential of about -10 mV for both concentrations. The copper metal is then etched from the gold substrate in peak III with an onset potential of about 10 mV. Peak III shows the sharp decrease in current indicating that all copper has been etched from the surface. Numerical integration of the current with respect to time in peaks II and III for each concentration are highlighted in Table 5.3. The total charge for both reduction (II) and oxidation (III) show similar quantities for each sweep and both concentrations. Copper reduction occurs at a higher potential (about 500 mV) than nickel reduction, and therefore no current is lost to secondary hydrogen reduction in these electrolytes. The small difference between total charge for reduction and oxidation is attributed to ascorbic acid oxidation. These electrolytes are designed such that the copper and ascorbic acid equilibrium potentials are within a few tens of millivolts. Therefore, ascorbic acid oxidation is likely contributing to the current in peak III, producing additional charge not observed in the copper reduction peak. When all of the copper is removed from the substrate, an ascorbic acid oxidation peak (I) emerges at higher potentials. This peak is more distinguishable at higher ascorbic acid concentrations because higher current levels are achieved before diffusional mass transfer limitations occur. For both concentrations current decays slightly and the curves shift to lower potentials as time progresses. This shift is likely due to spontaneous, homogenous reduction of cupric ions in solution by the ascorbic acid. The shift in peak I is more noticeable than peak II because cupric ion concentration is much higher than ascorbic acid and thus consumption of ascorbic acid shows a greater effect. Small peaks for gold reduction (IV) and oxidation (V) are also indicated on the CVs in Figure 5.5a&b.

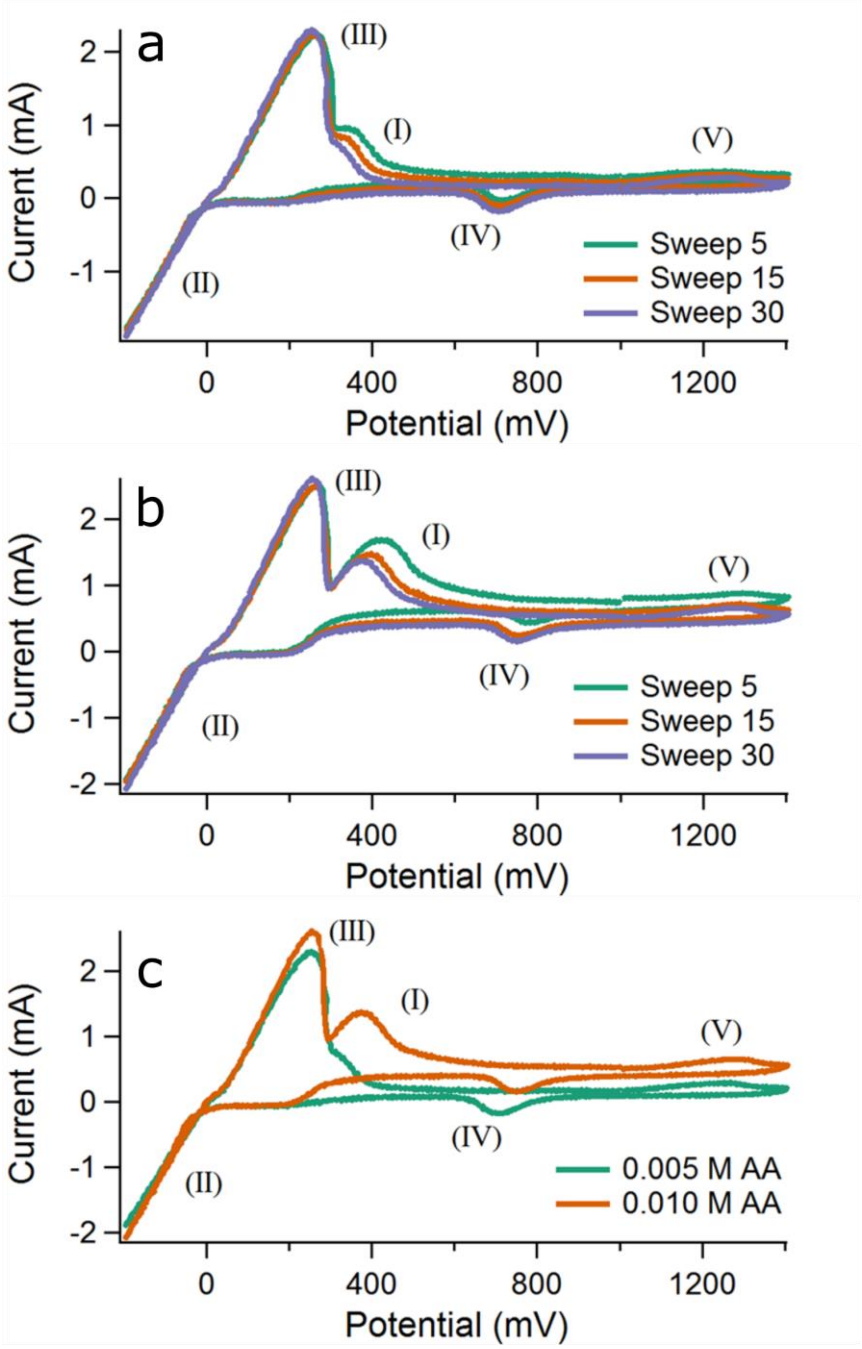

Figure 5.5. Cyclic voltammetry for copper/ascorbic acid bipolar electrolytes

Cyclic voltammograms at varying times for the copper/ascorbic acid electrolyte used in bipolar electrodeposition of copper for **(a)** 0.05 M $CuSO_4$ and 0.005 M ascorbic acid and **(b)** 0.05 M $CuSO_4$ and 0.01 M ascorbic acid. **(c)** Comparison of sweep 30 for each electrolyte composition.

Figure 5.5c shows cyclic voltammograms for each concentration at sweep 30. Significantly more ascorbic acid oxidation occurs in peak I at higher ascorbic acid concentrations. This is primarily due to additional ascorbic acid available for reaction but also caused by the equilibrium potential shift to a higher potential, making it easier to qualitatively separate copper and ascorbic acid oxidation currents. The total amount of copper deposited in peak II is essentially the same for both concentrations of ascorbic acid and the higher maximum current seen in peak III is due to increased ascorbic acid contributions at higher concentrations.

Table 5.3. Total charge for reduction (peak II) and oxidation (peak III) in Cu CVs

Sweep #	Copper mass deposited (μg)	Peak II Charge (mC)	Peak III Charge (mC)	Copper Oxidation Faradaic Efficiency
	0.005 M Ascorbic Acid			
5	2.30	-6.98	7.08	98.6%
15	2.34	-7.10	7.14	99.5%
30	2.42	-7.34	7.38	99.5%
	0.010 M Ascorbic Acid			
5	2.41	-7.33	7.78	94.2%
15	2.45	-7.45	7.71	96.6%
30	2.58	-7.82	8.10	96.6%

5.3.4 *Conclusion*

Cyclic voltammetry was performed for two types of bipolar electrolytes (irreversible and reversible local chemistries) to explore the electrochemical behavior of the bipolar systems and observe the effects of any secondary reactions. CVs show that nickel can be electrochemically etched from the gold substrate. The irreversible behavior in previous nickel experiments with the SBC is likely due to formation of a passivation layer at potentials more anodic than nickel oxidation peaks at -275 mV. In addition, significant hydrogen reduction takes place at similar potentials to nickel reduction, leading to faradaic efficiencies ranging from 13% to 53%. Varying

ascorbic acid concentration showed a more significant effect on current efficiency than varying nickel sulfate concentration, with the most efficient electrolyte formulation being 0.1 M $NiSO_4$ and 0.001 M ascorbic acid. A spike in current at -850 mV is attributed to hydrogen gas evolution. The potential window for H_2 gas evolution and the onset for nickel reduction (-525 mV) matches well the estimated 360 mV window for quality bipolar nickel electrodeposition in Figure 4.3.

For the reversible system, the copper electrodeposition and ascorbic acid oxidation bipolar couple was tested to explore stability of the metastable solution. Ascorbic acid oxidation current decreases with time, which is attributed to a small amount of spontaneous reduction of cupric ions in solution. This is expected, as the electrolytes are designed for ascorbic acid to be slightly reducing of copper ions. The peaks for ascorbic acid oxidation and copper overlap in these metastable solutions. Comparing copper oxidation current to the copper reduction current shows faradaic efficiencies of 94%-99%, with current inefficiencies generated by overlapping ascorbic acid oxidation. Cyclic voltammetry of nickel and copper bipolar electrolytes provides additional insight to the behavior of two types of characteristic bipolar systems used with the scanning bipolar cell.

Chapter 6. FUNDAMENTAL SCALING RELATIONSHIPS IN THE SCANNING BIPOLAR

6.1 SUMMARY

Bipolar electrochemistry in a scanning bipolar cell (SBC) enables local electrochemical reactions at an electrically floating conductive substrate. Bipolar electrochemistry involves complex coupling of the potential variation in solution, charge transfer kinetics for the bipolar couple, and thermodynamic relationship of the equal and opposite reduction and oxidation reactions. Finite element method simulations provide a powerful tool for understanding the intricate mating of the physicochemical phenomena in a bipolar electrochemical system. Yet it is often convenient to develop scaling relationships that simplify complex differential equations. In this work, finite element method simulations are used to relate bipolar electrochemical behavior in a SBC to a simple linearized equivalent circuit. Primary current distribution computations over several orders of magnitude show that the ohmic resistance through the SBC scales accurately with simple measures of microjet geometry and electrolyte conductivity. Secondary current distribution simulations that incorporate bipolar electrochemistry indicate that local charge transfer reactions beneath the microjet dominate the surface overpotential behavior so the charge transfer resistance is most representative of a Tafel kinetic regime. However, the coupling of ohmic resistance and charge transfer that is unique to bipolar electrochemistry leads to systematic errors in simple parallel circuit models where the two resistances are computed independently, underestimating the applied current necessary to overcome the thermodynamic barrier for “uphill” reduction and oxidation chemistries. Systematic deviations between simple parallel circuit elements and the

actual current distribution originates in the potential distribution beneath the microjet, where the manifestation of ohmic and charge transfer coupling is strongest.

6.2 INTRODUCTION

Figure 6.1a shows a perspective view schematic and key features for the experimental scanning bipolar cell. Electrolyte is pumped through an electrically insulating capillary nozzle. A platinum wire feeder electrode (typically the anode) is inserted in the microjet capillary upstream of the nozzle outlet where electrolyte jets onto the conductive substrate. The electrolyte pools on the substrate, forming a liquid meniscus, contacting a platinum feeder electrode ring (typically the cathode) attached to the acrylic housing of the microjet nozzle.

Figure 6.1b shows the axisymmetric geometry and key features of the scanning bipolar cell used in finite element simulations for the case where $H = R_i$. The inner (R_i = 100 μm) and outer (R_o = 335 μm) radii and the fly-height of the nozzle above the conductive substrate (H) control electrochemical behavior by tailoring the ohmic drop in the annular gap. The current flow pathways and operation of the scanning bipolar cell have been detailed in previous work[44,45,107]. Current sourced from the upstream platinum feeder electrode (I_{app}) has two pathway options: it can travel entirely through the electrolyte to the feeder cathode as ionic current (I_i), or, it can undergo charge transfer in the region beneath the nozzle, pass as electronic current (I_e) through the conductive substrate, and then undergo a second, equal and opposite, charge transfer reaction in the far-field area. The fraction of current that passes through the conductive substrate and participates in bipolar electrochemistry is coupled to the ohmic drop through solution, charge transfer kinetics, and thermodynamic relationship of the bipolar couple in the near-field and far-field of the substrate. For bipolar electrochemical current to flow through the substrate when the

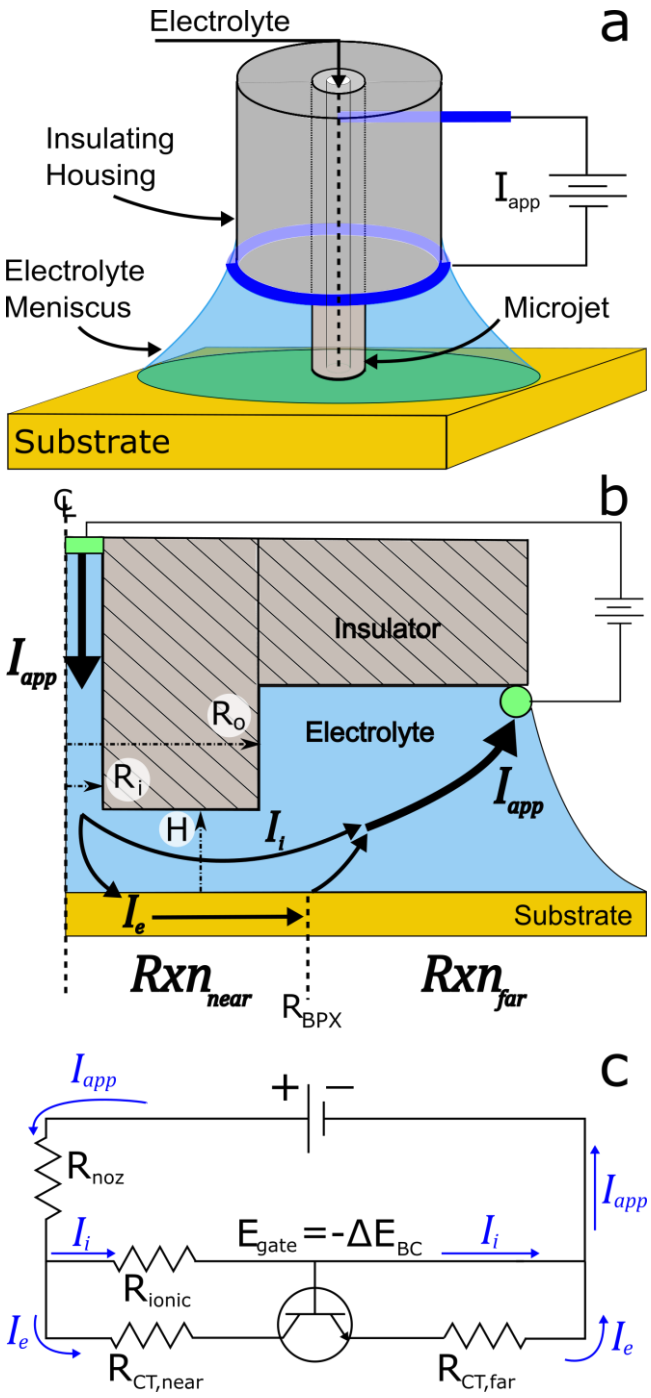

Figure 6.1. Schematics highlighting geometry and electrochemical features of the SBC **(a)** Perspective view schematic of important components in the SBC. **(b)** Schematic of axisymmetric geometric domain indicating current flow pathways. **(c)** Equivalent circuit approximating current flow and bipolar electrochemistry in the SBC.

near-field and far-field chemistry is thermodynamically uphill, the potential drop through solution must exceed the thermodynamic potential difference of the bipolar couple, ΔE_{BC}.

The current pathways described above can be approximated by the parallel equivalent circuit in Figure 6.1c. The resistance for current flow through the ionic pathway is dominated by the ohmic resistance beneath the microjet nozzle (R_{ionic}). The total resistance for current flow through the conductive substrate is the sum of the charge transfer resistances related to the bipolar electrochemical reaction kinetics ($R_{CT,near}$ and $R_{CT,far}$), assuming the electrical resistance of the conductor is negligible. However, current cannot flow through the electronic pathway until the substrate ohmic polarization exceeds the thermodynamic difference (ΔE_{BC}) between the equilibrium potentials of the bipolar reactions:

$$\Delta E_{BC} = E_{red}^{eq} - E_{ox}^{eq} \tag{6.1}$$

where the subscripts *red* and *ox* refer to the bipolar reduction and oxidation reactions occurring on the substrate, respectively. The thermodynamic difference in equilibrium potentials is in essence a threshold voltage; the circuit models that behavior by an ideal transistor with an infinite resistance until the gate voltage ($E_{gate} = -\Delta E_{BC}$) is exceeded. Once E_{gate} is exceeded, the transistor switches to zero resistance, and current flows through from the base-drain at a rate regulated by other circuit elements. The transition between "off" and "on" states is considered to be instantaneous. When the potential drop across the upper branch of the parallel circuit in Figure 6.1c is less than ΔE_{BC}, all of the applied current flows through the ionic pathway in the electrolyte. Once the potential drop through the annular gap ($E_{gate} = I_{app}R_{ionic}$) is greater than ΔE_{BC}, the transistor allows current flow through the lower branch of the parallel circuit via charge transfer reactions at the conductive substrate in the form of bipolar reactions. The fraction of total applied current that passes through the conductive substrate is the bipolar current efficiency (*BCE*):

$$BCE = \frac{I_e}{I_{app}}. \tag{6.2}$$

The *BCE* is a key quantitative descriptor for the coupling of ohmic, charge transfer, and thermodynamic contributions indicated in Figure 6.1c.

To understand the *BCE* and relate circuit elements in Figure 6.1c to physical parameters we introduce two experimental distinct systems. In previous work with the SBC, we have focused on near-field metal electrodeposition with an oxidation bipolar counter reaction in the far-field area. Electrodeposition chemistries provide an experimentally observable representation of bipolar behavior in the SBC. The types of chemistries selected will clearly influence the kinetics at the substrate, but equally significant is the thermodynamic relationship of the bipolar couple. Bipolar couples that are a reversible redox pair will have the same equilibrium potential and no net overall reaction, for example:

Scheme 1:

$$Near: \quad Cu^{+2} + 2e^- \rightarrow Cu_{(s)} \quad , \quad E^{eq}_{near} = 0.31V$$

$$Far: \quad Cu_{(s)} \rightarrow Cu^{+2} + 2e^- \quad , \quad E^{eq}_{far} = 0.31V$$

$$Net: \quad No\ Net\ Bipolar\ Reaction \quad , \quad \Delta E_{BC} = 0\ V$$

The reaction system in Scheme 1 has a thermodynamic potential difference (ΔE_{BC}) equal to zero by Eq. 6.1. For this bipolar couple, the gate voltage (E_{gate}) in the equivalent circuit in Figure 6.1c is zero, and any amount of applied current will drive bipolar reactions at the substrate.

When the desired near field chemistry is different from the far-field chemistry, there will be a thermodynamic difference. In the case of near-field nickel deposition on a gold substrate with far-field ascorbic acid oxidation, the equilibrium potentials of the bipolar reactions are:

Scheme 2:

$$Near: \quad Ni^{+2} + 2e^{-} \rightarrow Ni_{(s)} \quad , \qquad E_{red}^{eq} = -0.28V$$

$$Far: \quad AA \rightarrow DHAA + 2H^{+} + 2e^{-} \quad , \qquad E_{ox}^{eq} = 0.31V$$

$$Net: \quad Ni^{+2} + AA \rightarrow Ni_{(s)} + DHAA + 2H^{+} \quad , \quad \Delta E_{BC} = -0.59\,V$$

The reaction system in Scheme 2 has an overall net chemistry and a thermodynamic potential difference (ΔE_{BC}) of -0.59V. For the convention used here, negative values for ΔE_{BC} indicate an uphill thermodynamic barrier. Thus, this bipolar reaction system has a gate voltage of 0.59V that must be exceeded before any current can pass through the electronic pathway. In the following sections, we use finite element simulations and physical arguments to identify appropriate scaling relationships for each circuit element, as a means to predict BCE without need for full simulations

6.3 Simulation Methods

6.3.1 *Primary Current*

Finite element method simulations were used to explore the primary current distribution in the electrolyte using the SBC geometry ($H = R_i$) shown in Figure 6.2. The potential distribution through the electrolyte domain is modeled by Laplace's equation:

$$\nabla^2 \phi = 0 \, . \tag{6.3}$$

The nozzle and housing walls are treated as insulating boundary conditions, as is the substrate, in order to directly compute ohmic resistance through the nozzle gap:

$$\mathbf{n} \cdot \nabla \phi = 0 \, . \tag{6.4}$$

The anode boundary condition at the microjet inlet is

$$-\kappa \mathbf{n} \cdot \nabla \phi = \frac{I_{app}}{A_{nozzle}} \tag{6.5}$$

where κ is the electrolyte conductivity (1 S/m in primary current computations), $\boldsymbol{n}$ is the unit normal vector pointing out of the computation domain, A_{nozzle} is the area of the nozzle where current is applied, and I_{app} is the total applied current to the system. The cathode boundary is at the edge of the annular gap (R_o) and is set to a constant potential of zero:

$$\phi|_{R_o} = 0. \tag{6.6}$$

Simulations were performed at a constant applied current (100 μA) over a wide range of fly-heights (H = 2 μm to 1000 μm) and inner and outer radii (r_i = 50, 100, or 200 μm and r_o = 335, 670, or 1005 μm).

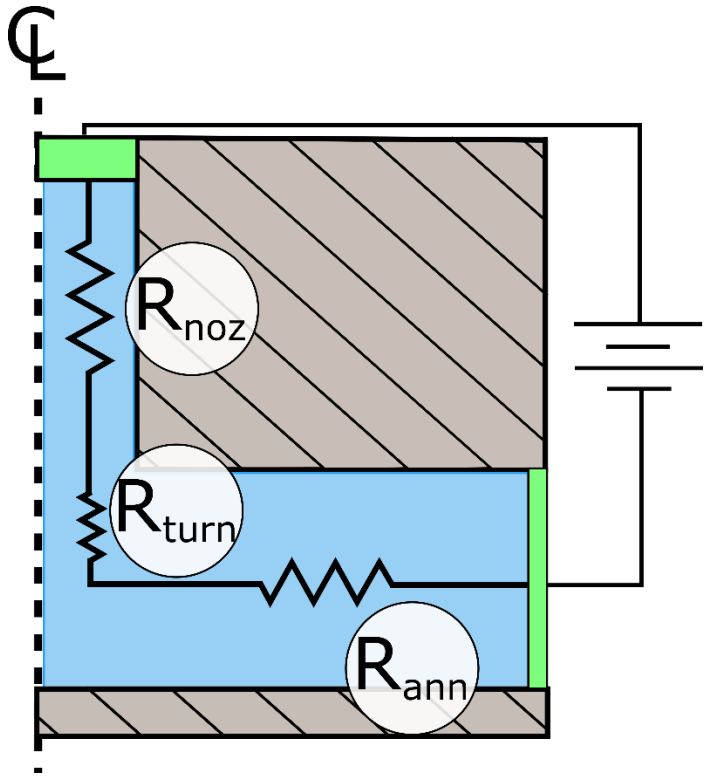

Figure 6.2. Primary current distribution geometry

Axisymmetric schematic of primary current distributions indicating the key ionic ohmic resistances between the feeder anode and the edge of the annular gap (R_o)

Mesh refinement in the regions of high gradient was used so that the overall charge balance in the system was less than 0.01% error. Grid refinement increased when geometric features decreased, producing about 100,000 to 3,000,000 mesh elements and a computational time of approximately 10-30 seconds for a typical converged solution. All computations were performed on a Lenovo ThinkCenter model m7052-C9U with an Intel Core i7-2600 CPU @ 3.40 GHz and 8 GB Ram using a Windows 7 Professional 64-bit operating system. Finite-element method (FEM) simulations were performed using COMSOL version 4.4 software with the heat transfer in fluids module.

6.3.2 *Secondary Current*

A secondary current distribution is appropriate here because concentration is substantially uniform in this high mass transfer rate microjet configuration[27]. Secondary current distribution computations were performed in the 2D axisymmetric computational domain in Figure 6.1b. All secondary current computations use a microjet nozzle with dimensions of R_i = 100 μm and R_o = 335 μm. The potential distribution in the electrolyte is defined by Laplace's equation (Eq. 6.3) and the nozzle, housing walls, and electrolyte meniscus are treated as electrically insulating boundary conditions (Eq. 6.4). The boundary condition for the feeder anode is defined by Eq. 6.5 and the feeder cathode boundary condition is

$$-\kappa \mathbf{n} \cdot \nabla \phi = \frac{-I_{app}}{A_{cathode}} \tag{6.7}$$

where $A_{cathode}$ is the area of the outer ring cathode. The most general form for the reaction rates at the conductive substrate are given by a modified Butler-Volmer kinetics

$$i_j = i_{o,j}\left[f_j e^{\left(\frac{\alpha_{a,j} n_j F}{RT}\eta_{s,j}\right)} - g_j e^{\left(\frac{-(1-\alpha_{a,j}) n_j F}{RT}\eta_{s,j}\right)}\right] \tag{6.8}$$

where $i_{o,j}$ is the exchange current density for reaction j, n_j is the number of electrons transferred for reaction j, and $\alpha_{a,j}$ and $\alpha_{c,j}$ are the transfer coefficients for the anodic and cathodic branches of reactions j, respectively. T is the temperature of the system (298 K), F is Faraday's constant, and R is the ideal gas constant. The functions f_j and g_j modify the Butler-Volmer equation to account for the reversibility of the respective branches. For example, the general Butler-Volmer equation with reversible kinetics such as Scheme 1 has functions f_j and g_j both equal to 1, whereas a Tafel approximation for reduction, as we assume in Scheme 2 near-field, has $f_j = 0$ and $g_j = 1$. For a bipolar system the anodic and cathodic reaction branches are not necessarily the same, and the total current at the substrate is the sum of the individual partial currents:

$$i = \sum i_j \tag{6.9}$$

The surface overpotential in Eq. 6.8 is

$$\eta_{s,j} = V_m - \phi(r) - E_j^{eq} \tag{6.10}$$

where the solution potential evaluated at the conductive substrate surface is a function of radial position as denoted by the function $\phi(r)$. The equilibrium potentials (E_j^{eq}) are estimated by a Nernst approximation and the open-circuit mixed potential of the conductive substrate (V_m) reflects the thermodynamics and kinetics of the reactions when current and ϕ are equal to zero.

To remain charge neutral, the conductive substrate must have equal and opposite oxidation and reduction reactions, which is expressed by the integral constraint over the area of the substrate:

$$I_{e,net} = 2\pi \int_0^R irdr = I_{e,near} + I_{e,far} = 0 \tag{6.11}$$

where i is defined by Eq. 6.9 and $I_{e,net}$ is the net electronic current passing through the conductive substrate, which must be zero when integrated over the whole substrate. The quantities $I_{e,near}$ and $I_{e,far}$ are the contributions from the equal and opposite reduction and oxidation reactions occurring on the substrate. The location along the radial axis where the current density is equal to zero is

defined as the bipolar cross-over point (*BPX*). Integrating the current density on the substrate from the nozzle center to the *BPX* yields $I_{e,near}$ in Eq. 6.11. Similarly, integrating current density from the *BPX* to the edge of the substrate radius (*R*) gives the equal and opposite value for $I_{e,far}$. In the simulations presented here, the *BCE* in Eq. 6.1 is computed with $I_{e,near}$.

The boundary condition for secondary current simulations of Scheme 1 is the Butler-Volmer approximation in Eq. 6.8 with kinetic parameters: i_o = 33.5 A m^{-2}, α_a = 0.73, α_c = 0.27, and n = 2. . Here, we use the reversible form of the Butler-Volmer equation where f_j and g_j are equal to 1. Electrolyte conductivity for these simulations is 1.125 S/m. If we assume the reversible copper chemistry is measured with a reference electrode of the same kind (i.e., a reversible copper reference) then $E_{red}^{eq} = E_{ox}^{eq} = 0$ and V_m = 0. This simplifies the expression for overpotential (η_s), which is now only a function of potential at the surface $\phi(r)$.

Computations for near-field nickel reduction on a gold substrate with ascorbic acid as the far-field bipolar counter reaction in Scheme 2 was used to explore electrochemical behavior for a thermodynamically uphill bipolar couple. For these computations nickel reduction is taken as irreversible, so we use the cathodic Tafel branch (setting f_j = 0 and g_j = 1 in Eq. 6.8) with kinetic data taken from literature[78]. For ascorbic acid, trace amounts of dehydroascorbic acid are present in the solution due to oxidation at the feeder cathode, and therefore the open circuit potential of the substrate is dominated by the ascorbic acid redox chemistry. We deal with the uncontrolled, trace dehydroascorbic acid in a manner that is easy to implement, produces results that are consistent with experimental measurables (such as open circuit potential, threshold voltages/currents, etc.) and whose magnitude (within reasonable bounds) has negligible influence on the computational results we report. Specifically, we use the Butler-Volmer form with f_j = 1 for the oxidation branch and set a small limiting current for dehydroascorbic acid reduction ($0.01i_{o,AA}$)

with g_j = *(1-i/0.01$i_{o,AA}$)*. This *ad hoc* treatment of the small amounts of dehydroascorbic acid reduction possible in the system gives the boundary condition for total current density on the bipolar substrate as

$$-\kappa \boldsymbol{n} \cdot \nabla \phi = i = i_{o,AA} e^{(\alpha_{AA} f \eta_{s,AA})} - i_{o,AA}\left[1 - \frac{i}{0.01(i_{o,AA})}\right] e^{(-(1-\alpha_{AA}) f \eta_{s,AA})} - i_{o,Ni} e^{(-(1-\alpha_{Ni}) f \eta_{s,Ni})} \quad (6.12)$$

where the room temperature kinetics for nickel and ascorbic acid are assumed to be $i_{o,Ni}$ = 2x10^{-6} mA cm^{-2}, $i_{o,AA}$ = 1.02 mA cm^{-2}, α_{Ni} = 0.5, α_{AA} = 0.20, and f = 77.89 V^{-1} since both reactions transfer two electrons[78].

For secondary current simulations, mesh refinement in the regions of high gradient was again used so that the overall charge balance and the substrate integral on the bipolar electrode both converged to less than 0.01% error. This resulted in about 200,000 to 2,000,000 mesh elements and computation times ranging from 5-10 minutes for a typical converged solution. Equipment and software used was the same as for primary current computations.

6.4 Results and Discussion

6.4.1 *Primary Current Scaling*

The computed resistance ($R_{computed}$) was estimated by taking the average potential at the anode, dividing by I_{app}, and subtracting the contribution of the microjet nozzle, which has an ohmic resistance of:

$$R_{noz} = \frac{l}{\pi \kappa R_i^2}\,. \quad (6.13)$$

The ohmic drop through the microjet nozzle does not affect the parallel splitting of current, but is important when considering the total potential sourced by the power supply. In these simulations l = 2 mm.

The characteristic resistance for current flow in the ionic pathway is the ohmic drop from the microjet outlet through the annular gap (R_{ionic}). In previous work, R_{ionic} was approximated by the resistance to current flow through an annular gap (R_{ann}), which is estimated by the electrolyte conductivity (κ) and nozzle geometry[85]:

$$R_{ann} = \frac{Ln\left({}^{R_o}/_{R_i}\right)}{2\pi\kappa H}. \tag{6.14}$$

Figure 6.3a shows a log-log plot of the computed resistances (R_{comp}) at varying nozzle geometries and fly-heights versus the annular resistance calculated by Eq. 6.14 (indicated by the black line). At low fly-heights, the computed resistances correlate well with Eq. 6.14. As fly-height is increased, the computed resistances diverge significantly from R_{ann} and plateau at fixed values. The expression in Eq. 6.14 is for current flow between two concentric cylindrical electrodes indicated qualitatively by the resistance R_{ann} in Figure 6.2. This approximation does not fully capture the characteristic ohmic resistance in the SBC, as there is an additional resistance between the microjet exit and the inner radius of the nozzle (R_{turn}). Current flow through the microjet outlet in the SBC is similar to that of a cylindrical disk. The potential variation near a disk electrode has been detailed previously[108], where we find a good fit to our geometry using the expression:

$$R_{turn} = \frac{1}{4\kappa R_i}\left(1 - \frac{2}{\pi\sqrt{1+0.16\left(\frac{H}{R_i}\right)^2}}\right). \tag{6.15}$$

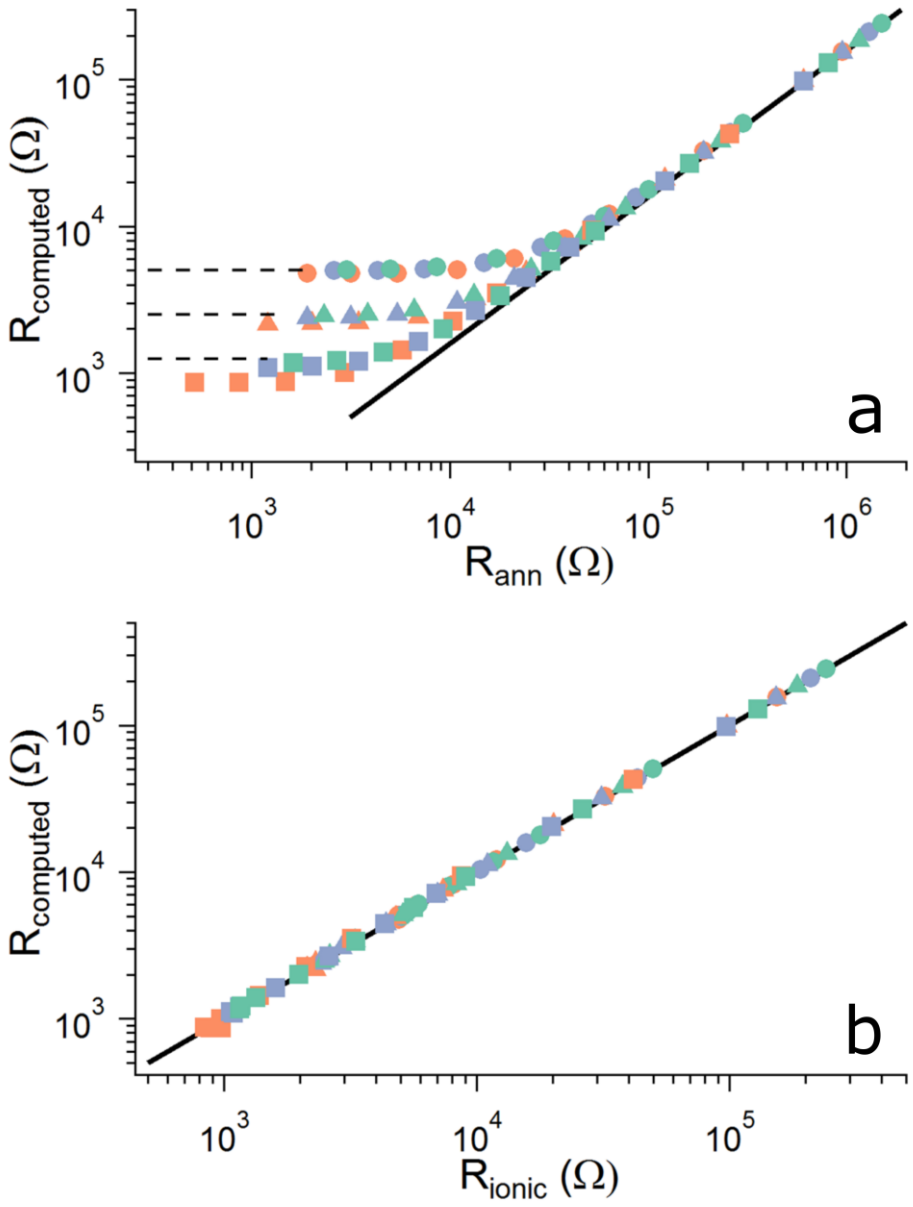

Figure 6.3. Comparison of computed ohmic resistances to scaling relationships

Computed ohmic resistances from the microjet exit to the edge of the annular gap are plotted (log-log) for varying microjet geometries versus scaling relationships: (a) versus the annular resistance (Eq. 6.8) with dashed lines indicating values for R_∞ and (b) the full scaling relationship that incorporates the resistance of an infinite disk (Eq. 6.16). Computed geometries are (in μm): R_i = 50 R_o = 335 (●), R_i = 100 R_o = 335 (▲), R_i = 200 R_o = 335 (■), R_i = 50 R_o = 670 (●), R_i = 100 R_o = 670 (▲), R_i = 200 R_o = 670 (■), R_i = 50 R_o = 1005 (●), R_i = 100 R_o = 1005 (▲), R_i = 200 R_o = 1005 (■).

When H is sufficiently large, the characteristic ohmic resistance directly beneath the microjet converges to the case when the counter electrode is at an infinite distance[108]. The dashed lines in Figure 6.3a indicate that Eq. 6.15 has the correct limiting behavior as $H \rightarrow \infty$ for different values of R_i. The total resistance for current flow in the ionic pathway is approximated by the sum of the resistances directly beneath the microjet (R_{turn}) and through the annular gap (R_{ann}):

$$R_{ionic} = \frac{1}{4\kappa R_i}\left(1 - \frac{2}{\pi\sqrt{1+0.16\left(\frac{H}{R_i}\right)^2}}\right) + \frac{Ln\left({R_o}/{R_i}\right)}{2\pi\kappa H}. \tag{6.16}$$

Figure 6.3b shows computed ohmic resistances plotted versus the scaling relationship in Eq. 6.16. The additional approximation for R_{turn} causes the data to fall completely on the diagonal line over ohmic resistance variations of several orders of magnitude. This good universal fitting is evidence that the computational solutions over the entire range of geometries are reasonable Thus, the geometric contributions to the ohmic resistance in the SBC are accurately modeled by the scaling relationship in Eq. 6.16 in a primary current system.

The universal nature of Eq. 6.16 is the ideal situation for a scaling relationship; a set of known geometric and physicochemical parameters (here electrolyte conductivity) are grouped into a simple analytical expression that captures all of the key features of more complex computations. Of course, the universal scaling behavior has limits. Additional simulations (not shown) indicate that the scaling relationship Eq. 6.16 breaks down for thin walled microjet nozzles, when $R_o/R_i < 1.5$, since Eq. 6.14 is no longer representative of the resistance in the annular gap.

6.4.2 *Secondary Current Scaling*

6.4.2.1 Reversible Bipolar Couple (Scheme 1)

Secondary current distribution computations for the reversible copper system in Scheme 1 were done to develop and test scaling relationships for the charge transfer resistances indicated in the equivalent circuit in Figure 6.1c. Figure 6.4 shows computations of overpotential and current density as a function of radius in the region beneath the microjet. Reaction conditions were evaluated at varying geometric configurations (H/R_i) by changing fly-height and ratios of applied current to area normalized exchange current density ($I_{app}/i_o A_{noz}$) by varying I_{app}. When $I_{app}/i_o A_{noz}$ = 1000, the overpotentials in Figure 6.4a are several hundreds of millivolts for every geometric configuration, consistent with Tafel approximated kinetics. The resistance to charge transfer is the derivative of overpotential with respect to current density evaluated at the characteristic current density (i_j^*) of the reaction

$$\bar{R}_{CT,j} = \left.\frac{d\eta_{s,j}}{di_j}\right|_{i_j^*} \tag{6.17}$$

where $\bar{R}_{CT,j}$ is an area-dependent resistance (Ω m^2). When kinetics follow Tafel behavior ($i_j^* >> i_{o,j}$) the characteristic charge transfer resistance is

$$R_{CT,j} = \frac{RT}{i_j^* A_j^* \alpha_j n_j F}. \tag{6.18}$$

Here, the area-dependent resistance is scaled by the characteristic area (A_j^*) through which the characteristic current density i^* flows, providing a pure resistance (units in Ω). The characteristic current (I_j^*) is the product of the characteristic current density (i_j^*) and area (A_j^*). The normalized current density plots in Figure 6.4d when $I_{app}/i_o A_{noz}$ = 1000 show sharp profiles at small geometric configurations, meaning that all of the applied current is passing through the conductive substrate directly beneath the microjet. Therefore, we expect that charge transfer for the near-field reaction

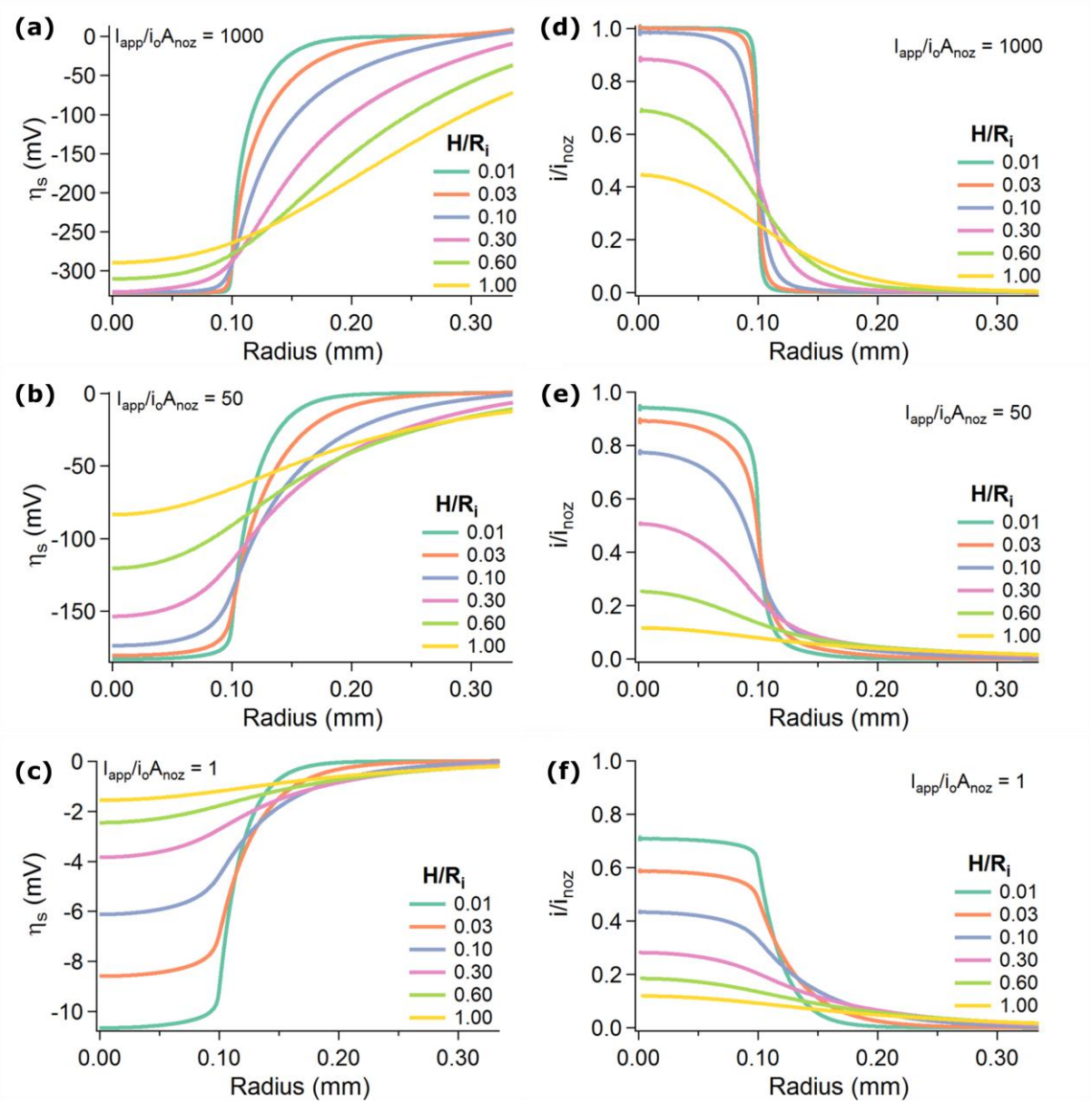

Figure 6.4. Surface current density and overpotential profiles for Cu bipolar couple Computed overpotentials (a-c) and current densities (d-f) for varying ratios of I_{app}/i_oA_{noz} and several geometric configurations in the region of the substrate directly beneath the microjet nozzle. At high applied currents, the kinetics follows a Tafel approximation. When applied current is on the order of i_oA_{noz}, the near-field reaction displays characteristics of linearized kinetics.

beneath the microjet nozzle ($R_{Ct,near}$) is dominated by the Tafel approximation with I_j^* equal to the applied current (I_{app}):

$$R_{CT,near} = \frac{RT}{I_{app}\alpha_j n_j F}. \tag{6.19}$$

The current density profiles in Figure 6.4d are all normalized to the current density exiting the microjet ($i_{noz} = I_{app}/A_{noz}$), providing a qualitatively spatial interpretation of the *BCE*. When the profile is sharp (H/R_i = 0.01, 0.03, 0.10) the *BCE* is close to 1, and all of the applied current passes into the substrate directly beneath the microjet exit. As the fly-height increases (H/R_i = 0.30, 0.60, 1.00), ohmic resistances are lower and the peak current densities and *BCEs* decrease. The current density profile also widens, with more of the applied current passing into the substrate beneath the microjet wall ($0.1 < r < 0.335$).

When the applied current is decreased ($I_{app}/i_o A_{noz}$ = 50), peak overpotentials in Figure 6.4b range from -80 mV to -200 mV at varying geometric conditions. Here, a couple of geometric conditions produce overpotentials under or near 100 mV, but overall Tafel kinetics remain a good approximation. The corresponding current density profiles in Figure 6.4e show that the peak current densities are all lower than in Figure 6.4d. Less applied current increases the characteristic charge transfer resistance in Eq. 6.19, decreasing the *BCE* for a given geometric condition. When $I_{app}/i_o A_{noz}$ is 1, the overpotentials in Figure 6.4c are about 10 mV or less for every geometric configuration. Here, we expect charge transfer to follow linear kinetics and the characteristic resistance to be independent of applied current:

$$R_{CT,j} = \frac{RT}{i_{o,j} A_j^* n_j F} \tag{6.20}$$

where resistance is again scaled by the characteristic area through which current flows. The corresponding normalized current density profiles in Figure 6.4f show peak current densities substantially less than what exits the microjet, producing lower *BCEs* than in Figure 6.4d-e. At

lower applied currents, we expect the Tafel scaling approximation in Eq. 6.19 will not accurately capture the kinetics of the near-field reaction.

Overpotential and current density plots in Figure 6.4 focus on the charge transfer reaction taking place in the near-field beneath the microjet. When the substrate is macroscopically large compared to SBC microjet dimensions (as is the case in our experimental systems), the area where the far-field reaction occurs (A_{far}) is about 500-1000 times larger than the area of the reaction beneath the microjet (A_{near}). Since the spatially segregated bipolar reactions must be equal and opposite, this results in average current densities and overpotentials in the far-field region ($R_{CT,far}$) characterized by the linear approximation for charge transfer resistance. Eq. 6.20 scales with characteristic area, and because $A_{far} >> A_{near}$, the charge transfer resistance for the far-field reaction is negligible compared to the resistance beneath the microjet. Thus, for scaling purposes, Eq. 6.19 is used to approximate the total charge transfer resistance to current flow through the conductive substrate. The overpotential and current density plots in Figure 6.4 show that the Tafel approximation for charge transfer resistance is most accurate at sufficiently high applied currents and low microjet fly-heights, where the characteristic current (I^*) is appropriately captured by I_{app}. However, since the actual current participating in charge transfer is I_e, Eq. 6.19 always underestimates charge transfer resistance, particularly when *BCE* is not close to 1.

The dimensionless Wagner number (*Wa*) can further generalize the phenomena for secondary current distribution systems. *Wa* captures the key differences between the ohmic and charge transfer contributions, and for the SBC is

$$Wa = \frac{R_{CT,near}}{R_{ionic}} \quad . \tag{6.21}$$

The relationship in Eq. 6.21 is useful for understanding the fundamental coupling between ionic migration and charge transfer resistance in the scanning bipolar cell. If applied current follows the

simple equivalent circuit in Figure 6.1c, then the dimensionless *BCE* in Eq 6.2 scales with *Wa* in the following manner:

$$BCE \sim \frac{1}{1+Wa}. \tag{6.22}$$

Figure 6.5 shows computed *BCEs* vs the scaling relationship in Eq. 6.22 (indicated by the black line). Applied currents expected to exhibit Tafel behavior were selected ($100 < I_{app}/i_o A_{noz} < 10000$). Computations show high *BCEs* for all cases. At low geometric configurations *BCEs* are close to unity and the estimated values correlate well with computations. We've previously shown Eq. 6.22 plotted in a form to emphasize small differences in *BCE*, namely *(1-BCE)/BCE* vs *Wa*, which demonstrates that the scaling prediction is not perfect[44]. As the geometric configuration increases the scaling relationship shows overestimations for *BCE*. The current density profiles in Figure 6.4

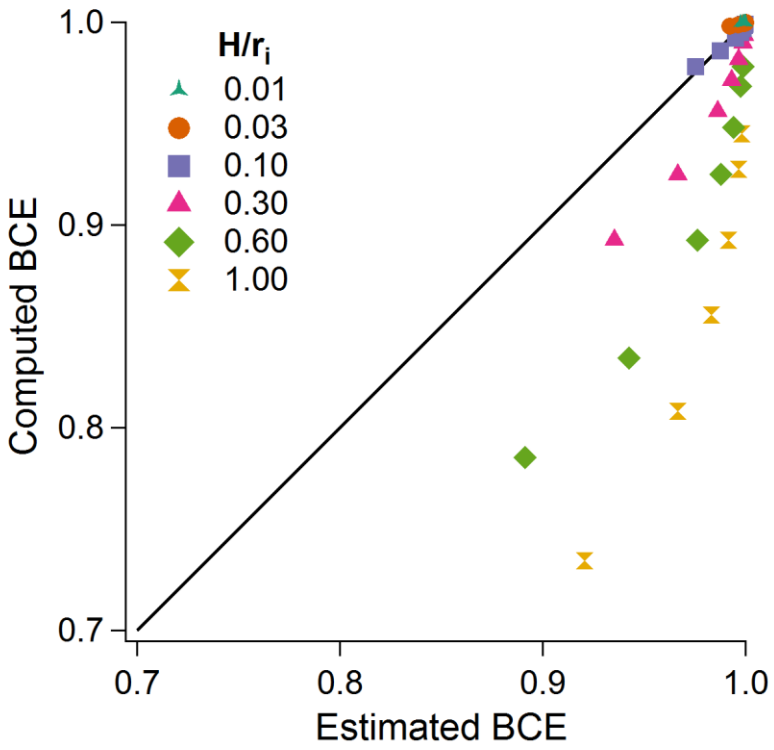

Figure 6.5. Scaling relationship for secondary current with Cu/Cu bipolar couple
Computed bipolar current efficiencies (BCEs) are plotted against estimated BCEs using Eq. 6.22 over a wide range of SBC geometries and applied currents.

at larger geometric configurations show lower peaks and broader profiles. Therefore the characteristic current is likely less than I_{app} and estimated charge transfer resistances are smaller than reality. In addition, as *BCE* decreases, less of the applied current is participating in charge transfer reactions at the conductive substrate resulting in further underestimations of charge transfer resistance. Nonetheless, the charge transfer resistance scaling in Eq. 6.22 captures the electrochemical behavior reasonably well for a reversible bipolar redox couple, demonstrating highly efficient bipolar electrochemistry is capable with the SBC.

6.4.2.2 Uphill Thermodynamic Bipolar Couple (Scheme 2)

The above analysis for a single reversible redox couple simplified the equivalent circuit in Figure 6.1c by having a thermodynamic potential difference equal to zero, and thus a gate voltage of zero for the transistor. However, many bipolar systems (such as in Scheme 2) employ two reactions from different redox couples, which can have nonzero values for ΔE_{BC}. In these systems, no current can pass through the conductive substrate and participate in bipolar electrochemistry until $E_{gate} > \Delta E_{BC}$. Thus, a minimum threshold current (I_{min}) is necessary to overcome the thermodynamic barrier and drive bipolar reactions. I_{min} is related to the thermodynamic difference of the bipolar couple by:

$$I_{min} = \frac{-\Delta E_{BC}}{R_{ionic}}, \tag{6.23}$$

where R_{ionic} is defined by Eq. 6.16.

Figure 6.6a shows computed normalized current density profiles in the region beneath the microjet at varying conditions of applied current when H/R_i = 0.10. When $I_{app} < I_{min}$, the thermodynamic potential difference for nickel reduction and ascorbic acid oxidation has not been exceeded and none of the applied current passes through the conductive substrate. In these computations, a small amount of limiting dehydroascorbic acid reduction current produces the

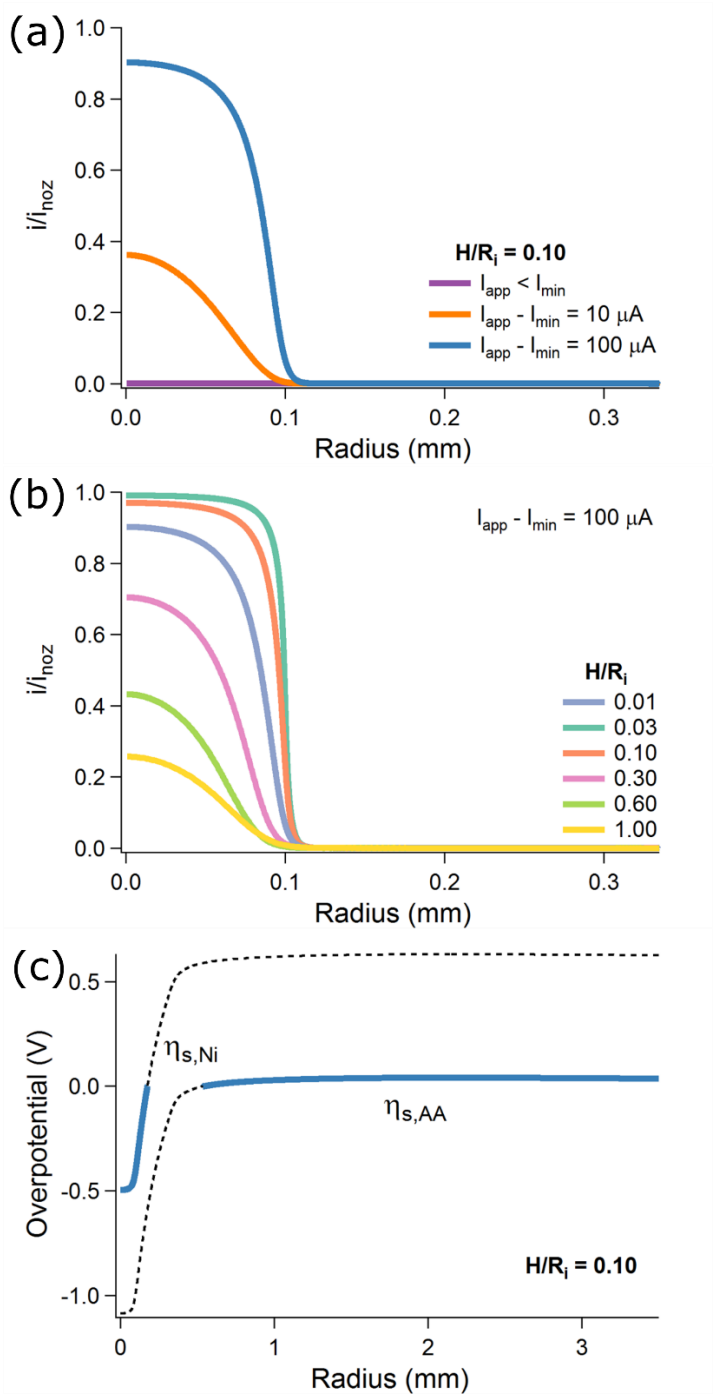

Figure 6.6. Computed current densities and overpotentials for the Ni/AA bipolar pair **a.** Normalized current density profiles in the region beneath the microjet demonstrating the relationship between I_{min} and I_{app}. **b.** Normalized current density profiles at varying geometric configurations when the characteristic current is 100 μA. **c.** Surface overpotentials for nickel and ascorbic acid across the entire substrate when the characteristic current is 100 μA and H/R_i = 0.10.

residual current density seen in Figure 6.6a. We have previously shown how to estimate I_{min} computationally[45] as the applied current where electronic current (I_e) through the substrate begins to increase significantly. I_{min} for the geometry in Figure 6.6a is 44 μA. Once ΔE_{BC} is exceeded ($I_{app} > I_{min}$) current can pass through the conductive substrate and participate in bipolar electrochemical reactions. The amount of applied current necessary to exceed I_{min} does not participate in charge transfer reactions, and thus does not contribute to the charge transfer resistance in Eq. 6.19. Therefore, the characteristic current for charge transfer resistance is the difference between I_{app} and I_{min} and

$$R_{CT,near} = \frac{RT}{(I_{app}-I_{min})\alpha_j n_j F} \tag{6.24}$$

assuming kinetics adhere to the Tafel approximation. Figure 6.6a shows that larger characteristic currents produce higher normalized peak current densities due to decreased charge transfer resistance, allowing for more applied current to pass through the conductive substrate resulting in higher *BCE*s. At conditions where $I_{app} > I_{min}$ the SBC behaves similarly to the reversible copper system in Figure 6.4. Figure 6.6b shows normalized current density profiles for a variety of geometric configurations when $I_{app} - I_{min}$ = 100 μA. When H/R_i is small the ohmic resistance is higher and more current is driven through the conductive substrate. Deviation of the normalized peak current density from 1 indicates smaller *BCEs*.

Figure 6.6c shows the computed overpotentials for nickel and ascorbic acid across the entire conductive substrate when $I_{app} - I_{min}$ = 100 μA and H/R_i = 0.10. The darkened regions indicate where substantial bipolar electrochemistry takes place; namely, nickel reduction ($\eta_{s,Ni} < 0$) and ascorbic acid oxidation ($\eta_{s,AA} > 0$). In the regions with the dashed lines, no bipolar electrochemistry can occur because the substrate overpotential is neither cathodic enough to drive nickel reduction nor anodic enough for ascorbic acid oxidation. The nickel reduction overpotential

(~ -500 mV) beneath the microjet nozzle is in the Tafel regime and the ascorbic acid overpotential (~ 40 mV) in the far-field is characteristic of linearized kinetics. The overpotential curves show a gap beneath the microjet where neither reduction of nickel nor ascorbic acid oxidation are significant (between r = 0.18 mm and r = 0.54mm). In our computations, current is driven by the aphyiscal dehydroascorbic acid reduction chemistry in this region. The potential drop across this gap is equal to the thermodynamic potential difference (ΔE_{BC}) necessary to drive the bipolar pair.

The scaling relationship relating *BCE* to *Wa* for the reversible copper system in Eq. 6.22 does not fully capture electrochemical behavior for bipolar couples with a thermodynamically uphill equilibrium potential difference. In previous work, we identified a new scaling relationship incorporating the minimum threshold current

$$BCE \sim \frac{1-{I_{min}}/{I_{app}}}{1+Wa}. \tag{6.25}$$

where the charge transfer resistance contribution in *Wa* was defined by Eq. 6.19. When $I_{app} < I_{min}$ Eq. 6.25 gives negative values for *BCE*, representing the condition when the transistor is off. Repeated computations such as those in Figure 6.6 were used to test the scaling relationship in Eq. 6.25. Figure 6.7 shows plots at varying geometric configurations comparing computed *BCE* to estimated *BCE* using Eq. 6.25 (indicated by the black line). In these plots, I_{min} was estimated by two methods: using the ohmic resistance scaling (R_{ionic}) in Eq. 6.22 (▲) and by estimating I_{min} computationally (♦). Calculated and computationally estimated values for I_{min} used in Figure 6.7 are given in Table 6.1. The ohmic resistance scaling relationship used to calculate I_{min} by Eq. 6.22 overestimates the *BCE* at every geometric configuration. When I_{min} is determined computationally, the scaling relationship in Eq. 6.25 predicts *BCE* far more accurately, especially at geometric configurations where H/R_i is small. This correlates well with the reversible copper system in

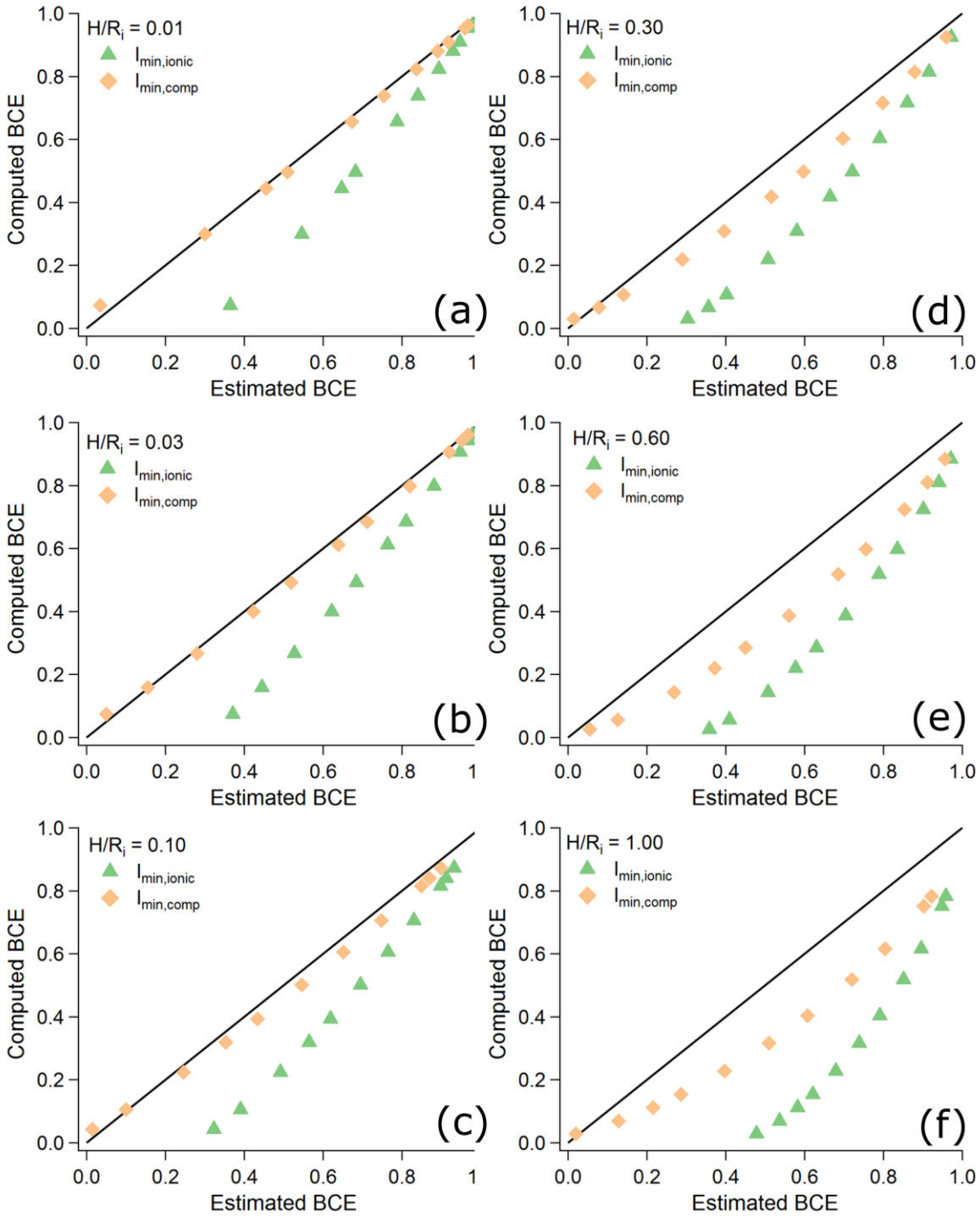

Figure 6.7. Computed *BCEs* vs predicted *BCEs* for Ni/AA bipolar couple

Comparison of computations to scaling in Eq. 6.25 at varying geometric configurations using different methods for estimating the minimum threshold current (I_{min}): estimated using Eq. 6.22 using R_{ionic} (▲) and estimated using computational methods (♦).

Figure 6.5, where the Tafel scaling relationship most accurately modeled kinetics at small geometric configurations. The expression for charge transfer resistance in Eq. 6.24 is accurate when a majority of the characteristic current ($I_{app} - I_{min}$) is passing through the conductive substrate. Therefore, when H/R_i is large significant current is lost to the ionic pathway and Eq. 6.24 underestimates the actual charge transfer resistance. The close correlation at small geometric configurations when calculating I_{min} computationally demonstrates that the scaling relationship in Eq. 6.25 accurately models bipolar behavior. Instead, we expect that the expression for ohmic resistance beneath the microjet does not effectively capture the full physicochemical behavior in a bipolar secondary current distribution system.

Table 6.1. Minimum threshold currents ($I_{\min}$) used in Figure 6.7.

H/R_i	Calculated I_{min} using R_{ionic} (μA)	Computationally determined I_{min} (μA)
0.01	3.05	4.71
0.03	9.07	13.9
0.10	29.3	43.5
0.30	80.5	116
0.60	142	211
1.00	200	392

The primary current computations clearly demonstrate that the expression for ohmic resistance beneath the microjet is accurately described by Eq. 6.16. However, the ability for partial current to pass through the conductive substrate in a secondary current system affects the potential variation beneath the microjet. This is evident when looking at equipotential contour plots for select primary and secondary current computations in Figure 6.8. Figure 6.8a-c show computations for the reversible copper bipolar couple when the substrate is an insulator (a), applied current gives

charge transfer kinetics characterized by the linear approximation (b), and when applied current produces Tafel kinetic behavior. When the substrate is an insulator, the ohmic resistance is effectively modeled by Eq. 6.16. Once charge transfer reactions occur on the substrate the potential lines that dictate ohmic resistance in solution show less bending through the annular gap, changing the characteristic ohmic resistance beneath the microjet from the primary current case. When the *BCE* is close to unity in Figure 6.8c, the potential drop through solution is equivalent to when the substrate is electrically connected to the current source.

Figure 6.8d-f show computations for the nickel reduction and ascorbic acid bipolar couple with a -590 mV thermodynamic barrier when the substrate is an insulator (d), when $I_{app} < I_{min}$ (e), and when $I_{app} - I_{min} = 100$ μA (f). When $I_{app} < I_{min}$ the equipotential contours match the condition when the substrate boundary condition is an electronic insulator. Here, *BCE* is effectively zero (any electronic current comes from residual dehydroascorbic acid reduction) and nearly all of the applied current is passing through the annular gap. When $I_{app} > I_{min}$ charge transfer occurs and current can pass through the conductive substrate. Again, there is less bending of equipotential lines beneath the microjet when charge transfer is active. The colored lines in Figure 6.8e-f compare the expected ionic current (I_i) through the annulus when estimating I_{min} computationally and using R_{ionic}. Computations show twice as much current flowing through the annulus than estimations using R_{ionic} producing an estimated *BCE* almost double that of the computations. Therefore, the characteristic ohmic resistance is smaller than what is computed in primary current ohmic scaling. The parallel nature of bipolar electrochemical systems means that the primary current ohmic resistance scaling does not accurately describe the characteristic ohmic resistance when significant charge transfer reactions take place.

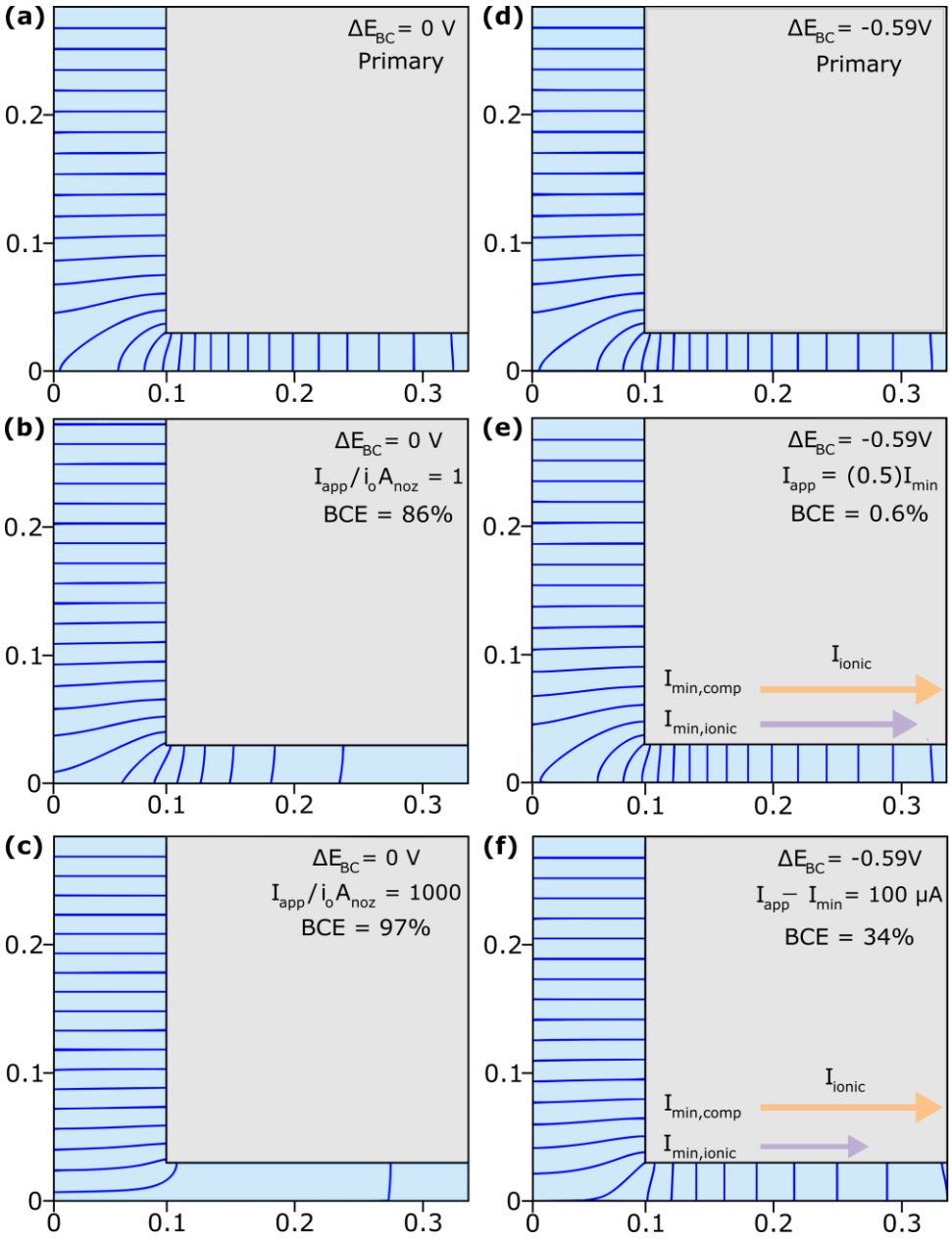

Figure 6.8. Equipotential contour plots

Constant potential contour plots for primary current and secondary current systems. Computations for the copper reversible bipolar couple comparing **(a)** primary current, **(b)** secondary current with linear approximation kinetics, and **(c)** secondary current with Tafel kinetics. Computations for the nickel and ascorbic acid bipolar couple comparing **(d)** primary current, **(e)** secondary current when $I_{app} < I_{min}$, and **(f)** secondary current when $I_{app} - I_{min} = 100$ μA. The lines in **(e-f)** depict (proportionally) expected ionic current (I_i) passing through the annular gap.

6.5 CONCLUSIONS

Finite element method simulations were used to test scaling relationships relating ohmic variation, charge transfer kinetics, and thermodynamics in a scanning bipolar cell. Previous chapters have demonstrated that scaling relationships are valuable for the developing experimental systems, and understanding when these scaling relationships break down is important. Ohmic, kinetic, and thermodynamic phenomena are captured in a linear equivalent circuit. The ohmic resistance scaling relationship was refined with the addition of a resistance related to a disk electrode, showing a strong correlation for ohmic resistance variation over several orders of magnitude. Secondary current simulations further explain charge transfer resistance relationships for two characteristic bipolar reaction couples. However, more complicated systems do not show a trivial universal scaling relationship. This is associated with how ionic current flows through the electrolyte in a bipolar system that has parallel current pathways. The unique coupling of ohmic variation, charge transfer kinetics, and thermodynamics in a bipolar system means that these phenomena can no longer be approximated independently of each other. An area for future research involves studying whether or not there are simple scaling arguments that incorporate kinetic and thermodynamic contributions into the ohmic resistance scaling in a bipolar system.

Chapter 7. TRANSLATION TO MARKET APPLICATIONS AND FUTURE RESEARCH ACTIVITIES

7.1 SUMMARY

In this chapter we discuss the impact of local bipolar electrodeposition and patterning with a scanning bipolar cell in industrial and research applications. In the device under test industry, gold testboards wear down after repeated contact with integrated circuit computer chips, testing functionality before packaging into electronic devices. Bipolar electrodeposition of gold with the SBC presents a technique for repairing damaged testboards in an automated and efficient manner. Local bipolar electrodeposition has the potential for significant impact in additive manufacturing. Currently, additive manufacturing is dominated by 3D printing technologies with user friendly integrated hardware and software. Most current electrodeposition additive manufacturing technologies require complex processing and are not software reconfigurable. The SBC offers a method for bridging desirable qualities of electrodeposition with full software control seen in commercially successful 3D printing technologies. A new electroanalytical tool combining bipolar electrochemistry and electrochemical impedance spectroscopy is proposed for *in-situ* monitoring of electrodeposition material growth and local charge transfer kinetic analysis.

7.2 SEMICONDUCTOR TESTBOARD REPAIR

Every year the semiconductor industry tests over 750 billion integrated circuit units, utilizing complex and expensive gold-plated test boards that can cost tens of thousands of dollars to manufacture. These testboards are custom designed for each individual integrated circuit generation and often wear out within 1-2 years due to constant contact rendering them useless. The

lifetime of an integrated circuit device is 3-4 years, meaning a typical testboard lasts for only half of a semiconductor device cycle. The amount of damaged gold is often less than 0.1% of the total surface area and the remaining, completely functional, gold is chemically recovered for reuse. The original manufacturers of the test boards do not have an industry qualified and cost effective method for repairing testboards, requiring the semiconductor test companies to purchase new boards upon deterioration. However, testboard manufacturing companies are losing repeat sales due to the emergence of black market techniques for refurbishing damaged testboards. These black market processes include knock-off counterfeit boards and by-hand brush based spot repair. None of these techniques meet industry standards and waste a significant amount of gold, in addition to infringing upon original manufacturers' intellectual property. A viable repair process will extend the lifetime of a single manufactured testboard to that of a computer chip life cycle and provides a route for manufacturers to capture repeat sales they are currently losing to black market techniques.

The scanning bipolar cell (SBC) provides an innovative method for local electrochemical spot repair of these damaged gold testboards. As demonstrated in previous chapters, proper electrolyte design enables local electrodeposition of a wide variety of metals with no need for an electrical connection to the substrate. The ability to perform electrodeposition without an electrical connection is essential. Each testboard is custom manufactured and patterned with differing conducting and non-conducting regions. Additionally, a single testboard can have several defected areas from testing wear. Finding and making electrical connections to each defected area for differing types of testboards is difficult and time-consuming, reducing repair and cost efficiency when using traditional electrodeposition (EcP) spot repair. With the SBC, spot repair is much more automated, especially when combined with optical scanning technology capable of rapidly identifying defected areas.

The technique for optimizing electrodeposition for semiconductor testboard repair is similar to what was presented in the previous chapters. In this case, the material deposited is gold. Initial tests were done using an alkaline gold electrolyte: 0.1 M $KAu(CN)_2$, 0.01 M KCN, and 0.01 M ascorbic acid (pH = 9.9). Note that in future gold experiments we used KOH as buffer/supporting electrolyte instead of KCN to create a more irreversible bipolar deposition electrolyte. As mentioned in Chapter 4, the optimal electrolyte pH for alkaline gold bipolar electrodeposition is between 8 and 10, which is less than the second pK_a (11.6) value for ascorbic acid. Figure 7.1 shows a typical scanning bipolar cell screening test for this electrolyte with our standard 200 μm ID and 670 μm OD nozzle. The 5x5 array varies applied current (I_{app}) along the horizontal axis in 50 μA increments and fly-height (H) along the vertical axis in increments of 9 μm. Deposition times were held constant at 5 seconds and electrolyte flowrate was constant at 400 μL min^{-1}. Deposit spacing is 400 μm center to center. The bipolar electrolyte formulation used here is thermodynamically uphill, with $\Delta E_{BC} \sim$ -0.91V, which must be exceeded before bipolar electrodeposition occurs. This is evident at low applied currents and high fly-heights, where very little deposition occurs because the substrate ohmic polarization is not sufficient to exceed the thermodynamic barrier. At high applied currents and low fly-heights, the gold deposits appear to be “burned” in the center. This is likely due to secondary hydrogen gas coevolution occurring at the higher current densities in the center of the deposits, as discussed in detail in Chapter 4 for nickel reduction and ascorbic acid oxidation. These screening tests aid in determining the optimum SBC operating window for any given electrolyte.

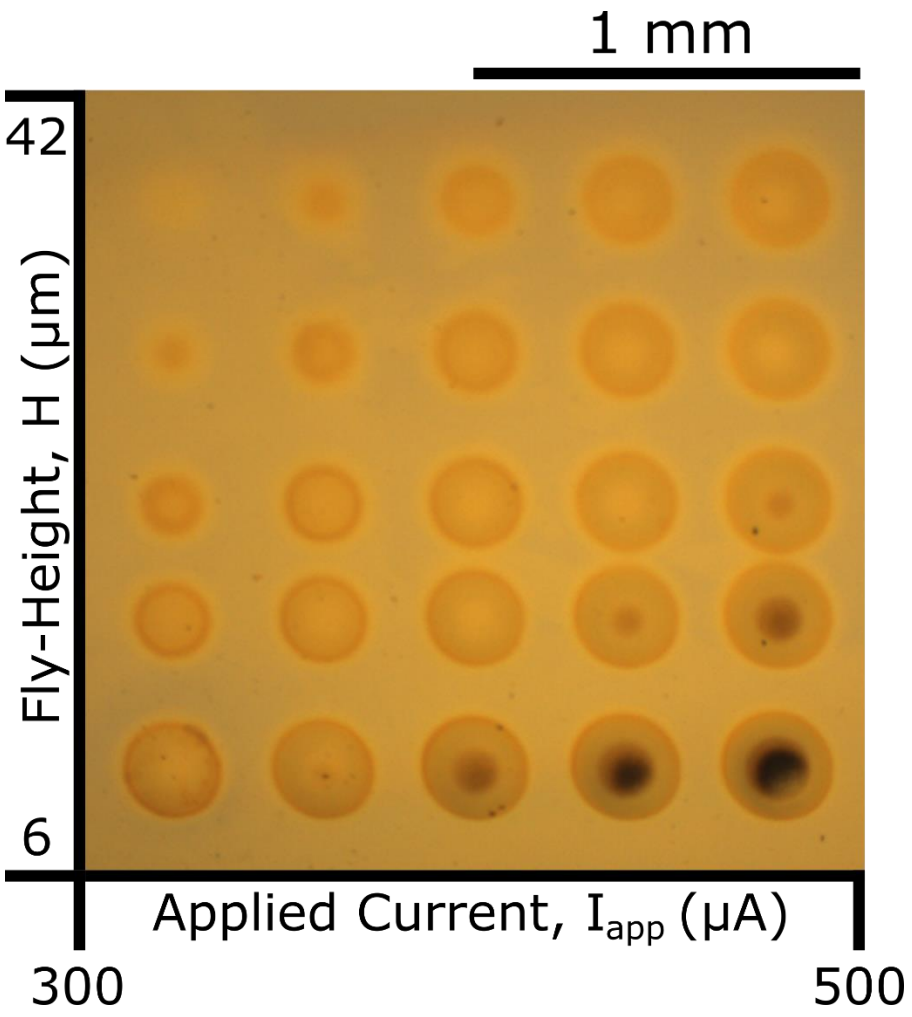

Figure 7.1. Array of gold bipolar electrodeposition

Optical micrograph of gold deposits on a gold substrate deposited at a range of applied currents and nozzle fly-heights using ascorbic acid oxidation as the far-field bipolar oxidation chemistry.

Ideal conditions from screening experiments such as in Figure 7.1 are used to repair damaged areas on a semiconductor testboard. Figure 7.2a shows an image of a probe card used for integrated circuit testing. Defects in the gold circuitry are apparent when zoomed in to the region within the dashed box seen in Figure 7.2b for several contact locations and for a single contact location (Figure 7.2c). The SBC is then used to remetallize the worn areas as shown in Figure 7.2d.

Gold was deposited at an applied current of 1100 μA for 10 seconds per deposit at a fly-height of 6 μm using the electrolyte above but with KOH as buffer. According to our screening test in Figure 7.1, these conditions would produce poor gold deposits with high levels of hydrogen coevolution in the center of the deposit. In Figure 7.1, bipolar deposition occurs on a macroscopic, clean gold substrate produced by physical vapor deposition. The defected region of the probe card has spatial dimensions on the order of the deposit size, which can reduce bipolar current efficiencies. In addition, the gold surface of the probe card was not pre-treated before bipolar electrodeposition, likely creating conditions of higher charge transfer resistance further diminishing the *BCE*. These

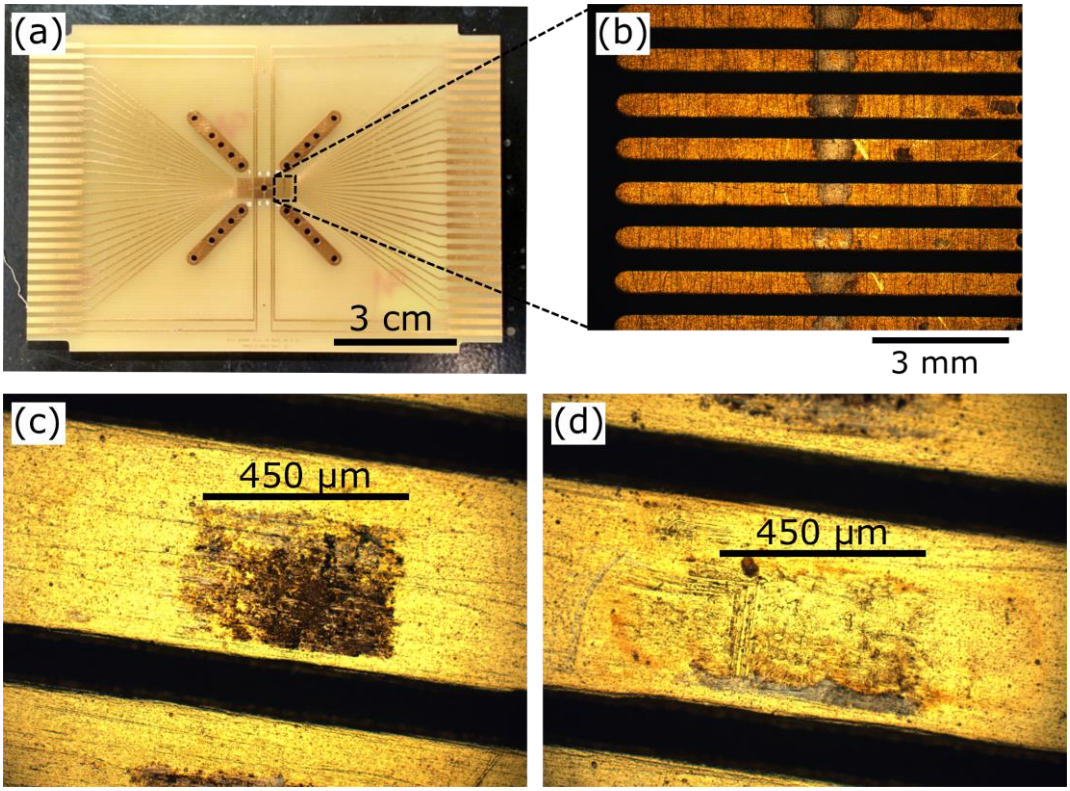

Figure 7.2. Remetallization of a probe card

Optical micrographs show the defects created by repeated contact during integrated circuit testing. (a) Optical micrograph of a full probe card used in testing and a zoomed in region (b) depicting defects caused by repeated contact. Isolated defects (c) can be remetallized (d) with the SBC without needed to make any electrical connections to the surface.

factors must be considered when determining the operable deposition window for an electrolyte, as lower *BCEs* require higher applied currents to achieve the same quality of deposition.

The experiments performed in Figure 7.1 and Figure 7.2 used a simple alkaline gold electrolyte to demonstrate the viability of the SBC as a repair tool for damaged semiconductor testboards. However, pure gold metal is soft and malleable and therefore typically alloyed to improve hardness for use in semiconductor device circuitry. In order to meet industry standards, the gold must be deposited as a "hard" gold alloy, consisting of 99.7% minimum gold content alloyed with either cobalt or nickel (Type 1 ASTM-B-488-01). Hard gold plating baths are typically formulated at mildly acidic conditions ($6 > pH > 4$), and require additional care because HCN gas can form in lethal concentrations when $KAu(CN)_2$ is mixed with strong acids. Developing and testing a hard gold plating electrolyte for use with the scanning bipolar cell is the next step in producing a viable industry qualified repair process for semiconductor testboard repair.

7.3 ADDITIVE MANUFACTURING

7.3.1 *Summary*

Recent advances in rapid prototyping technologies have generated a surge of users and applications for additive manufacturing. Driving this surge is the availability of easy-to-use integrated software/hardware platforms that can directly convert a computer aided design file into the fabricated object, accelerating the design-build-test cycle. Despite these advances, a similar shift to fully software reconfigurable electrodeposition-based prototyping has yet to emerge. Current commercial electrodeposition fabrication techniques involve hardware masks or stamps to develop their patterns, placing limitations on their reconfigurablility. However, the elements of fully software reconfigurable electrodeposition-based rapid prototyping are emerging. In this section, we review some of the most commercially successful rapid prototyping technologies currently available, describe existing commercial electrodeposition systems such as EFAB/MICA, and highlight the efforts in our lab to develop software reconfigurable electrodeposition freeform fabrication techniques for additive manufacturing.

7.3.2 *Background on Additive Manufacturing Techniques*

Additive manufacturing has evolved over the past three decades to the point where current methods encompass lateral and vertical resolutions ranging from nanometers to centimeters, as shown in Figure 7.3[17,109,110]. The first of these technologies commercialized was stereolithography (SL), which uses a photosensitive liquid polymer that hardens when an ultraviolet laser impinges on the resin[111]. The partially cured object is then lowered into the liquid to allow for curing of each subsequent additive layer. Stereolithographic resolutions are typically in the millimeter range, but the development of microstereolithography (MSL) has enabled additive manufacturing at sub-

micron level resolution[112,113]. However, SL and MSL have limited material capabilities as they require photosensitive polymers. Selective laser sintering (SLS) is similar to SL, except a solid powder is sintered (fused) by the application of a high-energy carbon dioxide laser beam[114]. The primary advantage of SLS is increased material capabilities (polymers, metals, and composites), but the vertical and lateral resolutions are typically in the millimeter range due to laser focus diameter, powder granule size limitations, and thermal conduction beyond the laser focus. Similar technologies to SLS include electron beam melting (EBM) which uses an electron beam instead of a carbon dioxide laser to melt the powder and laser engineered net shaping (LENS) which injects the powder into a specific location before then heating it with a high powered laser[109].

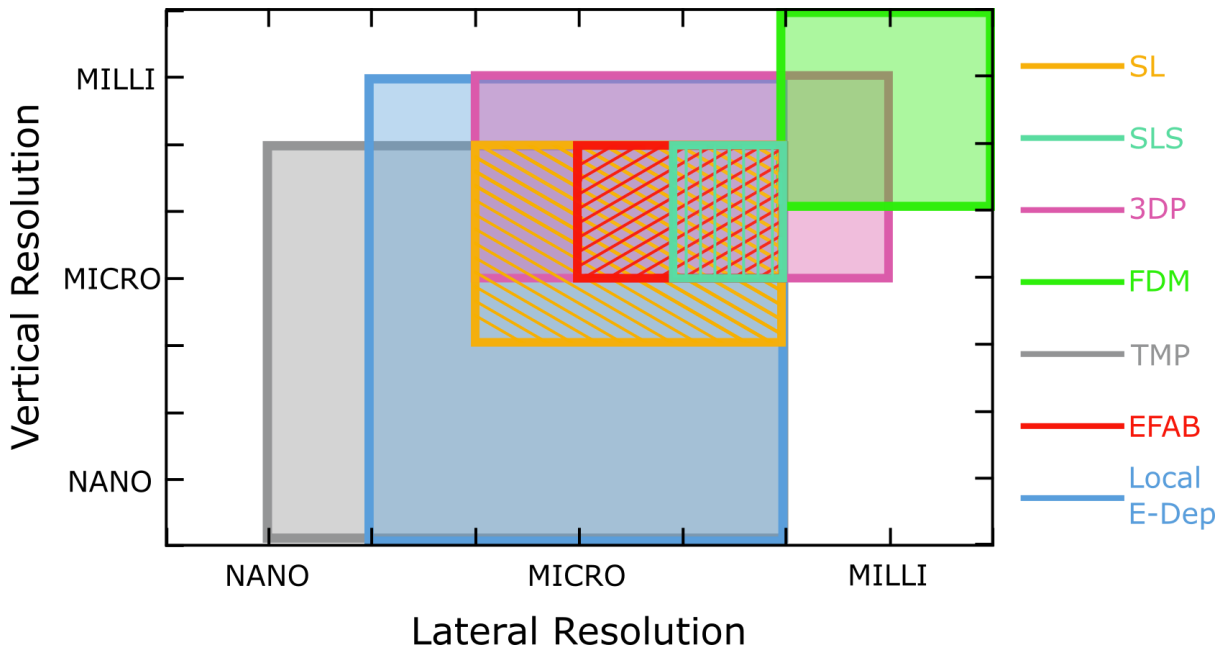

Figure 7.3. Summary of additive manufacturing spatial resolutions

The lateral and vertical resolutions for various additive manufacturing techniques govern the kinds of objects that can be fabricated. Shown here is the approximate design space for seven different additive manufacturing methods. Abbreviations for each method are given in the text.

The 3DP process (developed at MIT) also uses powder as the material stock but instead applied inkjet nozzle technology to deliver liquid binder[115]. 3DP eliminates the need for high powered lasers or electron beams and achieves better resolution than SLS, but was originally limited to powdered polymer materials. Later, Prometal developed a steel powder and liquid binder to form metal features in a manner similar to 3DP[109]. However, Prometal fabricated steel objects typically required high temperature sintering as a post-processing step to fuse the metals. Fused deposition modeling (FDM) processes have recently become the most commercially available additive manufacturing technology because of the inexpensive machinery and low materials cost. Ubiquitous machines like "Makerbot" rely on low melting point polymer filaments to transfer liquid polymer to the object, followed by solidification. Despite the low cost, commercial FDM systems are limited to printing thermopolymers and often have millimeter scale XY resolution as set by the diameter of the extrusion nozzle.

Stereolithography, selective laser sintering, 3DP, and fused metal deposition represent some of the most common methods for additive manufacturing. While each has attributes and limitations, taken in aggregate, AM technologies are seeing explosive growth. For example, Figure

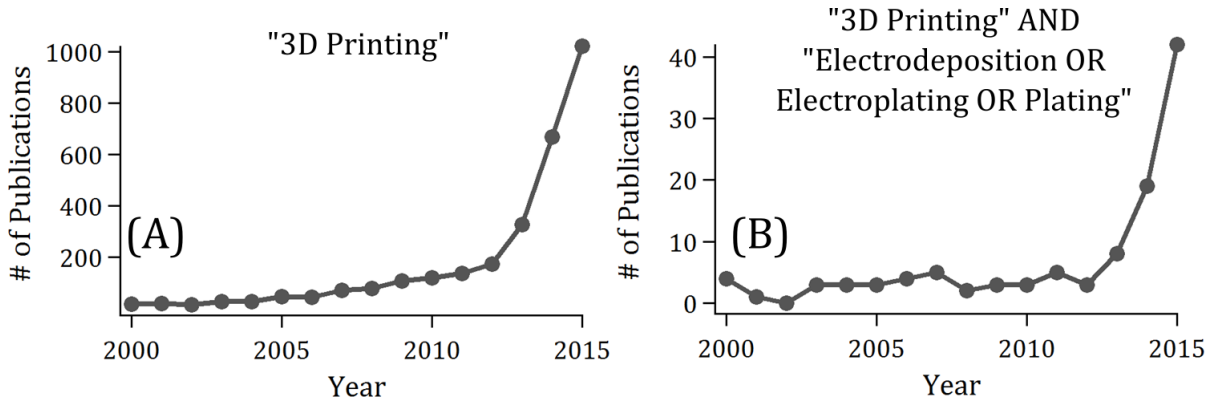

Figure 7.4. Publication trends in additive manufacturing

Publication trends involving 3D printing are revealed for topic searches involving the terms **(A)** "3D Printing" and **(B)** the subset of topics that also include "Electrodeposition OR Electroplating OR Plating".

7.4A shows the publication trends for a topic search of “3D Printing” in the WebOfKnowledge search engine. Research publications on 3D printing grew slowly for years, but there has been an exponential increase in publications starting in 2012.

7.3.3 *Electrodeposition Additive Manufacturing Techniques*

What role has electrodeposition played in the growing field of AM? Figure 7.4B shows the publication trend from a search in WebOfKnowledge for “3D printing AND (Electrodeposition OR Electroplating OR Plating)”. Electrodeposition based 3D printing research has an almost identical growth trend as in Figure 7.4A but is involved in a tiny fraction of the total 3D-printing publications. Electrodeposition based additive manufacturing technologies offer a potential solution to the material limitations of the technologies highlighted above (deposition capabilities include metals, alloys, semiconductors and polymers) while also improving the lateral and vertical resolution capabilities[8]. Electrodeposition is particularly unique in its ability to create films at sub-nanometer (monolayer) vertical resolutions, enabling an unexploited market for 3D-printing AM. Clearly, electrodeposition additive manufacturing is a rich, untapped space for additional research efforts.

The standard for electrodeposition additive manufacturing and patterning is through-mask plating, which has been highly utilized for development of integrated circuits, printed circuit boards, and hard drive components. This technique requires a mask to create the patterned layer and typically needs several deposition and material removal steps to fully develop the pattern. Recent years have seen the development of new electrodeposition methods utilizing flexible masks and sacrificial material in an attempt to reduce fabrication steps and increase geometric complexity of the fabricated structure. One example from our lab uses flexible masks for through-mask plating

of 3D shapes[116]. Pliant masks are laser cut to the desired shape and then adhered to nonplanar conductive substrates. After electrodeposition, the masks are removed, producing features such as the NiFe coil structure in Figure 7.5A. Another method for layered manufacturing utilizes sacrificial material that is etched after electrodeposition to create 3D features[117,118]. In this system, varying mass transfer rates or current densities during deposition of NiFe alloys can produce sacrificial iron-rich layers and retained nickel-rich layers from a single bath. This manufacturing method is capable of producing 3D features such as the microgear in Figure 7.5B, where a standard through-mask plated object (an extruded 2D shape) has embedded 3-D layers that can be partially or fully etched[118].

The most sophisticated and commercially successful electrochemical technology utilizing sacrificial materials for 3D fabrication is electrochemical fabrication (EFAB) or MICA (a second generation form of EFAB), which has been commercialized by Microfabrica[17,18]. EFAB is a three-step process (per layer) consisting of sacrificial material deposition, structural material deposition, and surface planarization. First, a sacrificial material (normally copper) is deposited using a pre-fabricated negative micromold. Then, the retained material (normally nickel) is blanket deposited, filling in gaps left by the micromold and also depositing on top of the sacrificial material. Finally, both materials are planarized to the desired layer thickness. After repeating until all of the layers of the build are completed, the sacrificial material is etched leaving only retained structural material with microfeature line rules down to 20 μm. Figure 7.5C shows an SEM image of a gyrocscope consisting of 31 layers fabricated using the EFAB process[119]. Despite EFABs success in microfabrication, it does not possess all of the traits for additive freeform fabrication, since there are hardware masks and layer-to-layer planarization. Through-mask plating and EFAB have some material selection advantages and better spatial resolution than SL, SLS, 3DP, and FDM but are

not fully software reconfigurable. Specifically, through mask plating and EFAB each use physical masks or stamps to develop their patterns. Direct write (DW) electrodeposition methods are needed to bridge the resolution and material capabilities in electrodeposition additive manufacturing with user friendly software reconfigurable techniques like FDM and SLS.

7.3.4 *Localized Electrodeposition for Additive Manufacturing*

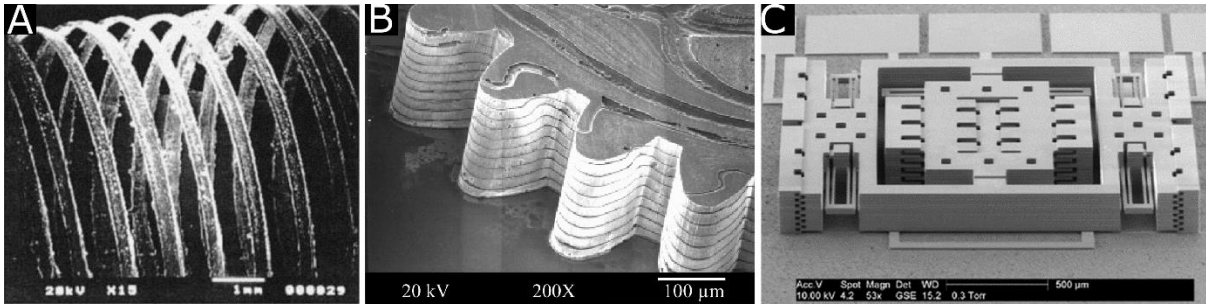

Figure 7.5. Electrodeposition using masks and sacrificial materials

Examples of electrodeposition creating successively distinctive three dimensional objects. **(A)** Flexible laser-cut masks are used to create a 3D nickel coil structure[116]. **(B)** Embedded sacrificial layers can be placed within traditional 2D extruded through-mask plated objects[118]. **(C)** Repeated through-mask electrodeposition of sacrificial copper, blanket electrodeposition of retained nickel, and planarization, enables automated many-layer builds such as a gyroscope fabricated using EFAB[119].

There have been several attempts to use localized electrochemistry for direct write patterning as a software reconfigurable solid freeform fabrication method. The use of microelectrodes to confine current density locally on a conductive substrate has shown growth rates on the order of μm s^{-1} [8]. Application of an electric field between a conductive substrate and a microelectrode in close proximity produces a highly localized current distribution at the substrate. The lateral resolution of the current distribution is dictated by the dimensions of the microelectrode. Highly developed scanning probe technology such as scanning electrochemical microscopy (SECM) and scanning tunneling microscopy (STM) have demonstrated nanometer

scale patterning for both electrodeposition and etching[19-21]. Microelectrode direct write electrodeposition addresses local control of current density and can easily achieve sub-micron resolution, but has diffusion limited mass transfer rates, which can limit material growth rates. Impinging jet electroplating systems address mass transfer limitations by providing controllable convective-diffusive mass transfer rates at the substrate. One of the first direct write jet-plating methods was developed by IBM in 1982 (laser-jet electroplating)[22-25]. This technology is able to achieve deposition rates of 50 μm s^{-1} by combining jetted convection with a linearly-directed laser to further improve mass transfer and kinetic rates. Control of mass transfer and local current density enables a wide range of materials to be deposited, and can be software reconfigurable.

Our laboratory expanded on impinging jet electroplating systems by implementing full software control of all electrodeposition and mass transfer parameters with a tool called Electrochemical Printing (EcP), enabling flexible electrodeposition of metals and alloys in a raster or vector drawing mode[26-29]. Figure 7.6A describes how EcP works. Software images (Figure 7.6.A, top) are used to define print locations and system operating conditions: microjet fly-height (*h*, distance from microjet nozzle to substrate), electrolyte flow rate (*v*), and applied current and charge. These conditions are loaded into the custom software that controls each parameter (Figure 7.6B). Figure 7.6C shows a schematic of the EcP print head and key features. A platinum anode is inserted upstream of the microjet outlet and the microjet nozzle diameter (*d*) and fly-height (*h*) are critical dimensions for deposit resolution. Full software control enables easily repeatable patterned deposition such as the copper on gold “Scale” pattern shown in the optical micrograph in Figure 7.6D. Here, we see that decreasing fly-height clearly improves deposit resolution, as current is more localized at the substrate. The serial nature of local electrodeposition techniques presents a major barrier to commercial implementation of EcP. However, a US Patent awarded in 2009

addresses the design rules for a multi-pixel print head which enables parallel patterning and increased throughput[77].

Convective-diffusive mass transfer control allows deposition of a wide range of alloy materials from a single bath. This was first demonstrated with EcP through copper-nickel alloy

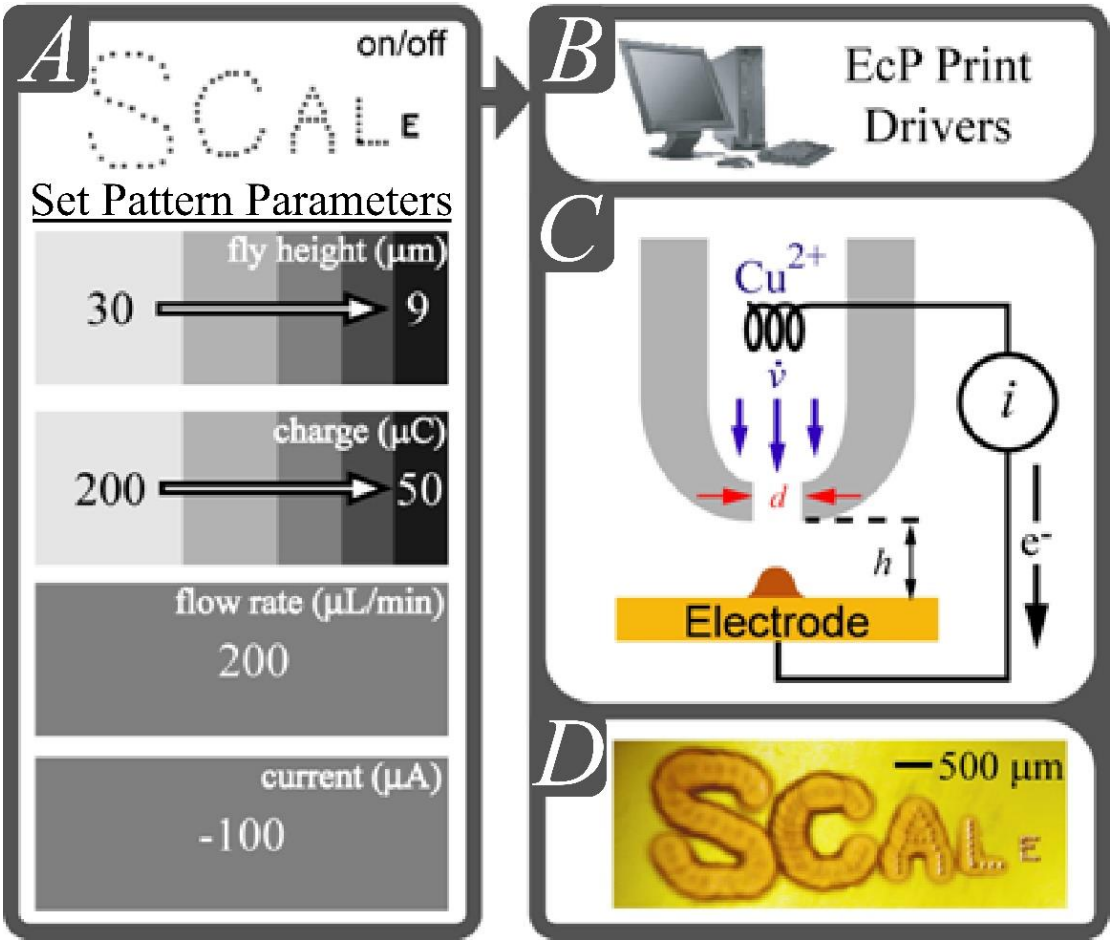

Figure 7.6. EcP schematic and process

Shows a schematic for software reconfigurable operation of Electrochemical Printing. **(A)** A bitmap image indicating deposit location nd process parameter selection is uploaded to a computer software program **(B)** with appropriate electrochemical and mass transfer operating conditions. This information is relayed to the EcP tool (schematic shown in **(C)**) which produces the corresponding copper pattern **(D)**. Image courtesy of Jeff Nelson.

deposition from a single bath (0.7 M $NiSO_4$, 0.004 M $CuSO_4$, and 0.500 M Na citrate). Figure 7.7A shows a 3D topographical map and a series of energy dispersive x-ray spectra (EDX), plots (a-f), for a 10x10 array of copper-nickel dots deposited under varying applied current and flow rates. EDX spectra show that copper-nickel alloy composition can be tailored by both the applied current and mass transfer conditions. The highest copper composition (*b*) occurs under low applied current and high mass transfer conditions, whereas the highest nickel composition (*e*) occurs at low mass transfer and high applied current conditions. These observations are consistent with kinetically limited nickel deposition and mass transfer limited copper deposition. These results show how EcP can be used to deposit both sacrificial (copper) and retained (nickel) materials from a single bath. This is the foundation for layered microfabrication from a software reconfigurable system.

EcP can further be modified to allow for much greater compositional control of the deposit by switching the electrolyte composition. This was achieved by adding a low volume micromixer upstream of the microjet nozzle outlet, providing rapid mixing of up to 4 individual bath streams. In this configuration, material composition is controlled by mixing individual bath components on the fly while printing, and then setting flow and current density that is optimal for that bath. Figure 7.7B shows an optical micrograph of a raster layer printed using EcP with on-the-fly mixing of baths in the micromixer. First, nickel raster dots were deposited at select locations from a 0.3 M $NiSO_4$, 0.014 M Na acetate, and 0.014 M acetic acid bath. After the nickel pattern finished, a copper bath (0.1 M $CuSO_4$ and 0.001 M H_2SO_4) was mixed on the fly, and another raster layer was printed, filling in the pattern. The Ni EDX image in Figure 7.7C, clearly reveals the nickel-rich material in the pattern “ECS”. In Figure 7.7D, the copper material in the layer was chemically etched with household ammonia cleaner, leaving only the nickel ECS pattern. The EcP micromixer

provides rapid, local elemental material composition control demonstrating a proof-of-concept method for software reconfigurable layered manufacturing using EcP. This one layer build is the starting point for more complex, but fully software controlled, 3D printing in metal.

In recent years, we have simplified the EcP tool so it can operate using bipolar electrochemical reactions, making it possible to do patterned electrodeposition without any need

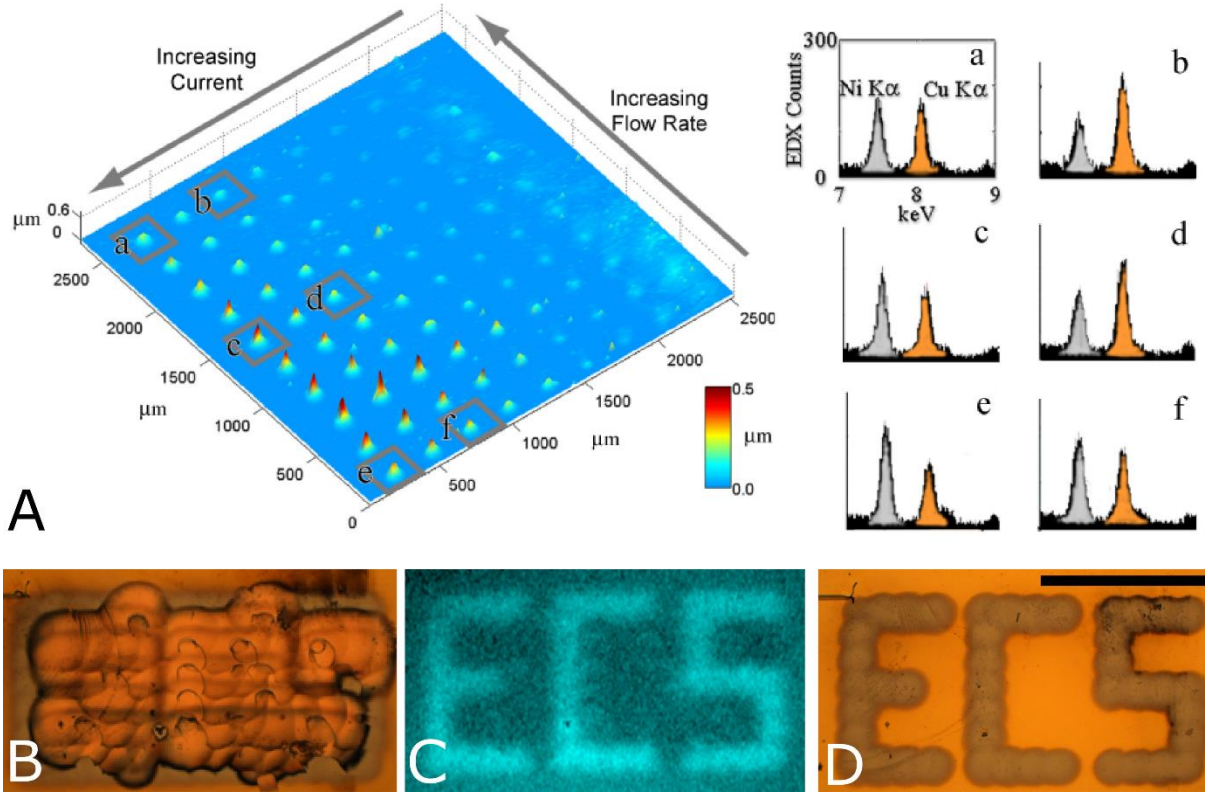

Figure 7.7. Control of metal composition using EcP

Local control of material composition using electrochemical printing (EcP). **(A)** Stylus profilometry (left) of nickel-copper alloy deposits in a 10x10 array of varying applied currents and electrolyte flow rates. EDX spectra (right) show copper and nickel Kα peaks indicating material composition for the deposits highlighted in the array. (B) Optical micrograph of nickel and copper material deposited in a single layer pattern using the EcP micromixer providing pure metal deposition control. **(C)** EDX map of the pattern in (B) showing nickel rich pattern within the single layer. **(D)** Optical micrograph of the pattern in (B) after chemical etching the sacrificial copper metal leaving only the nickel ECS logo remaining. Scale bar is 1mm.

for an electrical connection to the substrate[44,45,107]. This configuration is potentially advantageous for additive manufacturing on surfaces that are difficult to electrically connect to, at the expense of needing more sophisticated electrolyte engineering. We have so far demonstrated bipolar micropatterning of copper, nickel, silver, and gold using our software reconfigurable scanning bipolar cell (SBC).

We routinely perform EcP and the SBC in the micro to milli resolution regime. The scaling relationships for these microjet-based electrochemical systems have been studied and are well-understood[44,45,107]. The high mass transfer provided by the micro-jetted electrolyte eliminates concentration gradients at the substrate, allowing these systems to be approximated with a secondary current distribution (limiting current densities can exceed 10 A cm^{-2})[27]. Scaling of secondary current distribution systems are described by the dimensionless Wagner number, relating charge transfer resistances to ohmic resistances in the cell. Simple scaling relationships for these resistances as a function of operating parameters and geometric conditions provide insight for future scale-down to sub-micron patterning.

7.3.5 *Conclusion*

Additive manufacturing technologies have continued to evolve over the past three decades to meet the needs of manufacturing industries, researchers, and hobbyists alike. Techniques such as SL, SLS, 3DP, and FDM have been at the forefront of commercial additive manufacturing due to software control enabling greater design flexibility. FDM additive manufacturing has recently had great commercial success. Electrodeposition methods for additive manufacturing have also found significant commercial opportunities. Despite this, electrodeposition systems that are fully software controlled are just beginning to emerge. To bridge the advantages of techniques such as FDM with advantages of electrodeposition techniques like through-mask plating, localized

electrodeposition methods have been explored. In our laboratory, electrochemical printing was developed for local electrodeposition, providing higher material growth rates to due to high convective-diffusive mass transfer. The full software control of mass transfer and electrochemical parameters in EcP provides excellent deposit composition control, an attractive feature for 3D fabrication that relies on patterning sacrificial and retained materials. Further software design and automation is necessary to drive this technology toward the sophisticated layered manufacturing displayed by methods such as EFAB/MICA. As 3D printing continues to grow, additional research efforts in software reconfigurable, direct write electrodeposition will create an alternative pathway for additive manufacturing, particularly at sub-micron resolutions.

7.4 In-Situ Electroanalytics using Electrochemical Impedance Spectroscopy and Local Bipolar Electrochemistry

7.4.1 *Background and Statement of Problem*

Scanning probe electrochemical methods have been at the forefront of electroanalytical chemistry over the past few decades. Methods such as scanning electrochemical microscopy (SECM) and scanning ion conductance microscopy (SICM) have been used for non-contact topographical mapping of surfaces, electrocatalytic evaluation of materials, and dozens of other electrochemical applications[80]. Despite major advances in analytical applications, scanning electrochemical microscopy has not been extensively used for 2D/3D local electrodeposition and material fabrication. SECM fundamentally relies on solvated redox species to mediate the microelectrode substrate interaction and is therefore often a diffusional mass-transfer limited process. To alleviate the mass transport constraint on the local electrochemistry, microjet electrode systems have been developed with extreme mass-transfer rates useful for evaluation of rapid heterogeneous reaction kinetics and material growth[22,24]. The high deposition rates, up to 30 μm/s, are particularly appealing for 3D material fabrication applications.

In recent years, bipolar electrochemistry has been utilized to overcome some of the limitations of traditional electrochemistry; such as the difficulty in electrically connecting to micro/nanoscale electrodes and the ability to address multiple electrodes simultaneously with a single pair of feeder electrodes. While these advantages come at the expense of more sophisticated electrolyte engineering, bipolar electrochemistry has enabled exciting new applications ranging from electrocatalyst screening of material arrays to selective functionalization of microparticles[39]. Performing electrochemistry at a substrate with no electrical connection is particularly appealing

for micro and nanoscale fabrication, where electrically connecting to multifaceted conducting and insulating surfaces is difficult and time consuming.

Here, the proposed research is to develop a new electrochemical tool (from here on referred to as a *scanning bipolar probe*) that combines desirable aspects of scanning probe electroanalytics, high mass-transfer control via microjet electrodes, and the ability to address and modify substrates with no direct electrical contact using bipolar electrochemistry. This will be the basis for new research efforts employing in-situ electrochemical measurements during material fabrication and will add to the current suite of scanning probe methods currently available for electrochemical analytics.

7.4.2 *General Methodology*

The project will involve four major stages as illustrated in the Figure 7.8 flowchart. First, the scanning bipolar probe will be built and tested for subsequent research experiments. The software and hardware necessary to operate this system are the same as what is currently used in standard SECM systems, where piezoelectric stages provide X-Y-Z motion control at 10s of nanometer movements. A block diagram of the electrochemical system is shown in Figure 7.9a. Collaboration with current researchers with expertise in pipette-pulling and use of nanofabrication facilities will provide the methods necessary to fabricate the scanning bipolar probe nozzles. Fabrication of the potential sense electrode on the nozzle can be done in a similar manner to fabrication of current SECM/SICM probes[120]. The nozzles will be interchangeable, allowing for different resolution capabilities. Low volume flow pumps (either gear driven or piezoelectric) will provide mass-transfer control at the substrate.

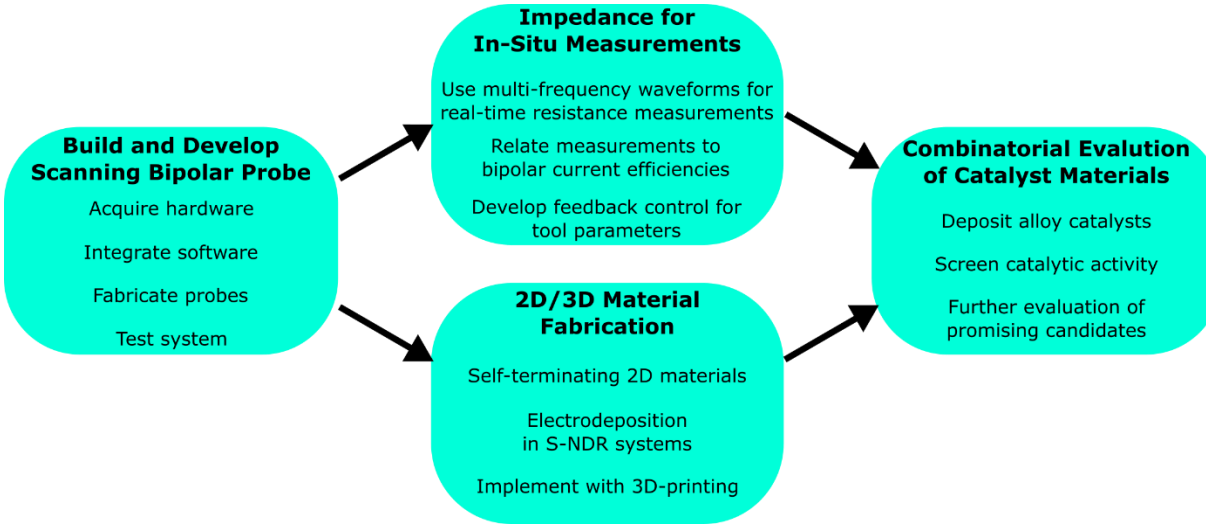

Figure 7.8 Flowchart demonstrating general methodology of the proposed research

7.4.2.1 Scanning Bipolar Impedance

The scanning bipolar probe will operate in a four-electrode setup as shown in Figure 7.9b. The current source electrodes (*A* and *B*) will be used to drive the desired chemistries at the substrate and will be located upstream of the microjet nozzle outlet (*A*) and situated in the far-field electrolyte (*B*). A potential sense electrode (*C*) will be patterned on the bottom of the microjet nozzle wall and will be electrically connected to a second electrode (*D*) also situated in the far-field electrolyte. Electrodes (*C*) and (*D*) measure the potential difference, but the potential at electrode (*D*) is essentially constant since potential gradients are negligible in the far-field electrolyte. In essence, these electrodes are measuring the surface potential of the substrate beneath the nozzle. It is important to note that the potential sense electrode patterned on the nozzle wall must be small with respect to the electrode surface being probed, otherwise significant bipolar electrochemistry can occur on the potential sense electrode, thus negating its function. This

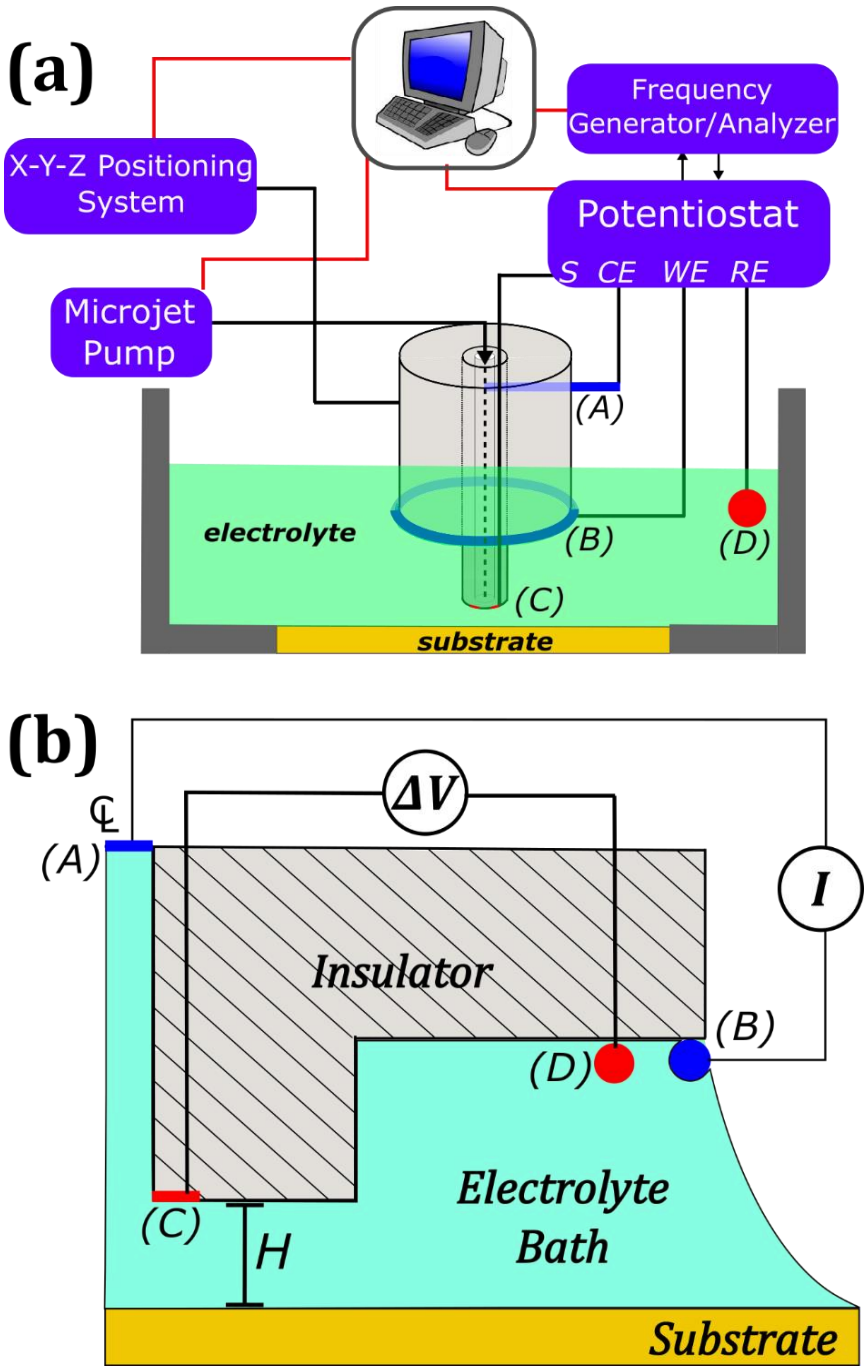

Figure 7.9 Schematic of SBP electrochemical impedance

Schematics of the key hardware and features of the scanning bipolar probe. **(a)** Block diagram of the scanning bipolar probe system. **(b)** Axisymmetric schematic detailing the locations of the four electrodes in the system.

problem is easily avoided by using a narrow width sense electrode, as the electric field necessary to drive bipolar reactions is inversely related to the electrode length[43].

The scanning bipolar probe will primarily use alternating current, local electrochemical impedance spectroscopy (LEIS) measurements for in-situ evaluation of local charge transfer resistance at the substrate and ohmic resistance beneath the microjet nozzle. This will provide real-time information about tool operation. One downside to bipolar electrochemical fabrication is that the ability to "count Coulombs" is lost when depositing materials since a fraction of the total applied current passes through the conductive substrate. However, in-situ charge transfer resistance and ohmic resistance measurements may enable bipolar current efficiencies to be calculated for a more accurate estimation of the amount of material deposited. In addition, real time measurement of the ohmic resistance allows for accurate control of the fly-height (the height at which the nozzle rests above the substrate) and knowledge thereof can provide information on the film thickness and material growth rate.

7.4.2.2 Fabrication of 2D/3D Materials

An emerging area in electrodeposition research is electrodeposition of materials in systems exhibiting non-monotonic voltammetric (i.e. potential-current) curves, particularly for catalytic applications. One example is self-terminated electrodeposition of 2D materials such as occurs during platinum or iridium deposition at high overpotentials, providing a technique for vertical control of deposit growth[121,122]. Lateral deposit growth can further be controlled by the scanning bipolar probe. Resolution of lateral deposition by local electrochemical methods is mostly determined by the nozzle dimensions and its fly-height above the substrate. Deposition of self-terminating materials with the scanning bipolar probe enables control of material deposition in both vertical and lateral directions.

Another form of non-monotonic voltammetric systems being studied is bottom-up fill copper deposition in through-silicon-vias (TSVs)[16]. In this mechanism, polyether adsorption on chloride surfaces suppresses copper growth. However, once copper deposition begins, polyether suppression is disrupted allowing for more rapid copper growth. This system is characterized by a bi-stable S-shaped negative differential resistance (S-NDR) system that leads to bifurcation of the surface into active and passive zones. This bifurcation can form Turing-like patterns on the surface supported by the difference in relaxation time between mass transport and the ohmic response of the system. Operation of the scanning bipolar probe requires that there are high ohmic resistances in order to drive more current through the substrate for electrochemistry to occur. Therefore, the scanning bipolar probe presents an ideal model system for exploring electrodeposition from suppressor derived S-NDR systems.

Recent years have seen a spike in research efforts using 3D-printing for additive manufacturing. Driving this surge is the availability of easy-to-use integrated software/hardware platforms that can translate an abstract computer file into a fabricated object. The most common commercially available low temperature, table-top additive manufacturing technologies are excellent at fabrication of polymeric materials, but are not typically capable of metal deposition. That said, local electrodeposition methods have been used for freeform fabrication of metal objects, but haven't made the jump to commercial viability, largely due to limitations in automation and software. The combination of real-time feedback from impedance measurements and non-contact electrodeposition features of the scanning bipolar probe can provide a platform ideal for implementation with current 3D-printing software and technologies. Collaboration with current 3D-printing research efforts will be done to develop a system that can build 3D objects consisting of polymers, ceramics, metals as well as composites thereof. The ability to easily form

such materials in a wide range of architectures is sure to find application in a range of technologies from sensor to microscale integrated circuit fabrication.

7.4.2.3 Combinatorial Screening of Catalyst Materials

The true novelty in this research proposal is the combination of a material fabrication tool with an electrochemical analytical probe. In the final segment of the research project, this aspect will be utilized for combinatorial fabrication and evaluation of electrocatalytic materials relevant to emerging energy conversion technologies. Recently, electrodeposition research has made a concerted effort to develop new catalyst materials for use in fuel cell energy conversion[123,124]. The motivation for this research stems from the high cost of current platinum catalysts. These research efforts have demonstrated that reducing the amount of platinum loading by alloying with transition metals can reduce material costs and also improve catalytic activity. The scanning bipolar probe can easily control material composition by varying electrolyte flow rates and applied currents, to deposit Pt-transition metal bi/tri-alloys of varying composition on a single substrate. Then, the scanning bipolar probe will evaluate catalytic activity by mapping the charge transfer resistance for oxygen reduction and water splitting reactions. Additional metrology equipment will also be vital for further evaluation of promising material candidates. Imaging x-ray photoelectron spectroscopy (XPS) will determine the thin film composition, allowing for correlation between scanning bipolar probe operating conditions and the alloy composition. Scanning electron microscopy (SEM) and atomic force microscopy (AFM) will provide information on catalyst structure and morphology.

7.4.3 *New Measurement Techniques*

Electrochemical impedance spectroscopy is a powerful technique for characterizing the transient and steady-state behavior of electrochemical systems. More recently, scanning electrochemical microscopy systems have employed electrochemical impedance spectroscopy (AC-SECM) to provide an element of spatial definition to the electrical measurement[125]. The scanning bipolar probe will operate in a similar manner, but with the diffusion resistance minimized by jetted electrolyte flow. The high mass-transfer rates in the scanning bipolar probe enable a straightforward measurement of the local heterogeneous charge transfer resistance. In the absence of a mass transport constraint the equivalent circuit (Figure 7.10a) for the scanning bipolar probe consists of just two resistances of interest: the ohmic resistance (R_{ohm}) and heterogeneous charge transfer resistance (R_{CT}), producing a Nyquist plot as shown in Figure 7.10b. Real-time measurements of the two resistances, R_{ohm} and R_{CT}, can be done by multiple frequency sinewave perturbation: high frequency oscillations for probing the ohmic resistance and low frequency oscillations for probing the charge transfer resistance. Recent studies have demonstrated the ability to probe systems with several waveforms, minimizing the time necessary to create full impedance spectroscopic data[126]. This method will allow for dynamic measurement of bipolar current efficiencies, enabling greater control of material fabrication and understanding of the electrochemical process.

7.4.4 *Significance and Application*

Development of the scanning bipolar probe fabrication and analytical capabilities will provide a platform for future research that extends well beyond the scope of the present proposal. For example, in some battery materials the contact resistance can be the same order of magnitude

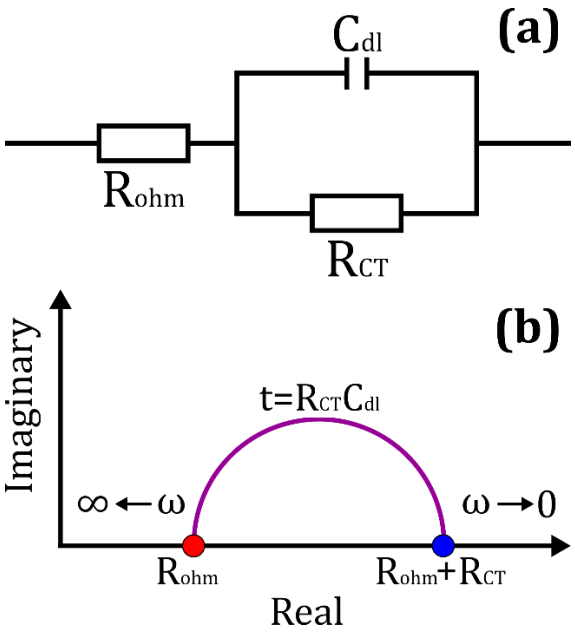

Figure 7.10 Equivalent Circuit and Nyquist Plot

Impedance equivalent circuit and contributions to the Nyquist plot. **(a)** The equivalent circuit consists of an ohmic resistance (R_{ohm}) and a charge transfer resistance (R_{CT}) in parallel with the double layer capacitance (C_{dl}). **(b)** The corresponding Nyquist plot for the equivalent circuit in (a).

as the charge transfer resistance, influencing measurements and requiring significant deconvolution to reveal the true reaction kinetics[127]. LEIS probing in a bipolar manner can provide a more direct assessment of localized reaction kinetics as there is no need for direct electrical connections to the material of interest. The method will also enable rapid exploration of the spatial nonuniformities in battery electrode materials. Furthermore, the scanning bipolar probe can also be utilized for traditional SECM-style measurements performed sequentially, or in parallel with the LEIS.

The proposed research will develop a new class of scanning probe technology and measurement. Implementation of LEIS enables real-time feedback on critical information such as charge transfer and ohmic resistances. In addition, operating with high mass-transfer, and with no

electrical connections to the substrate during bipolar operation, provides a more fundamental measurement of heterogeneous reaction kinetics than current EIS measurement techniques. The combination of material fabrication and real-time electroanalytics also enables rapid combinatorial evaluation of electrocatalysts for many electrochemical applications.

BIBLIOGRAPHY

1 Burleigh, J. C. & Garcia, T. D. The beginnings of gold electroplating. *Electrochemical Society Interface* **22**, 36-38 (2013).

2 Paunovic, M. *Fundamentals of electrochemical deposition*. 2nd ed. edn, (Hoboken, N.J. : Wiley-Interscience, 2006).

3 Tobias, C. W., Eisenberg, M. & Wilke, C. R. Difusion and convection in electrolysis - a theoretical review. *Journal of the Electrochemical Society* **99**, C359-C365, doi:10.1149/1.2779636 (1952).

4 Schlesinger, M. *Modern electroplating*. (Wiley, 2010).

5 Levich, B. Theory of concentration polarization II. *Acta Physicochimica Urss* **19**, 117-132 (1944).

6 Levich, B. The theory of concentration polarization. *Acta Physicochimica Urss* **17**, 257-307 (1942).

7 Koutetsky, J. & Levich, B. G. The use of a rotating disc electrode for studying kinetic and catalytic processes in electrochemistry. *Doklady Akademii Nauk Sssr* **117**, 441-444 (1957).

8 Madden, J. D. & Hunter, I. W. Three-dimensional microfabrication by localized electrochemical deposition. *Journal of Microelectromechanical Systems* **5**, 24-32, doi:10.1109/84.485212 (1996).

9 Chen, Q., Wang, Z., Cai, J. & Liu, L. The influence of ultrasonic agitation on copper electroplating of blind-vias for SOI three-dimensional integration. *Microelectronic Engineering* **87**, 527-531, doi:10.1016/j.mee.2009.06.035 (2010).

10 Nichols, R. J., Beckmann, W., Meyer, H., Batina, N. & Kolb, D. M. An insitu scanning tunneling microscopy study of bulk copper deposition and the influence of an organic additive. *Journal of Electroanalytical Chemistry* **330**, 381-394, doi:10.1016/0022-0728(92)80319-y (1992).

11 McCrea, J. L., Palumbo, G., Hibbard, G. D. & Erb, U. Properties and applications for electrodeposited nanocrystalline Fe-Ni alloys. *Reviews on Advanced Materials Science* **5**, 252-258 (2003).

12 Nickchi, T. & Ghorbani, M. Pulsed electrodeposition and characterization of bronze-graphite composite coatings. *Surface & Coatings Technology* **203**, 3037-3043, doi:10.1016/j.surfcoat.2009.03.029 (2009).

13 *Anti-corrosion coating market by type - Global trends and forecasts to 2019*, 2015).

14 Andricacos, P. C., Uzoh, C., Dukovic, J. O., Horkans, J. & Deligianni, H. Damascene copper electroplating for chip interconnections. *Ibm Journal of Research and Development* **42**, 567-574 (1998).

15 Vereecken, P. M., Binstead, R. A., Deligianni, H. & Andricacos, P. C. The chemistry of additives in damascene copper plating. *Ibm Journal of Research and Development* **49**, 3-18 (2005).

16 Moffat, T. P. & Josell, D. Extreme Bottom-Up Superfilling of Through-Silicon-Vias by Damascene Processing: Suppressor Disruption, Positive Feedback and Turing Patterns. *Journal of the Electrochemical Society* **159**, D208-D216, doi:10.1149/2.040204jes (2012).

17 Vaezi, M., Seitz, H. & Yang, S. A review on 3D micro-additive manufacturing technologies. *International Journal of Advanced Manufacturing Technology* **67**, 1721-1754, doi:10.1007/s00170-012-4605-2 (2013).
18 Cohen, A. L. Method for electrochemical fabrication. (2000).
19 Mandler, D. & Bard, A. Hole injection and etching studies of GaAs using the scanning electrochemical microscope. *Langmuir* **6**, 1489-1494, doi:10.1021/la00099a010 (1990).
20 McCarley, R., Hendricks, S. & Bard, A. Controlled nanofabrication of higly oriented pyrolytic-graphite with the scanning tunneling microscope. *Journal of Physical Chemistry* **96**, 10089-10092, doi:10.1021/j100204a002 (1992).
21 Wuu, Y., Fan, F. & Bard, A. High-resolution deposition of polyaniline on Pt with the scanning electrochemical microscope. *Journal of the Electrochemical Society* **136**, 885-886, doi:10.1149/1.2096765 (1989).
22 Macpherson, J., Marcar, S. & Unwin, P. Microjet electrode - a hydrodynamic ultramicroelectrode with high mass-transfer rates. *Analytical Chemistry* **66**, 2175-2179, doi:10.1021/ac00085a037 (1994).
23 Gelchinski, M. H., Romankiw, L. T., Vigliotti, D. R. & VON Gutfeld, R. J. Laser-enhanced jet-plating and jet-etching: high-speed maskless patterning method. (1985).
24 Vongutfeld, R., Gelchinski, M., Romankiw, L. & Vigliotti, D. Laser-enhanced jet plating - a method of high-speed maskless patterning. *Applied Physics Letters* **43**, 876-878, doi:10.1063/1.94534 (1983).
25 Vongutfeld, R., Acosta, R. & Romankiw, L. Laser-enhanced plating and etching - mechanisms and applications. *Ibm Journal of Research and Development* **26**, 136-144 (1982).
26 Nelson, J. B. & Schwartz, D. T. Electrochemical factors controlling the patterning of metals on SAM-coated substrates. *Langmuir* **23**, 9661-9666, doi:10.1021/1a701014u (2007).
27 Nelson, J. B. & Schwartz, D. T. Electrochemical printing: in situ characterization using an electrochemical quartz crystal microbalance. *Journal of Micromechanics and Microengineering* **15**, 2479-2484, doi:10.1088/0960-1317/15/12/033 (2005).
28 Nelson, J. B., Wisecarver, Z. & Schwartz, D. T. Electrochemical printing: mass transfer effects. *Journal of Micromechanics and Microengineering* **17**, 1192-1199, doi:10.1088/0960-1317/17/6/013 (2007).
29 Whitaker, J. D., Nelson, J. B. & Schwartz, D. T. Electrochemical printing: software reconfigurable electrochemical microfabrication. *Journal of Micromechanics and Microengineering* **15**, 1498-1503, doi:10.1088/0960-1317/15/8/017 (2005).
30 Nelson, J. B. & Schwartz, D. T. Characterization of buffered electrolytes for nickel electrochemical printing. *Journal of the Electrochemical Society* **155**, D181-D186, doi:10.1149/1.2825166 (2008).
31 Nelson, J. B. *Electrochemical printing : design, characterization, and translation*, (2007).
32 Whitaker, J. D. *Electrochemical printing*, (2003).
33 Bradley, J. C. *et al.* Creating electrical contacts between metal particles using directed electrochemical growth. *Nature* **389**, 268-271, doi:10.1038/38464 (1997).
34 Bradley, J. C., Ma, Z. M., Clark, E., Crawford, J. & Stephens, S. G. Programmable ward-wiring of circuitry using spatially coupled bipolar electrochemistry. *Journal of the Electrochemical Society* **146**, 194-198, doi:10.1149/1.1391586 (1999).

35 Chow, K. F., Mavre, F., Crooks, J. A., Chang, B. Y. & Crooks, R. M. A Large-Scale, Wireless Electrochemical Bipolar Electrode Microarray. *Journal of the American Chemical Society* **131**, 8364-+, doi:10.1021/ja902683f (2009).

36 Chow, K.-F., Chang, B.-Y., Zaccheo, B. A., Mavre, F. & Crooks, R. M. A Sensing Platform Based on Electrodissolution of a Ag Bipolar Electrode. *Journal of the American Chemical Society* **132**, 9228-9229, doi:10.1021/ja103715u (2010).

37 Fosdick, S. E. & Crooks, R. M. Bipolar Electrodes for Rapid Screening of Electrocatalysts. *Journal of the American Chemical Society* **134**, 863-866, doi:10.1021/ja210354m (2012).

38 Tisserant, G. *et al.* (Elsevier, Electrochimica Acta, 2015).

39 Fosdick, S. E., Knust, K. N., Scida, K. & Crooks, R. M. Bipolar Electrochemistry. *Angewandte Chemie-International Edition* **52**, 10438-10456, doi:10.1002/anie.201300947 (2013).

40 Ishiguro, Y., Inagi, S. & Fuchigami, T. Gradient Doping of Conducting Polymer Films by Means of Bipolar Electrochemistry. *Langmuir* **27**, 7158-7162, doi:10.1021/la200464t (2011).

41 Munktell, S., Nyholm, L. & Bjorefors, F. Towards high throughput corrosion screening using arrays of bipolar electrodes. *Journal of Electroanalytical Chemistry* **747**, 77-82, doi:10.1016/j.jelechem.2015.04.008 (2015).

42 Ulrich, C., Andersson, O., Nyholm, L. & Bjorefors, F. Formation of molecular gradients on bipolar electrodes. *Angewandte Chemie-International Edition* **47**, 3034-3036, doi:10.1002/anie.200705824 (2008).

43 Loget, G., Zigah, D., Bouffier, L., Sojic, N. & Kuhn, A. Bipolar Electrochemistry: From Materials Science to Motion and Beyond. *Accounts of Chemical Research* **46**, 2513-2523, doi:10.1021/ar400039k (2013).

44 Braun, T. M. & Schwartz, D. T. Localized Electrodeposition and Patterning Using Bipolar Electrochemistry. *Journal of the Electrochemical Society* **162**, D180-D185, doi:10.1149/2.1031504jes (2015).

45 Braun, T. M. & Schwartz, D. T. Bipolar Electrochemical Displacement: A New Phenomenon with Implications for Self-Limiting Materials Patterning. *Chemelectrochem* **3**, 441-449, doi:10.1002/celc.201500356 (2016).

46 Wood, M. & Zhang, B. Bipolar Electrochemical Method for Dynamic In Situ Control of Single Metal Nanowire Growth. *Acs Nano* **9**, 2454-2464, doi:10.1021/acsnano.5b00139 (2015).

47 Oleinick, A., Battistel, D., Daniele, S., Svir, I. & Amatore, C. Simple and Clear Evidence for Positive Feedback Limitation by Bipolar Behavior during Scanning Electrochemical Microscopy of Unbiased Conductors. *Analytical Chemistry* **83**, 4887-4893, doi:10.1021/ac2006075 (2011).

48 Qian, P. *et al.* A novel electrode-bipolar plate assembly for vanadium redox flow battery applications. *Journal of Power Sources* **175**, 613-620, doi:10.1016/j.jpowsour.2007.09.006 (2008).

49 Tang, A., McCann, J., Bao, J. & Skyllas-Kazacos, M. Investigation of the effect of shunt current on battery efficiency and stack temperature in vanadium redox flow battery. *Journal of Power Sources* **242**, 349-356, doi:10.1016/j.jpowsour.2013.05.079 (2013).

50 Ramakrishnan, S. & Shannon, C. Display of Solid-State Materials Using Bipolar Electrochemistry. *Langmuir* **26**, 4602-4606, doi:10.1021/la100292u (2010).

51 Kuwahara, T., Sato, K., Kondo, M. & Shimomura, M. Targeted deposition of a conducting polymer based on bipolar electrochemistry. *Synthetic Metals* **198**, 274-276, doi:10.1016/j.synthmet.2014.10.045 (2014).

52 Loget, G., Roche, J. & Kuhn, A. True Bulk Synthesis of Janus Objects by Bipolar Electrochemistry. *Advanced Materials* **24**, 5111-5116, doi:10.1002/adma.201201623 (2012).

53 Loget, G. & Kuhn, A. Propulsion of Microobjects by Dynamic Bipolar Self-Regeneration. *Journal of the American Chemical Society* **132**, 15918-15919, doi:10.1021/ja107644x (2010).

54 Zuccaro, L. *et al.* Selective Functionalization of Graphene Peripheries by using Bipolar Electrochemistry. *Chemelectrochem* **3**, 372-377, doi:10.1002/celc.201500461 (2016).

55 Raj, B., Mudali, U. K. & Rangarajan, S. *Corrosion prevention and control*. (Oxford, U.K. : Alpha Science International, 2009).

56 Szklarska-Smialowska, Z. *Pitting corrosion of metals*. (Houston, Tex. : National Association of Corrosion Engineers, 1986).

57 Naval Civil Engineering, L. *Forms of corrosion III : pitting*. (Port Hueneme, Calif. : Dept. of the Navy, Naval Civil Engineering Laboratory, 1985).

58 Wranglén, G. *An introduction to corrosion and protection of metals*. (Chapman and Hall, 1985).

59 Lipson, C. *Handbook of mechanical wear: wear, frettage, pitting, cavitation, corrosion*. (Ann Arbor, University of Michigan Press, 1961).

60 Streicher, M. A. Pitting corrosion of 18Cr-8Ni stainless steel. *Journal of the Electrochemical Society* **103**, 375-390, doi:10.1149/1.2430359 (1956).

61 Rosenfel.Il & Danilov, I. S. Electrochemical aspects of pitting corrosion. *Corrosion Science* **7**, 129-&, doi:10.1016/s0010-938x(67)80073-8 (1967).

62 Frankenthal, R. & Pickering, H. Mechanism of localized corrosion of iron and stainless-steel. 2. Morphological studies. *Journal of the Electrochemical Society* **119**, 1304-&, doi:10.1149/1.2403983 (1972).

63 Pickering, H. & Frankenthal, R. Mechanism of localized corrosion of iron and stainless-steel. 1. Electrochemical studies. *Journal of the Electrochemical Society* **119**, 1297-&, doi:10.1149/1.2403982 (1972).

64 Brigham, R. J. & Tozer, E. W. Temperature as a pitting criterion. *Corrosion* **29**, 33-36 (1973).

65 Galvele, J. R. Transport processes in passivity breakdown. 2.Full hydrolysis of metal-ions. *Corrosion Science* **21**, 551-579, doi:10.1016/0010-938x(81)90009-3 (1981).

66 Wagner, C. & Traud, W. E. The analysis of corrosion procedures through the interaction of electrochemical partial procedures and on the potential difference of mixed electrodes. *Zeitschrift Fur Elektrochemie Und Angewandte Physikalische Chemie* **44**, 391-402 (1938).

67 Zadorozne, N. S., Giordano, C. M., Rodriguez, M. A., Carranza, R. M. & Rebak, R. B. Crevice corrosion kinetics of nickel alloys bearing chromium and molybdenum. *Electrochimica Acta* **76**, 94-101, doi:10.1016/j.electacta.2012.04.157 (2012).

68 Edeleanu, C. & Evans, U. R. The causes of the localized character of corrosion on aluminium. *Transactions of the Faraday Society* **47**, 1121-1135, doi:10.1039/tf9514701121 (1951).

69 Pickering, H. W. Important early developments and current understanding of the IR mechanism of localized corrosion. *Journal of the Electrochemical Society* **150**, K1-K13, doi:10.1149/1.1565142 (2003).
70 Abdulsalam, M. I. & Pickering, H. W. Effect of the applied potential on the potential and current distributions within crevices in pure nickel. *Corrosion Science* **41**, 351-372 (1999).
71 Al-Zahrania, A. M. & Pickering, H. W. IR voltage switch in delayed crevice corrosion and active peak formation detected using a repassivation-type scan. *Electrochimica Acta* **50**, 3420-3435, doi:10.1016/j.electatata.2004.12.017 (2005).
72 Cho, K. & Pickering, H. W. The role of chloride-ions in the IR greater-than IR-star criterion for crevice corrosion in iron. *Journal of the Electrochemical Society* **138**, L56-L58, doi:10.1149/1.2085386 (1991).
73 Pickering, H. W. IR voltage in crevices during crevice corrosion and sacrificial cathodic protection. *Zeitschrift Fur Physikalische Chemie-International Journal of Research in Physical Chemistry & Chemical Physics* **221**, 1441-1454, doi:10.1524/zpch.2007.221.11 (2007).
74 Pickering, H. W. On the roles of corrosion products in local cell processes. *Corrosion* **42**, 125-140 (1986).
75 Mattsson, E. & Bockris, J. Galvanostatic studies of the kinetics of depostion and dissolution in the copper + copper sulphate system. *Transactions of the Faraday Society* **55**, 1586-1601, doi:10.1039/tf9595501586 (1959).
76 White, R. & Newman, J. Simultaneous reactions on a rotating-disk electrode. *Journal of the Electrochemical Society* **124**, C127-C127 (1977).
77 Schwartz, D. T. & Whitaker, J. D. (Google Patents, 2009).
78 Tanaka, N. & Tamamushi, R. Kinetic parameters of electrode reactions. *Electrochimica Acta* **9**, 963-989, doi:http://dx.doi.org/10.1016/0013-4686(64)85045-3 (1964).
79 Bard, A., Fan, F., Kwak, J. & Lev, O. Scanning electrochemical microscopy - introduction and principles. *Analytical Chemistry* **61**, 132-138, doi:10.1021/ac00177a011 (1989).
80 Amemiya, S., Bard, A. J., Fan, F. R. F., Mirkin, M. V. & Unwin, P. R. in *Annual Review of Analytical Chemistry* Vol. 1 *Annual Review of Analytical Chemistry* 95-131 (Annual Reviews, 2008).
81 Malel, E. & Mandler, D. Localized electroless deposition of gold nanoparticles using scanning electrochemical microscopy. *Journal of the Electrochemical Society* **155**, D459-D467, doi:10.1149/1.2902331 (2008).
82 Yatziv, Y., Turyan, I. & Mandler, D. A new approach to micropatterning: Application of potential-assisted ion transfer at the liquid-liquid interface for the local metal deposition. *Journal of the American Chemical Society* **124**, 5618-5619, doi:10.1021/ja0257826 (2002).
83 Bard, A. J. & Mirkin, M. V. *Scanning electrochemical microscopy*. 2nd ed. edn, (Boca Raton, Fla. : CRC Press, 2012).
84 Mirkin, M. V. & Amemiya, S. *Nanoelectrochemistry*. (Boca Raton : CRC Press, Taylor & Francis Group, 2015).
85 Newman, J. S. *Electrochemical systems*. 3rd ed. edn, (Hoboken, N.J. : J. Wiley, 2004).

86 Roy, P. R., Saha, M. S., Okajima, T. & Ohsaka, T. Electrooxidation and amperometric detection of ascorbic acid at GC electrode modified by electropolymerization of N,N-dimethylaniline. *Electroanalysis* **16**, 289-297, doi:10.1002/elan.200402838 (2004).

87 Borsook, H., Davenport, H., Jeffreys, C. & Warner, R. The oxidation of ascorbic acid and its reduction in vitro and in vivo. *Journal of Biological Chemistry* **117**, 237-279 (1937).

88 Sies, H., Stahl, W. & Sundquist, A. R. Antioxidant functions of vitamins: Vitamins E and C, beta-carotene, and other carotenoids. *Annals of the New York Academy of Sciences; Beyond deficiency: New views on the function and health effects of vitamins* **669**, 7-20 (1992).

89 Padayatty, S. J. *et al.* Vitamin C as an antioxidant: Evaluation of its role in disease prevention. *Journal of the American College of Nutrition* **22**, 18-35 (2003).

90 Liu, M. *et al.* A stable sandwich-type amperometric biosensor based on poly(3,4-ethylenedioxythiophene)-single walled carbon nanotubes/ascorbate oxidase/nafion films for detection of L-ascorbic acid. *Sensors and Actuators B-Chemical* **159**, 277-285, doi:10.1016/j.snb.2011.07.005 (2011).

91 Fang, Y. *et al.* Preparation in-situ of carbon nanotubes/polyaniline modified electrode and application for ascorbic acid detection. *Journal of Electroanalytical Chemistry* **755**, 39-46, doi:10.1016/j.jelechem.2015.07.039 (2015).

92 Zhang, M. N., Gong, K. P., Zhang, H. W. & Mao, L. Q. Layer-by-layer assembled carbon nanotubes for selective determination of dopamine in the presence of ascorbic acid. *Biosensors & Bioelectronics* **20**, 1270-1276, doi:10.1016/j.bios.2004.04.018 (2005).

93 Zhao, Y. F. *et al.* Selective detection of dopamine in the presence of ascorbic acid and uric acid by a carbon nanotubes-ionic liquid gel modified electrode. *Talanta* **66**, 51-57, doi:10.1016/j.talanta.2004.09.019 (2005).

94 Park, H. W. *et al.* Optical ascorbic acid sensor based on the fluorescence quenching of silver nanoparticles. *Luminescence* **24**, 367-371, doi:10.1002/bio.1119 (2009).

95 Yang, Y., Xia, Y., Huang, W., Zheng, J. & Li, Z. Fabrication of nano-network gold films via anodization of gold electrode and their application in SERS. *Journal of Solid State Electrochemistry* **16**, 1733-1739, doi:10.1007/s10008-011-1600-8 (2012).

96 Holade, Y., Napporn, T. W., Morais, C., Servat, K. & Kokoh, K. B. Probing Structure Modification of Palladium Nanomaterials during Chemical Synthesis by using In Situ X-ray Diffraction: Electrochemical Properties. *Chemelectrochem* **2**, 592-599, doi:10.1002/celc.201402353 (2015).

97 Lutz, B. R., Chen, J. & Schwartz, D. T. Characterizing homogeneous chemistry using well-mixed microeddies. *Analytical Chemistry* **78**, 1606-1612, doi:10.1021/ac051646i (2006).

98 Pisoschi, A., Pop, A., Serban, A. & Fafaneata, C. Electrochemical methods for ascorbic acid determination. *Electrochimica Acta* **121**, 443-460, doi:10.1016/j.electacta.2013.12.127 (2014).

99 Erdurak-Kilic, C. S. *et al.* Anodic voltammetric behavior of ascorbic acid and its selective determination in pharmaceutical dosage forms and some Rosa species of Turkey. *Journal of Analytical Chemistry* **61**, 1113-1120, doi:10.1134/s106193480611013x (2006).

100 Karabinas, P. & Jannakoudakis, D. Kinetic parameters and mechanism of the electrochemical oxidation of L-ascorbic acid on platinum electrodes in acid solutions.

Journal of Electroanalytical Chemistry **160**, 159-167, doi:10.1016/s0022-0728(84)80122-9 (1984).

101 Brezina, M., Loucka, T., Koryta, J., Marsikov, D. & Pradac, J. Adsoprtion and kinetics of oxidation of ascorbic-acid at platinum electrodes. *Journal of Electroanalytical Chemistry* **40**, 13-&, doi:10.1016/0368-1874(72)80226-0 (1972).

102 Ruiz, J., Aldaz, A. & Dominguez, M. Mechanism of L-ascorbic acid oxidation on a mercury electrode. 2. Basic medium. *Canadian Journal of Chemistry-Revue Canadienne De Chimie* **56**, 1533-1537, doi:10.1139/v78-248 (1978).

103 Perone, S. & Kretlow, W. Application of controlled potential techniques to study of rapid succeeding chemical reaction coupled to electro-oxidation of ascorbic acid. *Analytical Chemistry* **38**, 1760-&, doi:10.1021/ac60244a034 (1966).

104 Zhao, Y. *et al.* Electrocatalytic oxidation of ascorbic acid on a lithium-doped tantalum oxide film coated electrode. *Electrochimica Acta* **107**, 52-58, doi:10.1016/j.electacta.2013.06.007 (2013).

105 Sanchis, C., Ghanem, M. A., Salavagione, H. J., Morallon, E. & Bartlett, P. N. The oxidation of ascorbate at copolymeric sulfonated poly(aniline) coated on glassy carbon electrodes. *Bioelectrochemistry* **80**, 105-113, doi:10.1016/j.bioelechem.2010.06.006 (2011).

106 Rueda, M., Aldaz, A. & Sanchez-Burgos, F. Oxidation of L-ascorbic acid on a gold electrode. *Electrochimica Acta* **23**, 419-424, doi:10.1016/0013-4686(78)87040-6 (1978).

107 Braun, T. M. & Schwartz, D. T. Remote Control Electrodeposition: Principles for Bipolar Patterning of Substrates without an Electrical Connection. *Journal of The Electrochemical Society* **163**, D3014-D3019, doi:10.1149/2.0031612jes (2016).

108 Newman, J. RESISTANCE FOR FLOW OF CURRENT TO A DISK. *Journal of the Electrochemical Society* **113**, 501-&, doi:10.1149/1.2424003 (1966).

109 Wong, K. V. & Hernandez, A. A Review of Additive Manufacturing. *ISRN Mechanical Engineering* **2012**, 10, doi:10.5402/2012/208760 (2012).

110 Huang, S., Liu, P., Mokasdar, A. & Hou, L. Additive manufacturing and its societal impact: a literature review. *International Journal of Advanced Manufacturing Technology* **67**, 1191-1203, doi:10.1007/s00170-012-4558-5 (2013).

111 Hull, C. W. Apparatus for production of three-dimensional objects by stereolithography. (1986).

112 Bertsch, A., Jiguet, S. & Renaud, P. Microfabrication of ceramic components by microstereolithography. *Journal of Micromechanics and Microengineering* **14**, 197-203, doi:10.1088/0960-1317/14/2/005 (2004).

113 Kawata, S., Sun, H. B., Tanaka, T. & Takada, K. Finer features for functional microdevices - Micromachines can be created with higher resolution using two-photon absorption. *Nature* **412**, 697-698, doi:10.1038/35089130 (2001).

114 Deckard, C. R. Method and apparatus for producing parts by selective sintering. (1989).

115 Sachs, E., Cima, M., Williams, P., Brancazio, D. & Cornie, J. 3-Dimensional printing - Rapid tooling and prototypes directly from a CAD model. *Journal of Engineering For Industry-Transactions of the Asme* **114**, 481-488 (1992).

116 Wang, W., Holl, M. & Schwartz, D. Rapid prototyping of masks for through-mask electrodeposition of thick metallic components. *Journal of the Electrochemical Society* **148**, C363-C368, doi:10.1149/1.1360187 (2001).

117 Leith, S. D. & Schwartz, D. T. High-rate through-mold electrodeposition of thick (> 200 mu m) NiFe MEMS components with uniform composition. *Journal of Microelectromechanical Systems* **8**, 384-392, doi:10.1109/84.809052 (1999).
118 Leith, S. D. & Schwartz, D. T. In-situ fabrication of sacrificial layers in electrodeposited NiFe microstructures. *Journal of Micromechanics and Microengineering* **9**, 97-104, doi:10.1088/0960-1317/9/1/313 (1999).
119 Alper, S. E., Ocak, I. E. & Akin, T. - Ultrathick and High-Aspect-Ratio Nickel Microgyroscope Using EFAB Multilayer Additive Electroforming. **- 16**, - 1035 (2007).
120 Kranz, C. Recent advancements in nanoelectrodes and nanopipettes used in combined scanning electrochemical microscopy techniques. *Analyst* **139**, 336-352, doi:10.1039/c3an01651j (2014).
121 Sang Hyun, A. *et al.* Self-terminated electrodeposition of iridium electrocatalysts. *Energy & Environmental Science* **8**, 3557-3562, doi:10.1039/c5ee02541a (2015).
122 Liu, Y., Gokcen, D., Bertocci, U. & Moffat, T. P. Self-Terminating Growth of Platinum Films by Electrochemical Deposition. *Science* **338**, 1327-1330, doi:10.1126/science.1228925 (2012).
123 Hangarter, C. M., Liu, Y., Pagonis, D., Bertocci, U. & Moffat, T. P. Electrodeposition of Ternary Pt100-x-yCoxNiy Alloys. *Journal of the Electrochemical Society* **161**, D31-D43, doi:10.1149/2.022401jes (2014).
124 Liu, Y., Hangarter, C. M., Bertocci, U. & Moffat, T. P. Oxygen Reduction Reaction on Electrodeposited Pt100-xNix: Influence of Alloy Composition and Dealloying. *Journal of Physical Chemistry C* **116**, 7848-7862, doi:10.1021/jp300672h (2012).
125 Eckhard, K. & Schuhmann, W. Alternating current techniques in scanning electrochemical microscopy (AC- SECM). *The Analyst* **133**, 1486, doi:10.1039/b806721j (2008).
126 Breugelmans, T. *et al.* Odd random phase multisine EIS for organic coating analysis. *Progress in Organic Coatings* **69**, 215-218, doi:10.1016/j.porgcoat.2010.04.008 (2010).
127 Illig, J. *et al.* Separation of Charge Transfer and Contact Resistance in LiFePO4-Cathodes by Impedance Modeling. *Journal of The Electrochemical Society* **159**, A952-A960, doi:10.1149/2.030207jes (2012).

VITA

Trevor Braun

University of Washington 105 Benson Hall
Box 351750 Seattle, WA 98195-1750
tbraun@uw.edu | 623-670-1897

EDUCATION

June 2016 **Ph.D., Chemical Engineering**
University of Washington, Seattle, WA
GPA: 3.83
Dissertation: "Remote Control Electrodeposition: Patterning on Substrates without Direct Electrical Connections
Advisor: Dr. Daniel T. Schwartz

May 2011 **B.S., Chemical Engineering**
Colorado School of Mines, Golden, CO
GPA: 3.75 (Magna cum Laude)

PROFESSIONAL EXPERIENCE

2011-Present **Ph.D. Thesis Research**
University of Washington, Seattle, WA
Research Focus: Electrochemistry with a focus on bipolar electrodeposition including electrolyte design and characterization
Advisor: Dr. Daniel T. Schwartz

June-Sept. 2013 **Internship**
Lam Research, Tualatin, OR
Work Focus: Through silicon via (TSV) process optimization and customer product development.
Managers: Joe Richardson and Haiying Fu

2009-2010 **Undergraduate Research**
Colorado School of Mines, Golden, CO
Research Focus: Methane clathrate hydrate pipeline dissociation and CO_2 hydrate sequestration
Advisors: E. Dendy Sloan, Amadeu K. Sum, and Carolyn A. Koh

PUBLICATIONS & PRESENTATIONS

Articles

1. **T.M. Braun**, D.T. Schwartz. "Localized Electrodeposition and Patterning Using Bipolar Electrochemistry". *Journal of The Electrochemical Society*, vol 162 (4), D180-185 (2015)
2. **T.M. Braun**, D.T. Schwartz. "Bipolar Electrochemical Displacement: A New Phenomenon with Implications for Self-Limiting Materials Patterning". *ChemElectroChem*, vol 3 (3), 441-449 (2015)
3. **T.M. Braun**, D.T. Schwartz. "Remote Control Electrodeposition: Principles for Bipolar Patterning of Substrates without an Electrical Connection". *Journal of the Electrochemical Society*, vol 163 (12), D3014-3019 (2016).
4. **T.M. Braun,** D.T. Schwartz. "The Emerging Role of Electrodeposition in Additive Manufacturing". *Electrochemical Society Interface*, vol 25 (1), 69-73 (2016).

Patents

1. **T.M. Braun**, D.T. Schwartz, "Bipolar Electrochemical Printing". (patent applied for, U.S. Serial No. 14/666,554) (2014)

Oral Presentations

1. "Localized Electrochemistry using the Scanning Bipolar Cell", The 8th International Workshop on Scanning Electrochemical Microscopy, Xiamen, China (October 2015)
2. "Electrodeposition by Remote Control: The Scanning Bipolar Cell", University of Washington Chemical Engineering 7th Annual Graduate Student Symposium, Seattle, WA (September 2014)
3. "Electrodeposition by Remote Control: The Scanning Bipolar Cell", The Gordon Research Conference for Electrodeposition, Biddeford, ME (July 2014) (Awarded Talk)
4. "Contactless Electrodeposition and Micropatterning via Bipolar Electrochemical Printing", the 224th Electrochemical Society Meeting, San Francisco, CA (October 2013)

Poster Presentations

1. "Theory and Experiments for Metal Patterning with the Scanning Bipolar Cell", the 228th Electrochemical Society Meeting, Phoenix, AZ (October 2015) (1st Place for Best Poster)
2. "Electrodeposition by Remote Control: The Scanning Bipolar Cell", the Gordon Research Conference for Electrodeposition, Biddeford, ME (July 2014)
3. "Microscale Repair of Semiconductor Testboards", the Washington Clean Technology Alliance Cleantech Showcase, Seattle, WA (June 2014)
4. "Combinatorial Alloy Screening of New Plated Coatings Using Electrochemical Printing (EcP)", the Gordon Research Conference and Seminar for Electrodeposition, Biddeford, ME (July 2012)

TEACHING EXPERIENCE

Fall 2013-Spring 2014 **Mentor for Special Senior Design**, University of Washington
Course: CHEME497 Special Projects in Chemical Engineering Design

- Undergraduate elective senior course using chemical engineering research projects to design entrepreneurial businesses or products for industrial market applications. Direct mentor for 3 students with 16 total students in the course.
- Prepared lectures, mentored students in lab research, organized group meetings, evaluated coursework and research progress, and led research team in several entrepreneurial competitions (see IonoMetal awards below).

Fall 2014 & 2015 **Teaching Assistant**, University of Washington
Course: CHEME465 Reactor Design

- Undergraduate senior core class with ~70 students.
- Responsible for preparing and giving weekly recitations and occasional lectures, teaching Mathematica/Matlab software for homework problems, developing homework assignments and solutions, holding weekly office hours, and grading course assignments and exams.

Winter 2013 **Teaching Assistant**, University of Washington
Course: CHEME485 Process Design I

- Undergraduate senior core class with ~60 students.
- Responsible for preparing weekly recitations, teaching ASPEN software, holding weekly office hours, and grading course homework and reports.
- Received the Department Outstanding Teaching Assistant Award voted on by the students

Winter 2012 **Teaching Assistant**, University of Washington
Course: CHEME436 Chemical Engineering Laboratory II

- Undergraduate senior core class with ~60 students.
- Supervised unit operation labs, graded lab reports, and provided feedback on oral presentations.

AWARDS

- The Electrochemical Society Norman Hackerman Young Author Award (2016)
- National Research Council (NRC) Research Associate Program Postdoctoral Fellowship Recipient
- Electrodeposition Division Travel Award for 228th ECS Meeting (2015)
- Graduate Student Symposium Best Poster by Industry Vote (2015)
- IonoMetal Technologies: Fenwick & West Best Cleantech Idea Award at the University of Washington 2014 Business Plan Competition (2014)
- IonoMetal Technologies: WRF Capital Honorable Mention Prize at the University of Washington 2014 Environmental Innovation Challenge (2014)
- Joseph L. McCarthy Outstanding Teaching Assistant Award (2013)
- GAANN Fellowship for Chemical Engineering Innovators Program (2013)
- College of Engineering Kaiser Aluminum Fellowship Award at University of Washington (2011)
- Selim Memorial Award for Most Promising Future in Chemical Engineering Graduate Studies at Colorado School of Mines (2011)
- Presidential Scholarship Award at Colorado School of Mines (2007-2011)
- Robert C. Byrd Honor Scholarship (2007-2011)
- Athletic Scholarship Award at Colorado School of Mines (2007-2011)
- CoSIDA/ESPN the Magazine First Team Academic All District Soccer (2009 & 2010)

OTHER EXPERIENCE

Experimental Expertise: Extensive experience working with various electrochemical and electroanalytical systems. Some experience working in clean rooms as well as machine shop training including mill and lathe equipment. Specific experimental techniques include scanning electron microscopy (SEM) and energy dispersive spectroscopy (EDS), stylus profilometry and AFM, and voltammetric electroanalytical techniques.

Software: MS Office, COMSOL Multiphysics, Mathematica/MATLAB, IGOR Pro, AutoCad/Solidworks, ASPEN Tech

VOLUNTEERING & SERVICE

2015-Present **Electrochemical Society (ECS) Chapter at University of Washington**

- Vice-chair for ECS chapter and helped start the chapter at the University of Washington in Fall of 2015.
- Organized and scheduled bi-weekly meetings that included journal club and presentations of research and electrochemical techniques. Also organized outreach electrochemical demonstrations to primary school students.

2012-2015 **UW Engineering Days Demonstration Volunteer**

- Demonstrated and taught K-12 local students about basic chemistry and chemical engineering science. These demos included “Cold Fun” using liquid nitrogen and dry ice for demonstrations.
- Organized and helped design the “Enginearring Days” demonstration where colorful jewelry was made by electrochemically anodizing titanium, creating different colors depending on the titanium oxide layer thickness.

2012-2013 **Association of Chemical Engineering (ACES)**

- Graduate student program that organizes social, professional development, and outreach events.
- Member of professional development committee that organized the 2012 and 2013 Grad Student Chemical Engineering Symposia. Also acted as ACES Treasurer.